이학박사 학위논문

Flexoelectric Control of Ferroelectric Properties and Electronic Functions in Epitaxial $BiFeO_3$ Thin Films

켜쌓기 성장시킨 비스무스 페라이트 박막에서
강유전성과 전기 기능성의 변전 제어 연구

2014 년 2 월

서울대학교 대학원

물리천문학부

전 병 철

Flexoelectric Control of Ferroelectric Properties and Electronic Functions in Epitaxial $BiFeO_3$ Thin Films

Byung Chul Jeon

Supervised by

Professor Tae Won Noh

A Dissertation submitted to the Faculty of Seoul National University in Partial Fulfillment of the Requirements for the Degree of Doctor of Philosophy

February 2014

Department of Physics and Astronomy

Graduate School

Seoul National University

Flexoelectric Control of Ferroelectric Properties and Electronic Functions in Epitaxial $BiFeO_3$ Thin Films

켜쌓기 성장시킨 비스무스 페라이트 박막에서 강유전성과 전기 기능성의 변전 제어 연구

지도교수 노 태 원

이 논문을 이학박사학위논문으로 제출함
2013 년 11 월

서울대학교 대학원
물리·천문학부
전 병 철

전병철의 박사학위논문을 인준함
2013 년 11 월

위 원 장 **유 재 준** (인)
부 위 원 장 **노 태 원** (인)
위 원 **박 제 근** (인)
위 원 **최 석 봉** (인)
위 원 **부 상 돈** (인)

Abstract

Flexoelectricity is the generation of an electric field by a strain gradient via electro-mechanical coupling. Although it was first theoretically reported by Kogan in the 1968, there have been few studies on flexoelectricity in bulk solid materials. It is because the flexoelectric effects are expected to be quite small in the rigid bulk solids. Recently, however it was reported that the strain gradient in epitaxial oxide thin films could be 6 or 7 orders of magnitude larger than the corresponding bulk values. As a result, flexoelectric effect has been emerging as a fascinating means for exploring the physical properties in epitaxial ferroelectric thin films. In this dissertation, I will report the effect of deposition temperature to the defect evolution and ferroelectric properties in $BiFeO_3$ thin films. I could successfully control the strain evolution of the $BiFeO_3$ films by varying the deposition temperature and the film thickness. I will show that the flexoelectric effect can reverse the as-grown polarization direction and associated changes in the electronic functional properties of $BiFeO_3$ thin films. Finally, I will show that the unusual coupling between internal electric field and defect formation in $BiFeO_3$ epitaxial thin films. By tailoring the internal electric field via flexoelectricity, I control the defect formation and achieve a nearly defect-free $BiFeO_3$ film that exhibits perfectly functional performances.

Ferroelectric materials promise a broad range of functional electronic properties, which are generally governed by various defects. Critical to practical applications of ferroelectric properties is our ability for understanding and controlling the defect formation. To investigate the effects of deposition temperature to the defect evolution and

the ferroelectric properties of the $BiFeO_3$ thin films, I grew $BiFeO_3$ thin films on (001) $SrTiO_3$ substrates using pulsed laser deposition at temperatures in the range of 570–600℃ at intervals of 10℃. Interestingly, I found that defects appeared at temperatures greater than 590℃ and threshold temperature is between 580℃ and 590℃. The defects led to significant changes in the optical absorption and impurity peaks in X-ray diffraction data. Analysis of the X-ray diffraction data indicates that the defects are Fe_2O_3. Atomic force microscopy measurements showed that the appearance of defects accompanied an abrupt increase in the surface roughness. Furthermore, the presence of the defects significantly affected ferroelectric hysteresis. Our results suggest that the evolution of defects in $BiFeO_3$ thin films depends strongly on the deposition temperature.

The flexoelectric effect can play an important role in determining the domain configurations and electronic transport properties in ferroelectric epitaxial thin films, due to its intrinsic and universal existence in every dielectric material. In $BiFeO_3$ epitaxial films with a large strain gradient, the flexoelectric and interfacial effects compete with each other in establishing the self-polarization state. The competing effects in the films were introduced by fabricating $BiFeO_3$ thin films of two different strain states, varying the deposition temperature and/or the film thickness. We found that uniaxially, fully strained $BiFeO_3$ films were self-poled, having a downward polarization; this indicated that the interfacial effect was dominant. In contrast, the relaxed films had upward self-polarization, indicating that the flexoelectric effect was dominant. Interestingly enough, the two kinds of films also exhibited different unidirectional current flows, referred to as the diode effect. By understanding the self-poling mechanisms in $BiFeO_3$ films, such as

ferroelectric hysteresis and electronic transport characteristics, the configuration of the as-grown films can be optimized to allow full utilization of the ferroelectric functional device.

Finally, internal fields (E_{int}) can be induced in ferroelectric thin film during the growth. Numerous origins have been proposed for the built-in electric field, namely, interfacial effects, flexoelectricity, defects, and piezoelectricity, and so on. I demonstrate that the defect formation in $BiFeO_3$ thin films critically depends on the internal electric field in the films. The large, systematic control of internal electric field is achieved via flexoelectricity, which can thereby modify the defect formation and associated electronic functions of the films. Such a flexoelectric control can be utilized to achieve a nearly defect-free $BiFeO_3$ film that exhibits perfectly functional performances, such as imprint-free polarization switching and switchable diode effect. This results highlight that flexoelectricity can dramatically modify the defect formation even with a small variation of growth parameters, emphasizing its potential key role in defect engineering. Our study provides novel insight into defect engineering, as well as a foundation for fully utilizing functional materials.

Keywords: $BiFeO_3$, ferroelectric, strain gradient, flexoelectric effect, epitaxial thin film, self-polarization, defects, internal field.

Student number: 2006-22908

Abstracts (English) ……i

List of Figures ……...ix

1 Introduction ……...1

1.1 $BiFeO_3$ ……..1

1.2 Flexoelectric effect in ferroelectrics ……4

1.3 Defect formation via internal electric field……...……6

2 Experimental detail …….....13

2.1 Pulsed laser deposition ……...13

2.2 Williamson-Hall plot by high-resolution X-ray diffraction ……..…..…16

2.3 Piezoelectric force microscopy ……...18

3 The effect of the deposition temperature on the formation of defects in $BiFeO_3$ thin films ……..21

3.1 Introduction …….…….……..21

3.2 Experiments ……23

3.2.1 Fabrication of $BiFeO_3$ thin films……..23

3.2.2 Experimental setup and methods for characterizations……23

3.3 Results and discussions …….. 24

3.3.1 Investigation of defects…… 24

3.3.1.1 High-resolution X-ray diffraction……...…….. 24

3.3.1.2 Optical spectroscopy……..25

3.3.1.3 Atomic force microsopy……26

3.3.2 Ferroelectric properties……27

3.4 Conclusion ……..…….…..... 28

4 Flexoelectric effect in the reversal of self-polarization and electronic functionalities of epitaxial ferroelectric thin films …….. 33

4.1 Introduction …….…….. 33

4.1.1 Flexoelectric effect……...33

4.1.2 Domain engineering in ferroelectrics……...34

4.1.3 Self-polarization in ferroelectric thin films……..35

4.2 Experiments ……...…….36

4.2.1 Sample preparation …….…….36

4.2.2 Characterization of crystal structures …… ……36

4.2.3 Piezoresponse force microscopy …….37

4.2.4 Electrical measurements ……..37

4.3 T_D effect in $BiFeO_3$ thin films ……38

4.3.1 Uniaxially strain and relaxed $BiFeO_3$ thin films ……38

4.3.2 Thickness & T_D-dependent lattice relaxation ……..42

4.4 Mechanism of self-polarization ……...…..…. ……....48

4.4.1 As-grown domain state in $BiFeO_3$ thin films ……..48

4.4.2 Reversal of self-polarization in $BiFeO_3$ thin films ……..50

4.5 Estimation of flexoelectric field……..……...…….52

4.5.1 Williamson-Hall plot ……...52

4.5.2 Estimation of strain gradient and flexoelectric field ……...53

4.6 Control of electronic functional properties ……55

4.6.1 Configuration of defects ……..55

4.6.2 *P–V* hysteresis loops ……56

4.6.3 Electronic transport characteristics ……..57

4.7 Conclusion ……..58

5 Flexoelectric control of defect formation and electronic functions in ferroelectric thin films ……63

5.1 Introduction ……63

5.2 Results……..65

5.2.1 Experiments ……...…….…….....65

5.2.1.1 Thin films fabrication ……..……...…….....66

5.2.1.2 Structural analysis …….....67

5.2.1.3 Electrical measurements……68

5.2.2 Large dependence of strain gradient on T_D ……..……..……..70

5.2.3 Functional properties of $BiFeO_3$ films according to T_D……....73

5.2.4 Defect configurations in $BiFeO_3$ films according to T_D ……..76

5.2.5 Large, systematic control of E_{int} via flexoelectricity ……...79

5.2.6 Demonstration of the E_{int} effect on defect formation ……..82

5.3 Discussion……83

5.4 Conclusion ……...…….....……..88

6 Conclusion ……93

Appendix ……..……97

Publication List ……...……..103

국문 초록 (Abstract in Korean) …….…….....105

감사의 글 (Acknowledgements) ……..…….....109

List of Figures

Figure 1.1 Phase control in ferroics and multiferroics. The stress σ, electric field E, and magnetic field H control the strain ε, electric polarization P, and magnetization M, respectively. For example, in a multiferroic material, H may control P and ε, or E may control ε and M, or σ may control P and M [1].

Figure 1.2 (a) Polarization hysteresis loop of an epitaxial BFO film grown on STO(111) with remnant polarization $P_r \sim 100\ \mu C\ cm^{-2}$. (b) Four possible ferroelectric polarization variants in BFO [3].

Figure 1.3 *I–V* curves taken both on the domain wall (black) and off the domain wall (red) reveal Schottky-like behaviour. Inset indicates the out-of-plane PFM image of a written 180° domain in a monodomain BFO(110) film [9].

Figure 1.4 (a) *J–E* curves of bulk BFO after +150 V, –150 V. and +150 V pulses, in sequence. The diode forward and reverse directions switch when the direction of out-of-plane polarization is reversed by ±150 V pulses. The diode forward direction turns out to be the same as the direction of electric pulses used for polarization flipping [10]. (b) The zero-bias photocurrent density as a function of time with (top) green light (λ = 532 nm) or (bottom) red light (λ = 650 nm) on or off, shining on the different sides of bulk BFO (a sketch is shown in the inset). (c) and (d) Atomic resolution STEM images of the T phase and the R phase, respectively. Insets show schematic illustration of the unit cell [11].

Figure. 1.5 Schematic description of the evolution of the strain relaxation in epitaxial thin films.

Figure 2.1 Schematic diagram of a pulsed laser deposition chamber.

Figure 2.2 (a) Fitting results of (001), (002), (003), and (004) diffraction peaks; peak shapes are well fitted using Pearson VII function. (b) W-H plots for the inhomogeneous strain ε_I. The numerical values of ε_I were determined from the slope of the fit equation [6-8].

Figure 2.3 Sketch of domain nucleation in PFM. The dashed arrows indicate the electric field (denoted *E* field) lines. The solid needlelike (blue) figures show reversed domains (i.e., nuclei). The BE indicates the bottom electrode. Adapted from Yang *et al.* [10].

Figure 2.4 From left to right, topography, out-of-plane (OP) amplitude, OP phase, in-plane (IP) amplitude, and IP phase images of epitaxial $BiFeO_3$ thin film.

Figure 3.1 XRD θ–2θ scans of the BFO films grown at various T_D (from bottom to top T_D = 570℃, 580℃, 590℃, and 600℃). The peaks are indexed with the following symbols: B: BFO, S: STO, ★: Fe_2O_3.

Figure 3.2 (a) The imaginary part of the dielectric function of the BFO films. (b) Schematic band diagram of the BFO thin films. The yellow band indicates the defect level. Peaks indicated by the blue and red arrows correspond to the optical transition from O 2*p* to defect and Fe 3*d* levels, respectively.

Figure 3.3 Surface roughness of the BFO films. The inset shows AFM images of the BFO films grown at various T_D.

Figure 3.4 *P*–*E* hysteresis loops of the BFO films grown at various T_D. The inset shows

P–E hysteresis loops of the BFO film grown at 600℃.

Figure 4.1 XRD θ–2θ scans of the 250-nm-thick BFO films grown at 570℃ (solid red line) and 550℃ (solid black line) on vicinal STO (001) substrates. The gray short-dashed and solid vertical lines indicate the (002) diffraction peak positions of the fully strained and relaxed BFO films on STO substrates, respectively.

Figure 4.2 RSMs around the $\{\bar{1}03\}$ STO Bragg family of peaks with various ϕ angles for 250-nm-thick US- and R-BFO films. The $(\bar{1}03)$, (103), $(0\bar{1}3)$, and (013) peaks can be distinguished from each other in the RSM data, due to the large rhombohedral distortion of the BFO unit cell [22].

Figure 4.3 (a) HRXRD θ–2θ scans of BFO films grown at 570℃ between 50 and 250 nm thick. The closed blue triangles, black circles, and open-inverted triangles indicate the (002) peaks of BFO, SRO, and STO, respectively. The gray dash-dotted and solid lines indicate the (002) diffraction peak positions of the fully strained and relaxed BFO films on STO substrates, respectively. The θ–2θ scans show that the 50-nm-thick film is fully strained in the [001] direction. However, above a critical thickness, the strain should start to relax. As the film thickness increased, the 2θ peak position moved to larger angles, indicating that the average *c*-axis lattice constant became smaller. (b)–(e) RSM images around the $(0\bar{1}3)$ STO Bragg peaks of BFO films grown at 570℃ between 50 and 250 nm thick. As displayed in the RSM data, all of these films were fully strained along the [010] direction; i.e., they should be US-BFO films.

Figure 4.4 (a) and (b) Pseudocubic lattice parameters as a function of the film thickness

for US- and R-BFO films, respectively. The solid and dotted gray lines represent the lattice parameter of bulk BFO and STO, respectively.

Figure 4.5 Schematic representation of the direction of the strain relaxation for US-BFO films. The dark and pale gray areas represent strongly strained and relaxed BFO regions, respectively. (a), (b), and (c) indicate the schematic diagram top, side, and front views of the US-BFO film, respectively. The large blue arrow indicates the direction of vertical flexoelectric field ($E_{F,3}$). The green-dotted and black solid-line arrows indicate the direction of ferroelectric polarization, P_1^- and P_4^-, respectively. (d) Possible orientations of the polarization for US-BFO films on vicinal STO substrates. The step-bunching process and lattice dislocations (higher-order terms) are neglected in this representation. Recently, we demonstrated that in BFO films grown on vicinal STO substrates, some structural relaxation can occur through the step-bunching process and lattice dislocations [38]. However, because the resulting crystallographic tilt angle and the *c*-axis lattice constant should be higher-order variations, we neglected such effects in the schematic diagram [38]. To make the strain gradient more visible, we exaggerated the difference in the length scale of the BFO unit cells.

Figure 4.6 (a) XRD θ–2θ scans of BFO films grown at 550℃ between 50 and 250 nm thick. The closed blue triangles, black circles, and open-inverted triangles indicate the (002) peaks of BFO, SRO, and STO, respectively. The gray dash-dotted and solid lines indicate the (002) diffraction peak positions of the fully strained and relaxed BFO films on STO substrates, respectively. The θ–2θ scans show that the 50-nm-thick film is fully strained. However, above a critical thickness, the strain should start to relax. As the film

thickness increased, the 2θ peak position moved to larger angles, indicating that the average *c*-axis lattice constant became smaller. (b)–(e) RSM images around the $(0\bar{1}3)$ STO Bragg peaks of BFO films grown at 550℃ between 50 and 250 nm-thick. As displayed in the RSM data, the 50-nm-thick BFO film is fully strained. Above the critical thickness, the films were relaxed; i.e., they should be R-BFO films.

Figure 4.7 Schematic diagram of the direction of the strain relaxation for R-BFO films. The dark and pale gray areas represent strongly strained and relaxed regions, respectively. (a), (b), and (c) Schematic diagram top, side, and front views, respectively. The large red and blue arrows indicate the direction of the horizontal ($E_{F,1}$) and vertical ($E_{F,3}$) flexoelectric fields, respectively. (d) Possible polarization orientation for R-BFO films. The green-dotted and black solid-line arrows indicate the direction of ferroelectric polarization, P_1^+ and P_4^+, respectively. The step-bunching process and lattice dislocations (higher-order terms) are neglected in this representation [38].

Figure 4.8 (a) and (b) Out-of-plane PFM images with 50-, 120-, 180-, and 250-nm-thick BFO films. The bright yellow and dark regions indicate the up- and down-polarization states, respectively.

Figures 4.9 *P*–*V* loops for (a) 50-, (b) 120-, (c) 180-, and (d) 250-nm-thick BFO films grown at 570 ℃; (e) 50-, (f) 120-, (g) 180-, and (h) 250-nm-thick BFO films grown at 550 ℃. The 50-nm-thick BFO films exhibited a leaky behavior. The 120-, 180-, and 250-nm-thick US-BFO (R-BFO) films showed negative (positive) imprint characteristics. These imprint behaviors were nearly consistent with thickness dependence of self-polarization direction, as shown in the PFM images of Figures 4.8a and 4.8b.

Figure 4.10 Magnitude of the flexoelectric and interfacial effects as a function of film thickness. The red and black-dashed curves indicate the flexoelectric and interfacial effects, respectively. The right and left insets indicate the fully strained and relaxed BFO films, respectively.

Figure 4.11 (a) Out-of-plane and (b) in-plane W-H plots for the inhomogeneous strain of the BFO films.

Figure 4.12 (a) and (b) Schematic diagram of the location of the V_O-rich defect layer in US- and R-BFO films, respectively. The large white arrows represent the as-grown polarization direction.

Figure 4.13 (a) and (b) *P*–*V* hysteresis loops of the US-and R-BFO films, respectively. Vertical gray-dashed lines indicate the voltage center of hysteresis loops.

Figure 4.14 (a) and (b) *J*–*V* curves of US- and R-BFO films, respectively.

Figure 5.1 Structural analysis. (a) XRD θ–2θ scans of 250-nm-thick $BiFeO_3$ films gr own at T_D = 550, 560, 570 and 580℃ on vicinal $SrTiO_3$ (001) substrates. The gray s hort-dashed and solid vertical lines indicate the (002) diffraction peak positions of t he fully strained and relaxed $BiFeO_3$ films on $SrTiO_3$ substrates, respectively. (b) RSM images around the (013) $SrTiO_3$ Bragg peaks for 250-nm-thick $BiFeO_3$ films grown at T_D = 550, 560, 570 and 580℃.

Figure 5.2 Large, systematic variation of strain gradient, according to T_D. (a) Expected surface mobility of adatoms at the T_D range of 550 to 580℃. The inset schematically depicts the mobility of adatoms at each T_D. (b) The measured strain gradients in 250-nm-

thick $BiFeO_3$ films for different T_D. These values, estimated at room temperature, are believed to remain almost unchanged at high temperatures (during film-growth process), due to similar thermal lattice expansion of perovskite materials. Solid lines are the guide to eyes.

Figure 5.3 Large dependence of strain gradient on T_D. (a,b) Upper panels show atomic force microscopy images of 250-nm-thick $BiFeO_3$ films for (a) T_D = 550℃ and (b) 580℃. The film surface for T_D = 580℃ has a typical morphology of the step-flow growth mode. On the other hand, for T_D = 550℃, the lateral length of $BiFeO_3$ grains became much shorter, possibly due to the limited mobility of adatoms at lower T_D. Lower panels schematically describe the expected strain profile for (a) T_D = 550℃ and (b) 580℃. Considering the relationship bewteen the grain shape (e.g., aspect ratio) and strain relaxation, we can expect a larger strain gradient for lower T_D. (c) Rough estimation of in-plane strain gradient. According to a general model for the strain profile [23,24], independent of the actual relaxation mechanism, the in-plane strain ε can be expressed as follows:

$$\varepsilon(x) = \varepsilon_0 \cdot e^{-x/\delta} \quad (2)$$

where ε_0 and δ are constants, and x is the distance from the step edge. Typically, a film can be fully strained near the step edge (i.e., x = 0), due to a strong clamping effect. Also, we know the average in-plane strain values from the RSM results. Thus, using these information and Eq. (2), we can roughly estimate the profile of in-plane strain gradient. We here assumed the width of step terraces as 100 nm. The estimated values were found to be quite comparable with those obtained by W-H plots (Fig. 2b).

Figure 5.4 Electronic functions of $BiFeO_3$ films, according to T_D. (a) *P–E* hysteresis loops for 250-nm-thick $BiFeO_3$ films deposited at four different T_D of 550, 560, 570 and 580℃. (b) *J–E* curves measured for 250-nm-thick $BiFeO_3$ films deposited at four different T_D.

Figure 5.5 The shift of *P–E* loops. (a,b) *P–E* hysteresis loops of 250-nm-thick $BiFeO_3$ films for (a) T_D = 550℃ and (b) 570℃. We recently demonstrated that the shift of *P–E* loops is mainly due to the pinning field (E_{dd}) by defect dipoles (D_{defect}) [27]. We also found that the D_{defect} alignmnent (and associated E_{dd} direction) can be reversed by the polarization switching and subsequent annealing, which modifies the *P–E* hysteresis loops (i.e., the direction of shift). (Details of the annealing procedure are explained in ref. 27.) (c,d) Schematic illustrations describing the D_{defect} and E_{int} (= E_{if} + E_{flexo}) direction of the as-grown (left) and annealed state (right), for (c) T_D = 550℃ and (d) 570℃. (e) The direction of E_{dd} (by D_{defect}) can be reversed after the annealing precedure, whereas the E_{int} direction should be nearly unchanged. This means that the shifted value (E_{shift}) of *P–E* loops can be expressed as

$$E_{shift} = \pm E_{dd} + E_{int} \text{ (+: for as-grown state, –: for annealed state)} \quad (3).$$

Thus, using the E_{shift} values (obtained from *P–E* loops), we can estimate the values of E_{dd} and E_{int}, as shown in (e). The estimated values indicate that the shift of *P–E* loops is mainly due to E_{dd} (by D_{defect}), with small contribution from E_{int}. Referring to the strain-gradient values (Fig. 5.2) for T_D = 550℃ and 570℃, we also determined the values of E_{if} and E_{flexo}, which are comparable with the calculated E_{if} (ref. 28) and estimated E_{flexo} values (Fig. 5.8).

Figure 5.6 Defect configurations in $BiFeO_3$ films, according to T_D. (a) The schematic configurations of D_{defect} and V_O-rich layer in $BiFeO_3$ films according to T_D, determined from the measurements of *P–E* loops and *J–E* curves. (b) The shift in *P–E* loops of 250-nm-thick $BiFeO_3$ films, as a function of T_D. We normalized the shifted values (E_{shift}) of *P–E* loops by the coercive field (i.e., $E_c = (E_{c,+} - E_{c,-})/2$). (c) Unit-cell volume (black closed squares) and estimated V_O concentration (red closed circles) of 250-nm-thick $BiFeO_3$ films, as a function of T_D.

Figure 5.7 Two competing, intrinsic sources of E_{int} in $BiFeO_3$ films on $SrRuO_3/SrTiO_3$. (a) Interfacial charge discontinuity can generate the downward internal electric field (E_{if}) in $BiFeO_3$ films on $SrRuO_3/SrTiO_3$ substrate [28]. Note that $SrRuO_3$ is self-terminated with SrO surface, since the RuO_2-layer is highly volatile. (b) Relaxation of compressive misfit strain can generate the upward internal electric field (E_{flexo}) via flexoelectricity in $BiFeO_3$ films on $SrRuO_3/SrTiO_3$ substrate.

Figure 5.8 Large, systematic control of E_{int} via flexoelectricity. The estimated E_{int} for 250-nm-thick $BiFeO_3$ films, as a function of T_D. Using the measured values of strain gradient, we estimated E_{flexo}, projected onto the ferroelectric polarization direction (i.e., [111] or its equivalent ones). Red open and closed squares correspond to E_{flexo} for the flexoelectric coefficient λ = 1.0 and 0.25, respectively. Red dashed line represents the averaged values of E_{flexo} for λ = 1.0 and 0.25. Blue open triangles represent E_{if}, obtained by referring to the calculated values (ref. 9) and projecting them onto the polarization direction. Black solid line represents E_{int} (= E_{flexo} + E_{if}) according to T_D, obtained by summing E_{flexo} and E_{if}. The positive (or negative) E_{int} indicates the upward (or downward)

field direction.

Figure 5.9 Demonstration of the E_{int} effect on defect formation. (a,b) Schematics of the E_{int} variation according to the film thickness t, for (a) T_D = 550 and (b) 570℃. Red, blue and black arrows represent E_{flexo}, E_{if} and E_{int}, respectively. The length o f arrows indicates the magnitude of the associated electric field. (c,d) The measure d shift of P–E loops (black closed circles) and unit-cell volume (red open squares) as a function of t, for (c) T_D = 550 and (d) 570℃. Solid lines are the guide to eyes.

Figure 5.10 Effect of E_{int} on polarization-mediated defect formation. (a) Schematic illus tration of the defect formation in ferroelectrics. Defect dipoles (D_{defect}) acquire the energy gain for their formation by the interaction with ferroelectric polarization P (ref. 27,35,36). Usually, cation vacancy (V_{cation}) or impurity forms D_{defect} together w ith oxygen vacancy (V_O). Also, the interfacial accumulation of positively charged V_O can have the energy gain by compensating the negative polarization charge, res ulting in the formation of V_O-rich layer [37,38]. (b) Expectation of polarization profile at high temperatures during film growth, according to E_{int}. For $E_{int} \approx 0$, the inter action between charged point defects and polarization can be weakened due to the rmal fluctuation ($\sim k_B T$) of polarization, inhibiting the polarization-mediated defect fo rmation. On the other hand, if a large E_{int} exists, it can induce a noticeable magnitude of polarization, as well as stabillize the ferroelectric polarization against thermal fluctuation. (c) The polarization-mediated defect formation can be promoted under a large E_{int}.

Figure 5.11 Possible effect of E_{int} on the formation of point defects. (a) A large E_{int} ca n cause the lattice volume expansion by piezoelectric effect in ferroelectrics. [Note

that E_{int} can also cause the crystal volume expansion (as large as ~1.0 % locally) by electrostrictive effect in polar materials, already reported in ref. 39.] (b) The formation of point defects is accompanied with the increase of unit-cell volume, requiring an energy cost (e.g., from elastic energy). If the unit-cell volume is already large, the energy cost for the defect formation can be reduced. Referring to a recent theoretical work [40], we can expect that the formation of point defects can be mo re promoted for the enlarged unit cell under a large E_{int}, increasing the equilibriu m defect concentration in our $BiFeO_3$ films. (c) In order to quantitatively explore a possible crystal volume expansion by E_{int}, we consider the E_{flexo} contribution. Th e strain relaxation and associated E_{flexo} follow the exponential decay as a function of distance (d) from the bottom interface (i.e., $\propto e^{-d/\delta}$). We assumed the averaged E_{flexo} value of 5×10^6 V m^{-1} and the δ value of 40 nm. We also used three differe nt values (d_{33} = 100, 150, and 200 pm V^{-1}) for converse piezoelectric coefficient. The d_{33} value of $BiFeO_3$ is around 50–100 pm V^{-1} at room temperature. Note that the d_{33} is roughly proportional to the dielectric permittivity and polarization (i.e., $\propto \varepsilon \cdot P$), and thus can show the increasing trend as the temperature increases and approaches to the Curie temperature. In spite of the parameter dependence, our res ult evidently shows that the E_{int} can lead to a lattice-volume expansion (as large a s locally 0.5–1.0 %) at high temperatures during film growth.

Figure A.1 (a) BFO/SRO/STO 박막의 θ-2θ를 (001), (002), (003), 그리고 (004)까지 측정한 데이터. (b) BFO 박막 peak을 Pearson VII 식을 이용한 fitting. 여기서

β_{BFO}는 BFO 박막의 FWHM 값.

Figure A.2 Out-of-plane WHP. 기울기는 inhomogeneous strain, ε_I를 나타낸다.

Figure A.3 BFO/SRO/STO 박막의 (013), (023), 그리고 (033)까지 측정한 RSM 데이터. I used the line width in the *k*-direction of the RSM peaks–(013), (023), and (033)–of BFO films.

Chapter 1
Introduction

1.1 $BiFeO_3$

$BiFeO_3$ (BFO) is one of the most interesting multiferroic materials [1,2]. It simultaneously has at least two order parameters, i.e., ferroelectricity [2], ferroelasticity [3], and antiferromagnetism [1,2]. It has been explored for several decades, since they offered the possibility of manipulating the magnetic polarization by an electric field or vice versa, as shown in Figure 1.1. Magnetoelectric multiferroics are technologically and scientifically promising because of their potential applications in data storage, spintronics, sensor applications, etc. The ferroelectric and antiferromagnetic ordering temperatures are far above room temperature; the Curie and Néel temperatures are 1103 and 643 K, respectively [2]. Moreover, among all known ferroelectrics, BFO has the largest remnant polarization of 100 μC cm^{-2} along [111] direction, as shown in Figure 1.2(a). The bulk BFO shows rhombohedral (a=5.58 Å and α=89.5°) crystal structure at room temperature with the space group $R3c$ and G-type antiferromagnetism. There are four possible polarization variants, r_1, r_2, r_3, and r_4 in BFO, as shown in Figure 1.2(b) [3]. These properties make BFO be a promising ferroelectric material for applications, such as

magnetoelectrics [4,5], ferroelectric random-access memory [7], photovoltaics [8], etc.

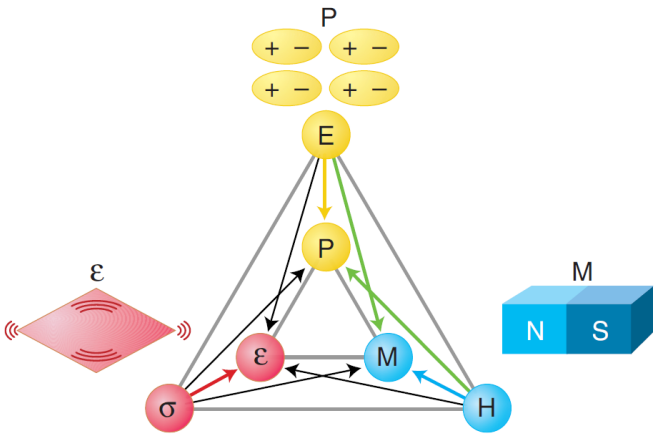

Figure 1.1 Phase control in ferroics and multiferroics. The stress *σ*, electric field *E*, and magnetic field *H* control the strain *ε*, electric polarization *P*, and magnetization *M*, respectively. For example, in a multiferroic material, *H* may control *P* and *ε*, or *E* may control *ε* and *M*, or *σ* may control *P* and *M* [1].

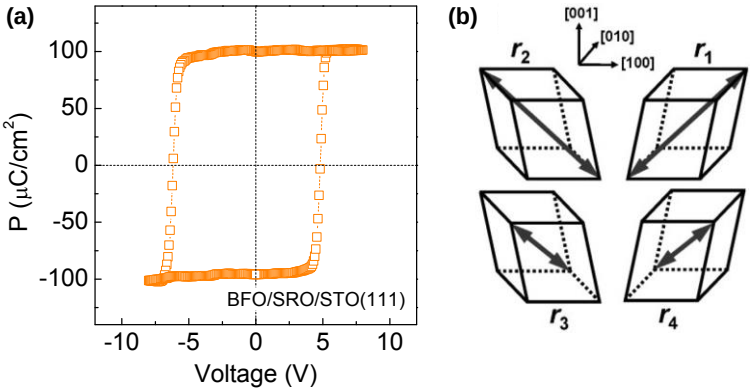

Figure 1.2 (a) Polarization hysteresis loop of an epitaxial BFO film grown on STO(111) with remnant polarization P_r ~ 100 μC cm^{-2}. (b) Four possible

ferroelectric polarization variants in BFO [3].

There have been many issues in BFO material due to the intriguing physical properties from the last decade. Seidel *et al*. reported the observation of room-temperature electronic conductivity at ferroelectric domain walls in the insulating BFO thin film [9]. Figure 1.3 shows the current–voltage (*I*–*V*) curves at the domain (red solid line) and domain wall (black solid line), respectively. They observed Schottky-like conduction behavior at the domain wall. Choi *et al*. reported a switchable diode and photovoltaic effects in BFO single crystal, as shown in Figure 1.4a and 4b [10]. Using a combination of epitaxial growth techniques in conjunction with theoretical approaches, Zeches *et al*. showed the formation of a morphotropic phase boundary through epitaxial constraint in lead-free piezoelectric bismuth ferrite films (show Figure 1.4c and 4d) [11].

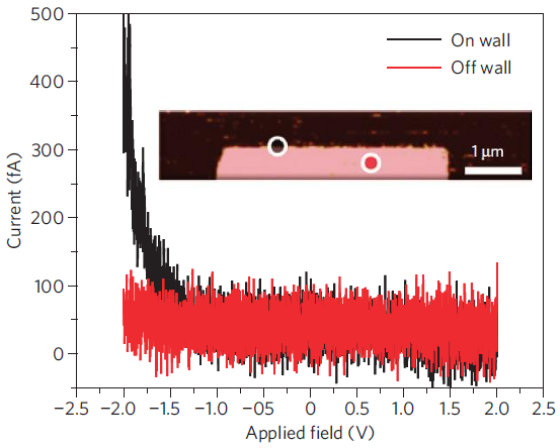

Figure 1.3 *I*–*V* curves taken both on the domain wall (black) and off the domain wall (red) reveal Schottky-like behaviour. Inset indicates the out-of-plane PFM image of

a written 180° domain in a monodomain BFO(110) film [9].

1.2 Flexoelectric effect in ferroelectrics

Flexoelectricity is the generation of an electric field by a strain gradient via electro-mechanical coupling. This effect was predicted theoretically by Kogan in 1964 [12] and experimentally observed by Bursian and Zaikovskii in 1968 [13]. The phenomenon was given the name 'flexoelectricity' by Indenbom et al. in 1981 [14]. Despite its long history, there has been little research on flexoelectricity of bulk solid materials [14-24], because its effects had been widely accepted to be quite small. Namely, the flexoelectric coefficients are small (10^{-10}–10^{-11} C m^{-1}) [23], and the strain gradients generated by mechanical bending are quite small, typically on the order of 0.1 m^{-1} [24].

Recently, there has been much interest in flexoelectricity, especially regarding epitaxial thin films [25-31]. Inside these material systems, a strain gradient as large as 10^5–10^6 m^{-1} can be produced [25,26]. Note that this value of the strain gradient is 6 or 7 orders of magnitude larger than the corresponding bulk values. Figure 1.5 indicates the strain gradient by relaxation of strain in epitaxial thin film. Using numerous epitaxial ferroelectric thin films, experimental studies showed that flexoelectricity can affect the domain configuration and imprint [26], dielectric constant [27,28], continuous rotation of the spontaneous polarization direction [29], polarization switching by mechanical force [30], and unusual coupling between electronic transport and the mechanical strain gradient [31].

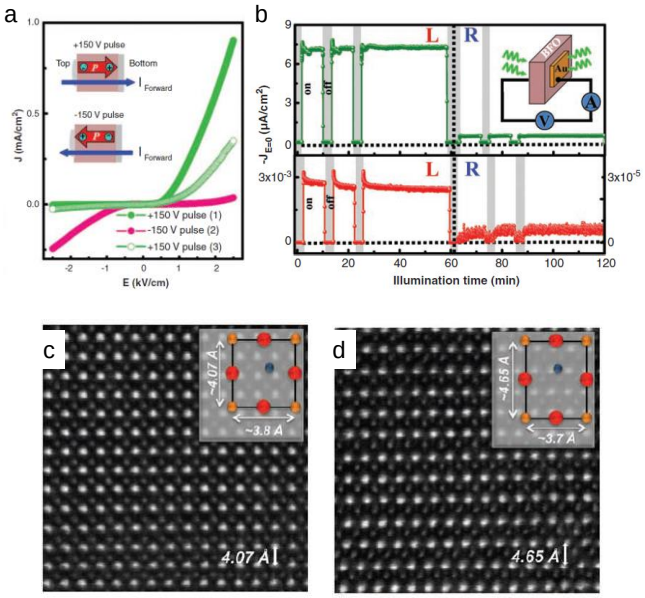

Figure 1.4 (a) *J–E* curves of bulk BFO after +150 V, –150 V. and +150 V pulses, in sequence. The diode forward and reverse directions switch when the direction of out-of-plane polarization is reversed by ±150 V pulses. The diode forward direction turns out to be the same as the direction of electric pulses used for polarization flipping [10]. (b) The zero-bias photocurrent density as a function of time with (top) green light (λ = 532 nm) or (bottom) red light (λ = 650 nm) on or off, shining on the different sides of bulk BFO (a sketch is shown in the inset). (c) and (d) Atomic resolution STEM images of the T phase and the R phase, respectively. Insets show schematic illustration of the unit cell [11].

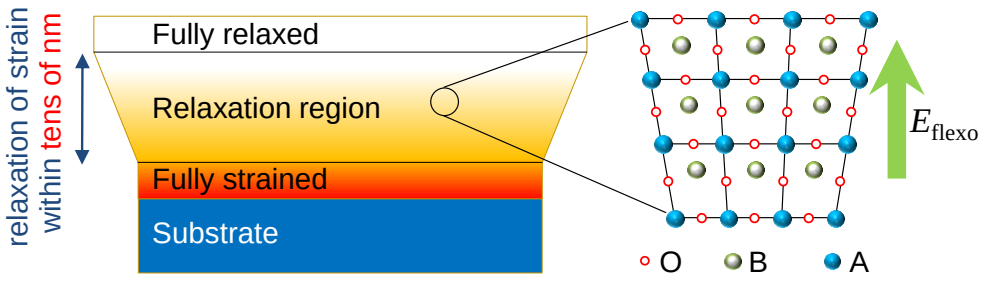

Figure 1.5 Schematic description of the evolution of the strain relaxation in epitaxial thin films.

1.3 Defect formation via internal electric field

The advancement of materials science relies on our ability to modify and optimize a wide range of functional properties. These properties, including electronic, magnetic, and optical properties, critically depend on the type and concentration of defects, which exist in every material. Particularly in ferroelectrics, defects play a governing role in the control and optimization of these materials [32,33]. Typical ferroelectric materials allow for a diversity of point defects and extended defects, which sometimes seem unavoidable even with the well-chosen fabrication conditions. These defects are usually detrimental to a functional ferroelectric property [32], but can be desirable for some functions, such as giant electromechanical response [34] and multilevel data storage [35]. This makes it necessary to fully understand the mechanism of defect formation, for relevantly controlling defects and their effect. While our understanding still continues to evolve, the exact mechanism of defect formation remains unclear, with many important factors

unresolved.

The interaction between polarization and charged point defects is one of the well-known mechanisms for defect formation in ferroelectrics [34-38]. It has been widely accepted that ferroelectric polarization drives charged point defects (e.g., vacancies) to migrate towards the energetically preferred sites, facilitating the defect formation during fabrication process. However, it has been overlooked that such polarization-mediated defect formation can be more promoted by other intrinsic polarizations, which have a different origin from the ferroelectric polarization. Recent studies reported that in epitaxial thin films, a huge internal electric field (E_{int}) can emerge intrinsically by various sources, such as interfacial charge discontinuity [39,40] and strain gradient [26,29], generating a considerable magnitude of polarization. Its magnitude can be around E_{int} = 10^6 V m^{-1} on the average and even as large as 10^7–10^8 V m^{-1} locally, which can induce the polarization of 1–10 μC cm^{-2} and seems large enough to affect the defect formation at high temperatures. Therefore, although overlooked so far, it would be critical to explore how such E_{int} and induced polarization influence the defect formation in thin films.

Particularly, flexoelectricity (i.e., generation of E_{int} by strain gradient) [24,26,40-43] has recently gained much attention. The strain gradient naturally breaks the inversion symmetry and thus can induce an electric response and intriguing phenomena in all dielectric materials. Especially regarding epitaxial thin films, in which the lattice mismatch can give rise to very steep elastic strain relaxation, the strain gradient becomes huge and the associated flexoelectric field can be as large as $\geq 10^7$ V m^{-1}. This flexoelectric field has played an important role in novel electronic functions, such as

domain control [26], flexoelectric rotation of polarization [40], mechanical writing of polarization [30], and flexoelectric diode [31]. Despite such universal, strong nature of flexoelectricity, however, its possible influence on the defect formation during thin-film epitaxy has received little consideration. The exploitation of such an effect would allow the design of defect configuration and associated electronic functions, as well as provide a pathway to unravelling the fundamental physics of defect formation.

References

1. N. A. Spaldin and M. Fiebig, Science **309**, 391 (2005).
2. J. Wang et al., Science **299**, 1719 (2003).
3. S. H. Baek et al., Nat. Mater. **9**, 309 (2010).
4. T. Zhao et al., Nature Mat. 5, 823 (2006).
5. M. Fiebig et al., Nature **419**, 818 (2002).
6. N. A. Hill and K. M. Rabe, Phys. Rev. B **59**, 8759 (1999).
7. D. Lee et al., Adv. Mater. **24**, 402 (2012).
8. W. Ji et al., Adv. Mater. **22**, 1763 (2010).
9. J. Seidel et al., Nature Mat. 25, 229 (2009).
10. T. Choi et al., Science **324**, 63 (2009).
11. R. J. Zeches et al., Science **326**, 977 (2009).
12. S. M. Kogan, Sov. Phys. Solid State, **5**, 2069 (1964).
13. E. V. Bursian et al., Sov. Phys. Solid State **10**, 1121 (1968).
14. V. L. Indenbom et al., Kristallografiya **26**, 1157 (1981).
15. A. K. Tagantsev, Phys. Rev. B **34**, 5883 (1986).
16. W. Ma, L. E. Cross, Appl. Phys Lett. **78**, 2920 (2001).
17. R. Resta, Phys. Rev. Lett. **105**, 127601 (2010).
18. R. Maranganti, and P. Sharma, Phys. Rev. B **80**, 054109 (2009).
19. A. K. Tagantsev, V. Meunier, P. Sharma, MRS Bulletin, **34**, 643 (2009).
20. A. Gruverman et al., Appl. Phys. Lett. **83**, 728 (2003).
21. W. Ma and L. E. Cross, Appl. Phys. Lett. **86**, 072905 (2005).

22. W. Ma , L. E. Cross , Appl. Phys. Lett. **88**, 232902 (2006).
23. L. E. Cross, J. Mater. Sci. **41**, 53 (2006).
24. P. Zubko et al., Phys. Rev. Lett. **99**, 167601 (2007).
25. D. Lee, T. W. Noh, Philos. Transact. A. Math. Phys. Eng. Sci. **370**, 4944 (2012).
26. D. Lee, et al., Phys. Rev. Lett. **107**, 057602 (2011).
27. G. Catalan et al., J. Phys.: Condens. Matter **16**, 2253 (2004).
28. G. Catalan et al., Phys. Rev. B **72**, 020102(R) (2005).
29. G. Catalan et al., Nature Mater. **16**, 963 (2011).
30. H. Lu et al., Science **336**, 59 (2012).
31. D. Lee et al., Nano Lett. **12**, 6436 (2012).
32. M. E. Lines, A. M. Glass, Principles and Applications of Ferroelectrics and Related Materials, Clarendon, Oxford 1977.
33. M. Dawber, K. M. Rabe, J. F. Scott, Rev. Mod. Phys. **77**, 1083 (2005).
34. X. Ren, Nat. Mater. **3**, 91 (2004).
35. D. Lee et al., Adv. Mater. **24**, 6490 (2012).
36. D. Lee et al., Phys. Rev. B **84**, 125305 (2011).
37. M. F. Chisholm et al., Phys. Rev. Lett. **105**, 197602 (2010).
38. D. Lee et al., Phys. Rev. B **81**, 012101 (2010).
39. A. Ohtomo, H. Y. Hwang, Nature **427**, 423 (2004).
40. P. Yu et al., Proc. Natl. Acad. Sci. **109**, 9710 (2012).
41. S. M. Kogan, Sov. Phys. Solid State **5**, 2069 (1964).
42. G. Catalan et al., Phys. Rev. B **72**, 020102(R) (2005).

43. P. Zubko et al., Annu. Rev. Mater. Res. **43**, 387 (2013).

Chapter 2
Experimental detail

2.1 Pulsed laser deposition

The choice of deposition method has a significant impact on the properties of oxide thin films [1-4]. Each deposition method has its own unique advantage and disadvantage that affects microstructure and physical property of films. Pulsed Laser Deposition (PLD) method offers a very wide range of deposition parameters, which makes it an attractive tool for investigating the effects of the deposition parameters.[5] For example, PLD has flexibility in controlling parameters like deposition temperature, deposition pressure, target material composition, growth rate. Figure 2.1 shows a schematic diagram of an experimental setup. It consists of a target holder and a substrate holder housed in a vacuum chamber. A high power laser is used as an external energy source to vaporize materials and to deposit thin films. A set of optical components is used to focus the laser beam over the target surface.

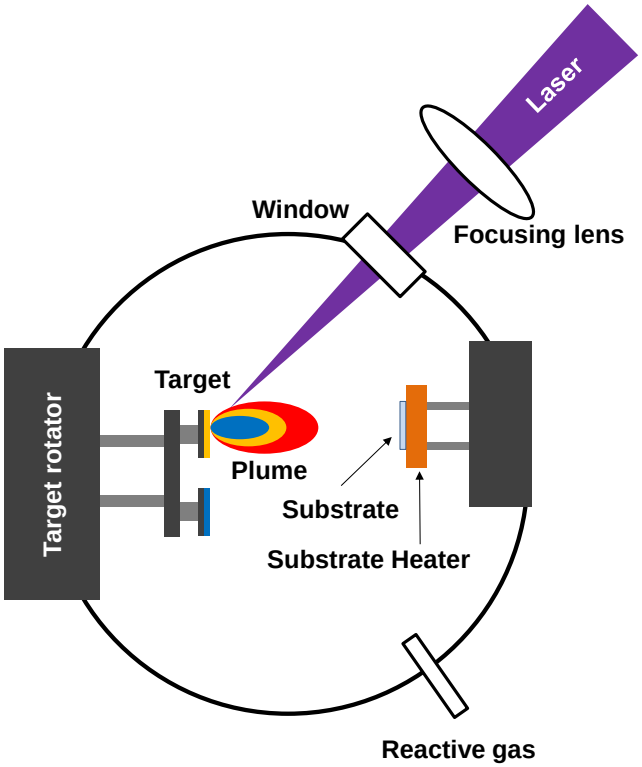

Figure 2.1 Schematic diagram of a pulsed laser deposition chamber.

The decoupling of the vacuum chambers and the evaporation power source makes PLD more simple and flexible than with the constraints imposed by the use of internally powered evaporation sources. Because of the fast and very directional plume, attenuation due to trajectory change as a result of collisions with the background gas is small.

Main advantages of PLD are listed as follows:

• Ability of using high pressures as well as ultra high vacuum (UHV) conditions.

• Flexibility and good control of substrate temperature by allowing heater designs in

different complexity.

• High energy particles in plasma increased reactivity by using a large variety of process gases.

• Stoichiometric transfer from target to substrate

• Highly controllable deposition rate

• Multiple target usage for multilayer depositions

• Reduced deposition chamber size by placing the power source outside of the chamber, which eases the pumping operations.

However, there are two major drawbacks of PLD. One is the lack of uniformity over a large area due to narrow angular distribution of the plume. It may be solved by rotation or translation of substrates. The other one, “splashing” which means, “the deposition of particulates onto the substrates” is an intrinsic problem, much more difficult to overcome. The occurrence of splashing has many origins. For example, surface boiling, exfoliation of target, etc. The solutions to avoid splashing are lowering the laser power density, using mechanical particle filter, which actually lowers the deposition rate.

The parameters for the optimization of PLD conditions are listed as follows:

• Substrate temperature

• Growth rate

• Laser energy density

• Ambient gas pressure

• Laser beam intensity profile, which is determined by laser path and voltage.

• Annealing (Treatment after film deposition)

• Substrate pre-treatment

2.2 Williamson-Hall plot by high-resolution X-ray diffraction

The crystal structure of thin films can be usually obtained from the high-resolution X-ray diffraction (HRXRD). Through HRXRD measurement combined with x-ray reflectometry (XRR) measurements, the lattice constants of the global film can be obtained along with the film thickness. On the other hand, θ-2θ scan shows the *c*-axis lattice constant of the film along with the thickness of the film. When a superlattice is deposited instead of thin film, satellite peaks can be observed due to the multiplied unit cell of the superlattice structure. By analyzing them we can confirm the period of the superlattices. In addition, by analyzing the reciprocal space mapping (RSM), we can obtain the information on the in-plane lattice constant. The *x*- and *y*-axis in the map corresponds to the reciprocal of the *a*- and *c*-axis, respectively.

In order to calculate the vertical inhomogeneous strain (ε_I), four peaks–(001), (002), (003), and (004)–are selected from the XRD θ–2θ data, as-shown in Figure 2.2a. The following equation was used for the fit [6-8].

$$\beta \cos\theta = K\lambda / D + 4\varepsilon_I \sin\theta ,$$

where β is defined by $\beta = \beta_{\text{sample}} - \beta_{\text{substrate}}$, and β_{sample} and $\beta_{\text{substrate}}$ indicate the full-width at half maximum (FWHM) values of sample and substrate peaks, respectively [5], λ

=1.5406 Å, D is the coherence length along the scattering vector, K is a geometrical constant which was taken as 1. We adopted the Pearson VII function, $I(x) = I(0)/(1+Cx^2)^m$ for fitting to obtain the more accurate line widths [8]. There are many approaches to the modeling of diffraction lines, but one of the most commonly used functions is the Pearson VII. The Pearson VII clearly includes the Lorentzian (m = 1) and it tends to a Gaussian as m → ∞. The solid lines are fitted results, as shown in Figure 2.2b. Similarly, we estimated the in-plane ε_I of the films. To obtain the in-plane ε_I, we used the line width in the k-direction of the RSM peaks–(013), (023), and (033)–of film and substrate. (I will explain the W-H plot method more detail in Appendix)

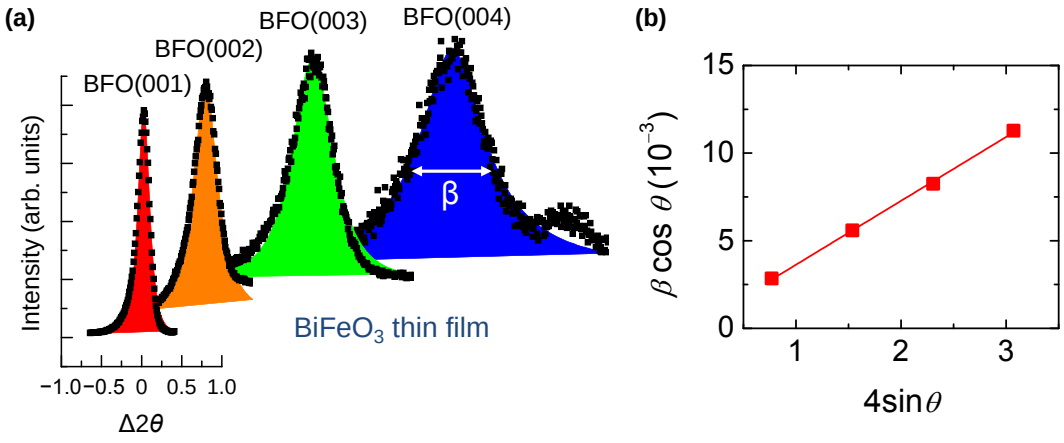

Figure 2.2 (a) Fitting results of (001), (002), (003), and (004) diffraction peaks; peak shapes are well fitted using Pearson VII function. (b) W-H plots for the inhomogeneous strain ε_I. The numerical values of ε_I were determined from the slope of the fit equation [6-8].

2.3 Piezoelectric force microscopy

Piezoresponse force microscopy (PFM), a specialized atomic force microscopy (AFM) technique, is a very powerful method for direct visualization of ferroelectric (FE) static domain configurations and their dynamic behaviors at nanoscale [9-13]. All FEs should exhibit the piezoelectric effect, a linear coupling between mechanical strains and electric fields. When a stress is applied to FE materials, a mechanical displacement will be induced, leading to the generation of an electric field: we call this phenomenon as piezoelectric effect. PFM detect the "*converse piezoelectric response*" of FE materials, i.e., local mechanical vibrations induced by an applied external ac field.

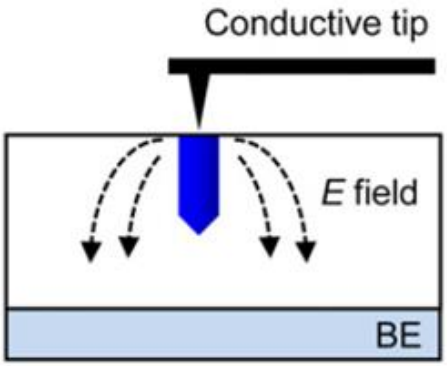

Figure 2.3 Sketch of domain nucleation in PFM. The dashed arrows indicate the electric field (denoted *E* field) lines. The solid needlelike (blue) figures show reversed domains (i.e., nuclei). The BE indicates the bottom electrode. Adapted from Yang *et al.* [10].

In conventional PFM, an ac bias, $V_{tip} = V_0 \sin\omega t$, is applied to a conductive tip of AFM

in contact with a bare surface of the sample (Figure 2.3). Here, the amplitude of V_0 should be smaller than the coercive voltage of FE materials. Then, the local piezoelectric strain s caused by V_{tip} is that $s = s_0 \sin(\omega t + \phi)$. The amplitude s_0 and phase difference ϕ yield the information on the magnitude of piezoresponse and the orientation of polarization in FE domains, respectively.

We used the piezoelectric force microscopy (PFM) to image the ferroelectric domains. The operation of PFM is usually based on the fact that when an external electric field is applied to a ferroelectric material, the z-deformation (i.e., vertical strain of the material) depends on the polarization direction. If the domain with upward polarization is vertically stretched for a applied electric field, then the domain with downward polarization is vertically squeezed. Thus, by using the PFM, we can clearly image the ferroelectric domains. Figure 2.4 shows the domain pattern in epitaxial $BiFeO_3/SrRuO_3$ on vicinal $SrTiO_3$ substrate, obtained with our PFM setup. Domains and domain wall are seen clearly in Figure 2.4.

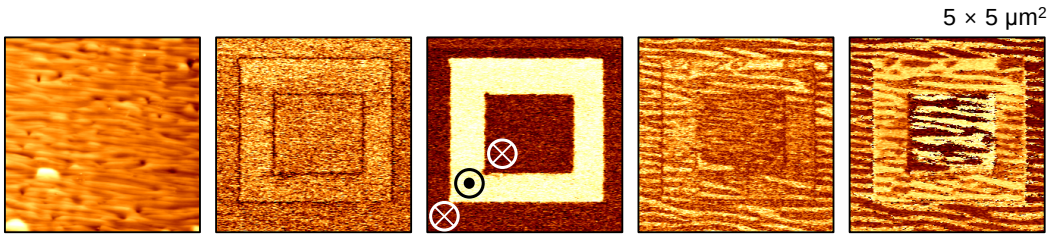

Figure 2.4 From left to right, topography, out-of-plane (OP) amplitude, OP phase, in-plane (IP) amplitude, and IP phase images of epitaxial $BiFeO_3$ thin film.

References

1. H. Kitahata, K. Tadanaga, T. Minami, N. Fujimura, and T. Ito, Japanese J. Appl. Phys. Part 1-Regular Papers Short Notes & Review Papers 38 (1999) 5448.
2. Y. Chye, T. Liu, D. Li, K. Lee, D. Lederman, and T. H. Myers, Appl. Phys. Lett. 88 (2006) 132903.
3. W. C. Yi, J. S. Choe, C. R. Moon, S. I. Kwun, and J. G. Yoon, Appl. Phys. Lett. 73 (1998) 903.
4. T. Yoshimura, N. Fujimura, N. Aoki, K. Hokayama, S. Tsukui, K. Kawabata, and T. Ito, Japanese Journal of Applied Physics Part 1-Regular Papers Short Notes & Review Papers 36 (1997) 5921.
5. D. B. Chrisey and G. K. Hubler, eds., Pulsed laser deposition of thin films,
6. G. K. Williamson, and W. H. Hall, Acta Metall. 1953, 1, 22.
7. J. I. Langford, D Louër, Rep. Prog. Phys. 1996, 59, 131.
8. G. Catalan, B. Noheda, J. McAneney, L. J. Sinnamon, J. M. Gregg, Phys. Rev. B 2005, 72, 020102(R).
9. M. Alexe and A. Gruverman, *Ferroelectrics at Nanoscale: Scanning Probe Microscopy Approach* (Springer, New York, 2004).
10. S. M. Yang, J.-G. Yoon, and T. W. Noh, Curr. Appl. Phys. 11, 1111 (2011).
11. A. Gruverman, O. Auciello, and H. Tokumoto, Annu. Rev. Mater. Sci. 28, 101 (1998).
12. S. Hong *et al*., J. Appl. Phys. 89, 1377 (2001).
13. S. V. Kalinin and D. A. Bonnell, Phys. Rev. B 65, 125408 (2002).

Chapter 3
The effect of the deposition temperature on the formation of defects in $BiFeO_3$ thin films

3.1 Introduction

$BiFeO_3$ (BFO) is a particularly interesting multiferroic material [1] and has two order parameters, ferroelectricity and antiferromagnetism. The ferroelectric and antiferromagnetic ordering temperatures are significantly greater than room temperature; the Curie temperature is 1103 K and the Néel temperature is 643 K [2,3]. Moreover, BFO has the largest remnant polarization of all known ferroelectrics of 100 μC cm^{-2} along the [111] direction [4]. These properties make BFO a promising ferroelectric material for applications including ferroelectric random-access memory [5], photovoltaics [6], and magnetoelectrics [7].

Recent studies of ferroelectric materials have shown that control over defects is important for tuning the physical and functional properties of ferroelectric devices. Lee *et al*. reported that multilevel data storage could be realized using BFO thin films via defect dipole engineering [5]. They further demonstrated active control of irreversible defect dipoles in BFO thin film without compromising the ferroelectricity [8]. More

recently, through site-specific substitutional alloying, Choi *et al*. showed that the band-gap of ferroelectric $Bi_4Ti_3O_{12}$ could be controlled without deterioration of the ferroelectric properties [9].

To obtain desired functionality using defect engineering in BFO thin films, an effective method to control the defect states is required. The site-engineering concept [10], which exploits the non-stoichiometric BFO target [11], and adjustment of the oxygen partial pressure [12] are useful techniques to control the defects in BFO thin films. It is also known that the deposition temperature, T_D, significantly affects defect formation in BFO films [13]. However, the evolution of defects depending on the small ranges of T_D in BFO films has not yet been carefully investigated. Moreover, the effects of defects on the functional properties of BFO films have been rarely studied. Therefore, a detailed investigation is required to understand the effects of T_D on the defect evolution in BFO thin films.

In this chapter, we investigated the evolution of defects in BFO films grown on (001) $SrTiO_3$ (STO) substrates as a function of T_D, which was varied over a narrow range of 570–600℃ in intervals of 10℃. X-ray diffraction (XRD) data of the BFO films grown at $T_D \geq 590$℃ exhibited Fe_2O_3 defect peaks, whereas those grown at $T_D \leq 580$℃ did not show any defect peaks. The presence of the defects in the BFO films grown at $T_D \geq 590$℃ was also investigated using optical spectroscopy. We found that the presence of defects was strongly correlated with changes in the surface morphology and ferroelectric properties of the BFO films. Well-aligned stripe patterns and nearly rectangular polarization–electric field (*P–E*) hysteresis loops were observed in the BFO

films grown at $T_D \leq 580$℃. However, the surface roughness abruptly increased and the *P–E* hysteresis loops showed leaky behavior in the films grown at $T_D \geq 590$℃. These results indicated that $T_D \sim 590$℃ was threshold temperature.

3.2 Experiments

3.2.1 Fabrication of $BiFeO_3$ thin films

We grew BFO thin films using pulsed laser deposition (PLD) [13]. The films were sandwiched between a Pt top electrode and a $SrRuO_3$ (SRO) bottom electrode. BFO/SRO thin-film layers were fabricated on STO substrates with a 4° miscut toward the [100] direction. To form the bottom electrode, the 20-nm-thick SRO layer was deposited at 650℃, the laser fluence was 2 J cm^{-2}, and the repetition rate was 2 Hz. The BFO thin films were deposited on top of the SRO bottom electrode at T_D = 570℃, 580℃, 590℃, and 600℃. For the top electrode, the Pt layer was photolithographically patterned to form the BFO capacitors.

3.2.2 Experimental setup and methods for characterization

The crystal structure of the BFO films was analyzed using high-resolution XRD (Bruker AXS D8 Advanced X-ray Diffractometer). Optical spectra were obtained using a VASE (J. A. Woollam) ellipsometer. The angle of incidence of the polarized light was 65°, 70°, and 75°. Ferroelectric *P–E* hysteresis loops were measured using a TF analyzer 2000 (AixACCT) at room temperature. The surface state of the BFO films was

measured using an atomic force microscope (AFM) (XE-100, Park systems).

3.3 Results and discussions

3.3.1 Investigation of defects

3.3.1.1 High-resolution X-ray diffraction

Figure 3.1 shows XRD θ–2θ scans of the BFO films grown at various T_D. For BFO films grown at 570℃ and 580℃, only the BFO (00*l*) peaks were present, indicating that the crystalline axes of the films were well-aligned and without impurities. In the BFO film grown at 590℃, an Fe_2O_3 peak at $2\theta \approx 49°$ appeared. The Fe_2O_3 peaks were more clearly identified at $2\theta = 24.2°$ and $2\theta = 49.4°$ in the BFO film grown at 600℃ [12].

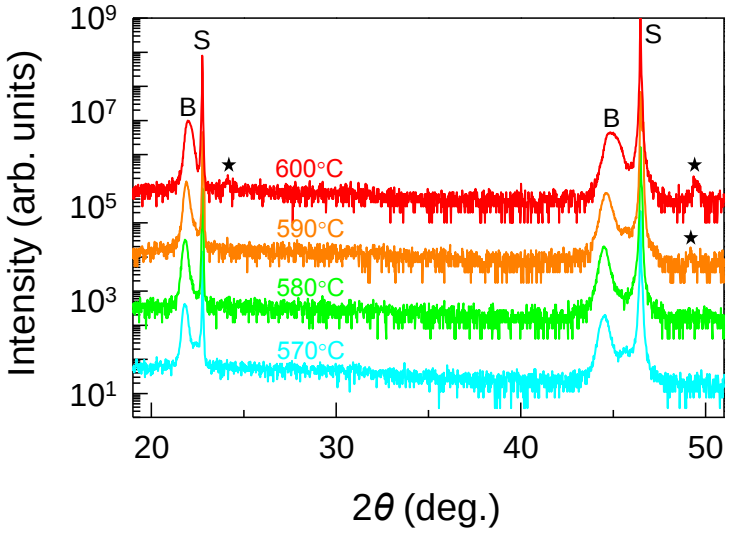

Figure 3.1 XRD θ–2θ scans of the BFO films grown at various T_D (from bottom to top T_D = 570℃, 580℃, 590℃, and 600℃). The peaks are indexed with the

following symbols: B: BFO, S: STO, ★: Fe_2O_3.

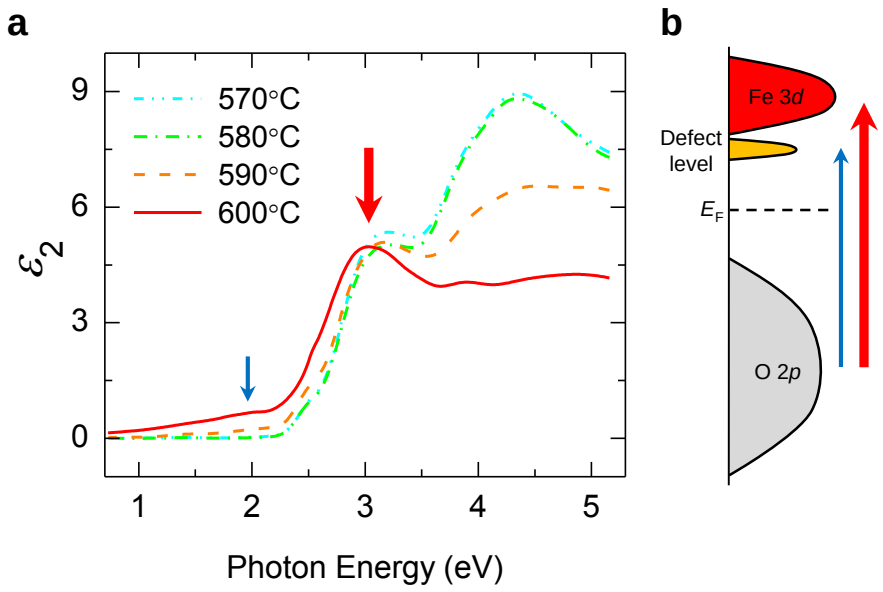

Figure 3.2 (a) The imaginary part of the dielectric function of the BFO films. (b) Schematic band diagram of the BFO thin films. The yellow band indicates the defect level. Peaks indicated by the blue and red arrows correspond to the optical transition from O 2*p* to defect and Fe 3*d* levels, respectively.

3.3.1.2 Optical spectroscopy

The appearance of defects can also be identified by optical spectroscopy experiments. For example, the defects states in STO thin films manifest as finite optical absorption below the fundamental band gap of STO [14]. Figure 3.2a shows the imaginary part of the dielectric function, ε_2, of the BFO films. The data were analyzed by considering

homogeneous BFO+Fe_2O_3 mixed layers. The overall spectral shapes of the dielectric functions for the BFO films grown at 570℃ and 580℃ were almost identical. The band gap estimated from the ε_2 data was 2.5 ± 0.2 eV. Pronounced peaks above 2.2 eV are attributed to dipole-allowed excitations from O 2*p* to Fe 3*d* bands (indicated by the red arrow in Fig. 3.2b), which is consistent with the results of both first-principles calculations and experiments [15–18]. We note that the spectral shape of ε_2 for the films grown at $T_D \geq 590$℃ were significantly different from those of the films grown at $T_D \leq 580$℃. Suppression of ε_2 at photon energies greater than 3.5 eV was observed, as shown in Fig. 3.3, which may be due to the increased surface roughness of these films. In addition, a weak absorption peak appeared around 2.0 eV, which is below the optical band gap of BFO. The weak absorption may result from optical transitions from the O 2*p* to localized defect levels, as depicted in Fig. 3.2b [19]. These optical data indicate that the defects appeared abruptly at $T_D = 590$℃, which is consistent with the XRD data, as shown in Fig. 3.1.

3.3.1.3 Atomic force microscopy

The presence of the defects affected the surface morphology of the BFO thin films. AFM measurements show that the surface roughness significantly increased with the appearance of the defects, as shown in Fig. 3.3. The surface of the BFO films grown at $T_D \leq 580$℃ exhibited well-ordered stripe patterns, which were nearly consistent with the pattern of the BFO film grown on the 4° miscut [100] $SrTiO_3$ substrate [20]. The films grown at $T_D \geq 590$℃ exhibited mosaic patterns and also exhibited a considerably larger

surface roughness than those grown at lower temperatures. Thus, we believe that important role of T_D includes robustness of sample stoichiometry by decreasing the propensity for volatile species to desorb and to maintain the step-flow growth up to threshold temperature.

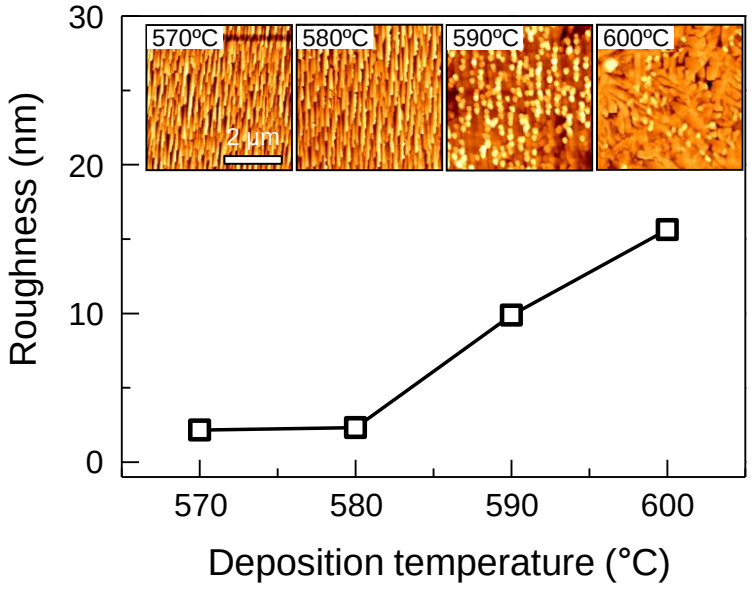

Figure 3.3 Surface roughness of the BFO films. The inset shows AFM images of the BFO films grown at various T_D.

3.3.2 Ferroelectric properties

The ferroelectric properties were also affected by the presence of the defects. Figure 3.4 shows *P*–*E* hysteresis loops of the BFO films. Note that the hysteresis loops of the BFO films grown at $T_D \leq 580$℃ were almost rectangular, indicating that the leakage currents were very small and that the polarization relaxation was not likely to occur. The BFO film grown at 590℃ was somewhat leaky, but the remnant polarization of the

film grown at 590℃ was almost the same as that of the films grown at $T_D \leq 580$℃. The BFO film grown at 600℃ exhibited a very large leakage current and the hysteresis loop lost the rectangular shape, as shown in the inset of Fig. 3.4.

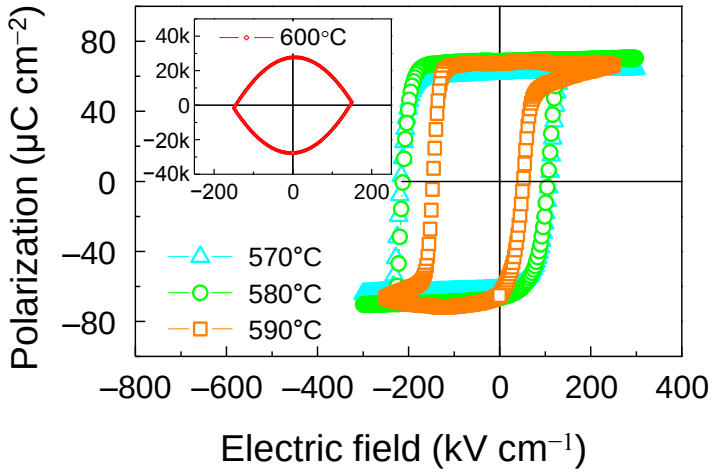

Figure 3.4 *P–E* hysteresis loops of the BFO films grown at various T_D. The inset shows *P–E* hysteresis loops of the BFO film grown at 600°C.

3.3 Conclusion

We controlled the formation of defects in BFO films by varying the substrate temperature during epitaxial growth over a narrow range of 570℃–600℃. We found that the presence of defects significantly affects the optical and ferroelectric properties. The BFO films grown at $T_D \leq 580$℃ had a band gap of 2.5 ± 0.2 eV and showed rectangular *P–E* hysteresis loops. Fe_2O_3 impurities appeared in the BFO films grown at $T_D \geq 590$℃, leading to weak absorption below the band gap and leaky *P–E* hysteresis

loops. Our work suggests that the defect evolution in BFO films critically depends on the deposition temperature.

References

[1] Wang J, Neaton JB, Zheng H, Nagarajan V, Ogale SB, Liu B, et al. Science 2003;299:17191.

[2] Smolenskii GA, Isupov, V, Agranovskaya A, Kranik N, Sov. Phys.–Solid State 1961;2:2651.

[3] Fischer P, Polomska M, Sosnowska I, Szymanski M, J. Phys. C 1980;13:1931.

[4] Ederer C, Spaldin NA, Phys. Rev. Lett. 2005, 95, 257601.

[5] Lee D, Yang SM, Kim TH, Jeon BC, Kim YS, Yoon JG. Adv. Mater. 2012; 24: 402.

[6] Ji W, Yao K, Liang YC, Adv. Mater. 2010;22:1763.

[7] Baek SH, Jang HW, Folkman CM, Li YL, Winchester B, Zhang JX, et al. Mater. 2010;9:309.

[8] Lee D, Jeon BC, Baek SH, Yang SM, Shin YJ, Kim TH, et al. Adv. Mater. 2012; 24: 6490.

[9] Choi WS, Chisholm MF, Singh DJ, Choi T, Jellison Jr GE, Lee HN, Nature Communications 2012;3:689.

[10] Qi X, Dho J, Tomov R, Blamire MG, MacManus-Driscoll JL, Appl. Phys. Lett. 2005;86:062903.

[11] Das RR, Kim DM, Baek SH, Eom CB, Zavaliche F, Yang SY, et al. Appl. Phys. Lett. 2006;88:242904.

[12] Béa H, Bibes M, Barthélémy A, Bouzehouane K, Jacquet E, Khodan A, et al. Appl. Phys. Lett. 2005;87:072508.

[13] Jeon BC, Lee D, Lee MH, Yang SM, Chae SC, Song TK, et al. Adv. Mater., 2013;25:5643.

[14] Kim YS, Kim J, Moon SJ, Choi WS, Chang YJ, Yoon JG, et al. Appl. Phys. Lett. 2009;94:202906.

[15] Neaton JB, Ederer C, Waghmare UV, Spaldin NA, and Rabe KM, Phys. Rev. B 2005;71:014113.

[16] Chen P, Podraza NJ, Xu XS, Melville A, Vlahos E, Gopalan V, et al. Appl. Phys. Lett. 2010;96:131907.

[17] Ihlefeld JF, Podraza NJ, Liu ZK, Rai RC, Xu X, Heeg T, et al. Appl. Phys. Lett. 2008;92:142908.

[18] Pisarev RV, Moskvin AS, Kalashnikova AM, Rasing Th, Phys. Rev. B 2009;79:235128.

[19] Yang CH, Seidel J, Kim SY, Rossen PB, Yu P, Gajek M, et al. Nature Mater. 2009;8:485.

[20] Jang HW, Ortiz D, Baek SH, Folkman CM, Das RR, Shafer P, et al. Adv. Mater. 2009;21:817.

Chapter 4
Flexoelectric effect in the reversal of self-polarization and associated changes in the electronic functional properties of epitaxial ferroelectric thin films

4.1 Introduction

4.1.1 Flexoelectric effect

Flexoelectric effect is the generation of an electric field by a strain gradient via electromechanical coupling. This effect was predicted theoretically by Kogan in 1964 [1] and experimentally observed by Bursian and Zaikovskii in 1968 [2]. The phenomenon was given the name 'flexoelectricity' by Indenbom *et al*. in 1981 [3]. Despite its long history, there has been little research on flexoelectricity of bulk solid materials [3-13], because its effects had been widely accepted to be quite small. Namely, the flexoelectric coefficients are small (10^{-10}–10^{-11} C m^{-1}) [12], and also the strain gradients generated by mechanical bending are quite small, typically on the order of 0.1 m^{-1} [13].

Recently, there has been much interest in flexoelectricity, especially regarding epitaxial thin films [14-20]. Inside these material systems, a strain gradient as large as 10^5–10^6 m^{-1} can be produced [14,15]. Note that this value of the strain gradient is 6 or 7

orders of magnitude larger than the corresponding bulk values. Using numerous epitaxial ferroelectric thin films, experimental studies showed that flexoelectricity can affect the domain configuration and imprint [15], dielectric constant [16,17], continuous rotation of the spontaneous polarization direction [18], polarization switching by mechanical force [19], and unusual coupling between electronic transport and the mechanical strain gradient [20],

4.1.2 Domain engineering in ferroelectrics

Domain engineering in ferroelectrics, ferromagnetics, and multiferroics, has been attracting worldwide attention recently, due to its functionality and ease of control [21-23]. Ferroelectric materials, in particular, are important due to their promising application [24-27] in such devices as ferroelectric random-access memory, photovoltaics [24], magnetoelectrics [25], and optoelectronic devices [27]. Since most of the functional properties of ferroelectrics are directly related to the electrically switchable polarization and domain configurations, the control of ferroelectric polarization states has been the main concern in ferroelectric community [28,29]. Especially, $BiFeO_3$ (BFO) is more interesting than any other ferroelectrics, due to its room temperature multiferroics and large Pb-free piezoelectrics [30]. By controlling the domain structure in BFO films, for example, Yang and co-workers reported photovoltages that were significantly higher than the electronic band-gap [24]. Observation of the domain wall conductivity in BFO thin films has emphasized the importance of controlling domain configuration and polarization state, which can lead to a new device concept using ferroelectrics [26].

Unfortunately, BFO films can have very complicated domain structures, depending on the substrates [31]. Recently, several studies have tried to control the ferroelectric domain structures of BFO films by varying the substrates [21], miscut directions [32], and orientations [23]. In particular, as-grown ferroelectrics thin films (including BFO) have a self-poled domain state (i.e., self-polarization) when deposited on oxide electrodes, such as $SrRuO_3$ (SRO) and doped manganites [22,23,33]. The determination of the as-grown polarization state is critical for full utilization of the BFO thin films, because the polarization state affects the defect configuration, and, in turn, the ferroelectric hysteresis and electronic transport.

4.1.3 Self-polarization in ferroelectric thin films

Many ferroelectric films were reported to have one preferred polarization direction just after deposition [21-23,33-37]. This phenomenon, known as a self-polarization, has been attributed to a built-in electric field. Numerous origins have been proposed for the built-in electric field, namely, defects [34], piezoelectricity [35], interfacial electrode effects [22,33], and so on. Specifically for BFO thin films, most of the earlier research showed that the as-grown films usually exhibited downward self-polarization [22,23,33]. Here, I show how flexoelectricity can reverse the direction of the as-grown polarization in epitaxial BFO thin films grown on a vicinal $SrTiO_3$ (STO) substrate with an SRO bottom electrode. Additionally, the change in the self-polarization could result in large variations of the functional properties of the as-grown BFO films, including ferroelectric hysteresis and diode behavior.

4.2 Experiments

4.2.1 Sample perperation

We used high-quality BFO epitaxial thin films with thicknesses varying from 50 to 250 nm. The films were sandwiched between a Pt top electrode and a single crystal SRO bottom electrode. BFO/SRO thin-film layers were fabricated using pulsed laser deposition (PLD) onto STO (001) single-crystal substrates, with a 4° miscut toward the [100] direction. To form the bottom electrode, an SRO layer (20-nm-thick) was deposited onto an STO substrate by PLD at 650℃. The target-substrate separation was 2 inches. An oxygen pressure of 100 mTorr was maintained. The laser fluence and repetition rate were 2 J cm^{-2} and 2 Hz, respectively. The BFO thin film was grown on top of the SRO bottom electrode by PLD over a temperature range of 550 to 600℃. A stoichiometric BFO ceramic target was used. The deposited BFO film was postannealed in situ inside the PLD chamber at the deposition temperature for 1 hour under an oxygen atmosphere of 760 Torr. For the top electrode, a Pt layer (40-nm-thick) was deposited at room temperature by sputter deposition. After the deposition, the Pt layer was photolithographically patterned to form the BFO capacitors. Pt top electrodes consisted of 10 to 200-μm square patterns.

4.2.2 Characterization of crystal structures

The crystal structures of the BFO films were analyzed using high-resolution X-ray

diffraction (D8 Advanced, Bruker AXS). To evaluate the in-plane strain states, we used reciprocal space mapping analysis of $\{\bar{1}03\}$ family peaks with various phi angles (0°, 90°, 180°, and 270°). The average *a*-axis lattice constant was calculated from the average value of the BFO $(\bar{1}03)$ and (103) peak. The average *b*-axis lattice constant was determined from the BFO $(0\bar{1}3)$ peak value for ϕ = 90°. The average *c*-axis lattice constant was obtained from the θ–2θ data.

4.2.3 Piezoresponse force microscopy

The piezoresponse force microscopy (PFM) measurements were performed using an XE-100 (Park systems) with commercially available Pt/Ir-coated Si tips (PPP-EFM, Nanosensors). For PFM imaging, we applied an AC voltage of 1.0 Vrms at 17.1 kHz to the bottom electrode (i.e., sample bias). We measured the amplitude and phase signals of the converse piezoelectric responses with a lock-in amplifier (SR830, Stanford Research Systems).

4.2.4 Electrical measurements

Ferroelectric polarization–voltage (*P*–*V*) hysteresis loops were measured using a TF analyzer 2000 (AixACCT) at room temperature. We performed current density–voltage measurements at room temperature using a low-noise probe station and a picoampere meter (Keithley 236). A +12 V (−12 V) external-poling voltage was applied to the uniaxially strained (relaxed) BFO capacitor to obtain the downward (upward) polarization state; a −12 V (+12 V) external-poling voltage resulted in upward (downward)

polarization.

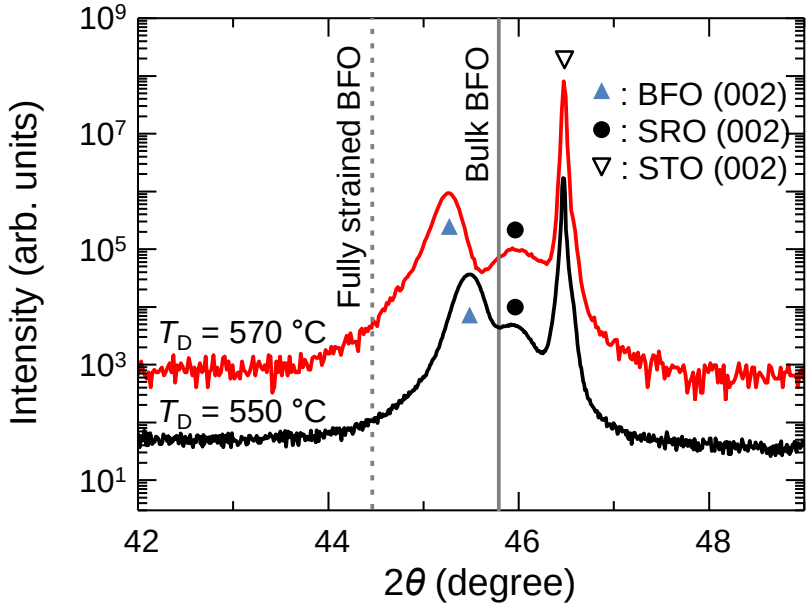

Figure 4.1 XRD θ–2θ scans of the 250-nm-thick BFO films grown at 570°C (solid red line) and 550°C (solid black line) on vicinal STO (001) substrates. The gray short-dashed and solid vertical lines indicate the (002) diffraction peak positions of the fully strained and relaxed BFO films on STO substrates, respectively.

4.3 T_D effect in $BiFeO_3$ thin films

4.3.1 Uniaxially strain and relaxed $BiFeO_3$ thin films

Figure 4.1 shows the XRD θ–2θ scan for 250-nm-thick BFO films grown at 570°C and 550°C. For these films, only the BFO (00l) peaks appear, indicating that the crystalline axes of the films were well-aligned. The BFO (002) peaks for both the films

were located between the predicted positions for the fully strained BFO film and bulk BFO, shown as the dotted and solid lines, respectively. This indicated that some structural relaxation occurred for both the films. Additionally, the BFO (002) peak position of the film grown at 550 ℃ was closer to the bulk BFO value, indicating that this film became more relaxed along the [001] direction than that grown at 570℃.

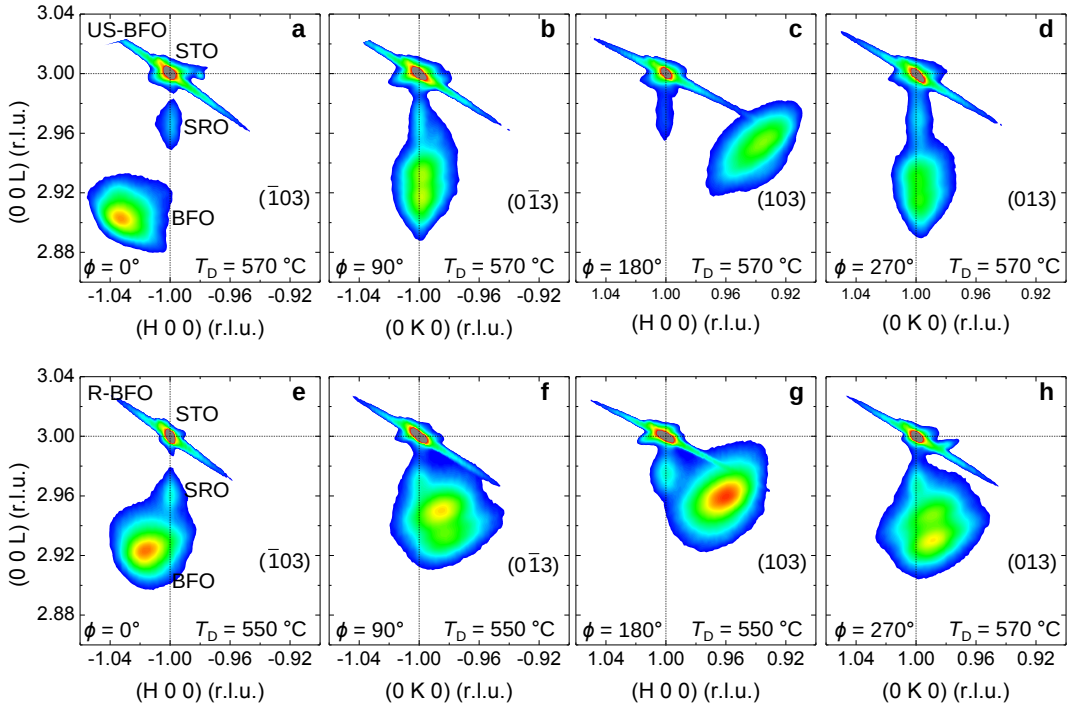

Figure 4.2 RSMs around the $\{\bar{1}03\}$ STO Bragg family of peaks with various ϕ angles for 250-nm-thick US- and R-BFO films. The $(\bar{1}03)$, (103), $(0\bar{1}3)$, and (013) peaks can be distinguished from each other in the RSM data, due to the large rhombohedral distortion of the BFO unit cell [22].

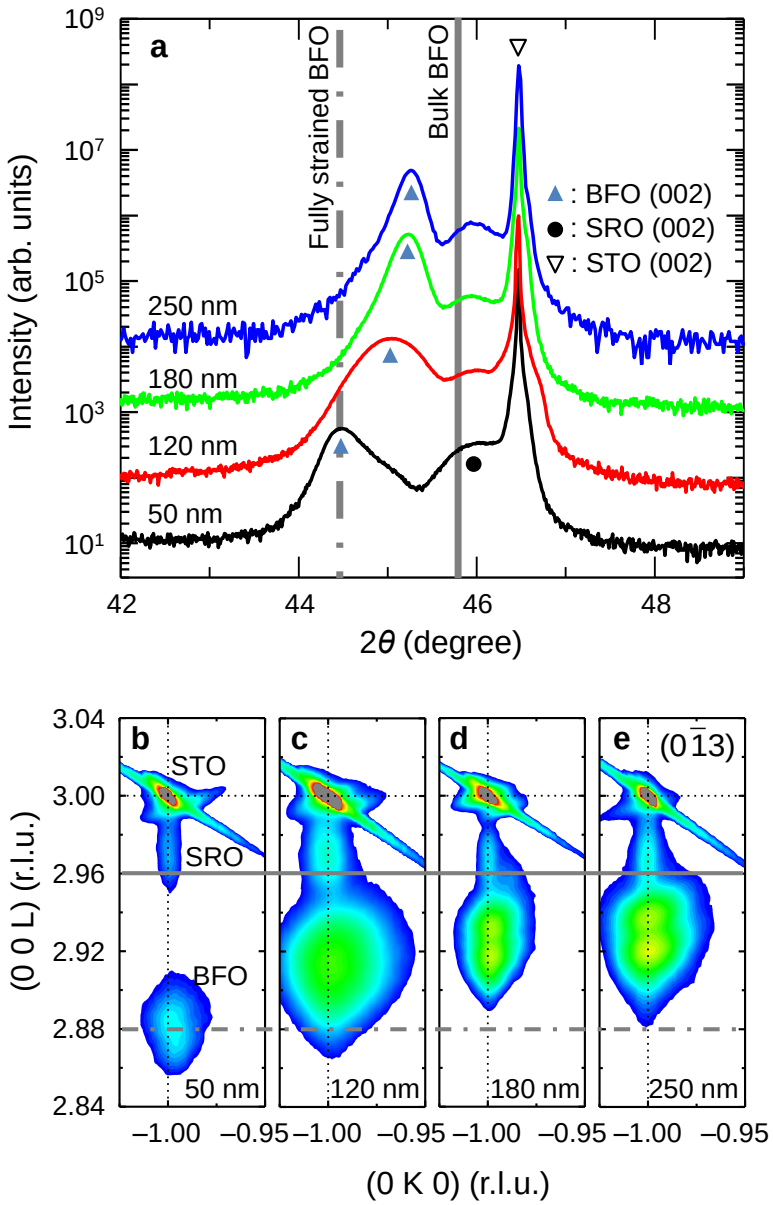

Figure 4.3 (a) HRXRD θ–2θ scans of BFO films grown at 570°C between 50 and 250 nm thick. The closed blue triangles, black circles, and open-inverted triangles indicate the (002) peaks of BFO, SRO, and STO, respectively. The gray dash-dotted and solid lines indicate the (002) diffraction peak positions of the fully strained and

relaxed BFO films on STO substrates, respectively. The θ–2θ scans show that the 50-nm-thick film is fully strained in the [001] direction. However, above a critical thickness, the strain should start to relax. As the film thickness increased, the 2θ peak position moved to larger angles, indicating that the average *c*-axis lattice constant became smaller. (b)–(e) RSM images around the $(0\bar{1}3)$ STO Bragg peaks of BFO films grown at 570°C between 50 and 250 nm thick. As displayed in the RSM data, all of these films were fully strained along the [010] direction; i.e., they should be US-BFO films.

Although deposition temperature (T_D) differed by only 20℃, we found that our BFO thin films had different strain relaxation behaviors. To obtain information on the in-plane strain state, we used reciprocal space mapping (RSM) analysis of the {103} family of BFO peaks with various ϕ angles for the 250-nm-thick BFO films, as shown in Figure 4.2 [22]. The (013) and $(0\bar{1}3)$ BFO Bragg peaks for the film grown at 570℃ are located near the vertically dotted line, indicating that this film was almost fully strained along the [010] direction, while the $(\bar{1}03)$ and (103) BFO Bragg peaks were located outside of the vertically dotted line, as shown in Figures 4.2(a)-(d), indicating that this film was relaxed along the [100] direction. From here on, the films grown at 570℃ will be referred to as uniaxially strained BFO (US-BFO) films. Figures 4.2(e)-(f) show the RSM results for the film grown at 550℃. Note that the {103} family of peaks are located outside of the vertically dotted line, indicating that the film was relaxed in all directions; these films will be referred to as relaxed BFO (R-BFO) films.

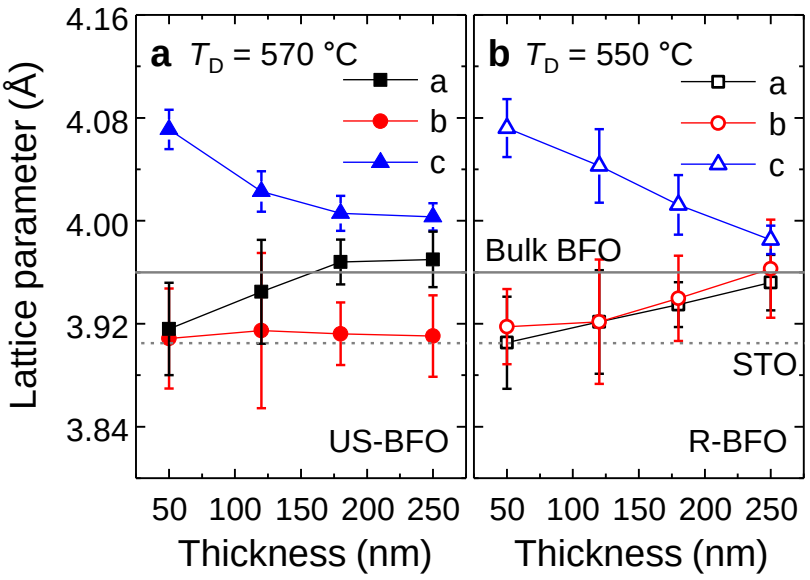

Figure 4.4 (a) and (b) Pseudocubic lattice parameters as a function of the film thickness for US- and R-BFO films, respectively. The solid and dotted gray lines represent the lattice parameter of bulk BFO and STO, respectively.

4.3.2 Thickness & T_D-dependent lattice relaxation

To obtain further information on how strain developed in the US-BFO films, we deposited four BFO films at 570℃ with four different thicknesses of 50, 120, 180, and 250 nm. The 50-nm-thick film is fully strained in the *ab*-plane. As the film thickness increased, the average value of the *c*-axis lattice constant decreased, but the *b*-axis lattice constant remained constant, as shown in Figure 4.3. We determined the average values of all the lattice constants from the θ–2θ and RSM data. The results are shown in Figure 4.5(a). Note that the average value of the *b*-axis lattice constant was independent of the film thickness and nearly the same as that of the STO substrate. Because the *b*-axis

corresponds to the direction of step edges in STO substrates, the uniaxially strained growth behaviors should originate from clamping effects of the US-BFO films at the STO step edges.

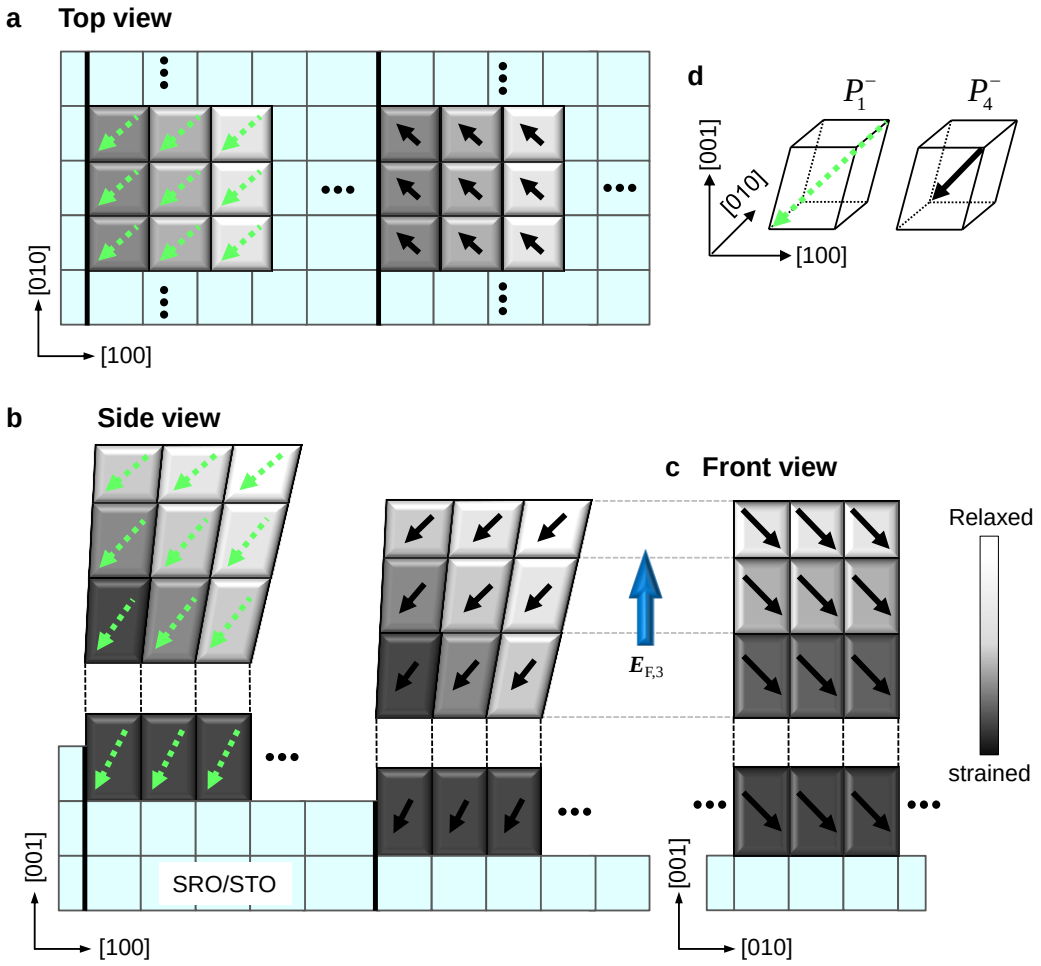

Figure 4.5 Schematic representation of the direction of the strain relaxation for US-BFO films. The dark and pale gray areas represent strongly strained and relaxed BFO regions, respectively. (a), (b), and (c) indicate the schematic diagram top, side, and front views of the US-BFO film, respectively. The large blue arrow indicates the

direction of vertical flexoelectric field ($E_{F,3}$). The green-dotted and black solid-line arrows indicate the direction of ferroelectric polarization, P_1^- and P_4^-, respectively. (d) Possible orientations of the polarization for US-BFO films on vicinal STO substrates. The step-bunching process and lattice dislocations (higher-order terms) are neglected in this representation. Recently, we demonstrated that in BFO films grown on vicinal STO substrates, some structural relaxation can occur through the step-bunching process and lattice dislocations [38]. However, because the resulting crystallographic tilt angle and the *c*-axis lattice constant should be higher-order variations, we neglected such effects in the schematic diagram [38]. To make the strain gradient more visible, we exaggerated the difference in the length scale of the BFO unit cells.

Based on the structural data, we proposed a schematic diagram of the US-BFO films, as shown in Figure 4.5. According to our RSM analysis, the US-BFO films were strongly clamped along the [010] direction. Along that direction, the lattice constant of the in-plane BFO near the substrate might be the same as that of the substrate. Experimentally, we found that this as-grown film should have a downward polarization. With the preferential distortion of the BFO unit cells on the miscut STO substrate, only two polarization variants, P_1^- and P_4^- are possible [32].

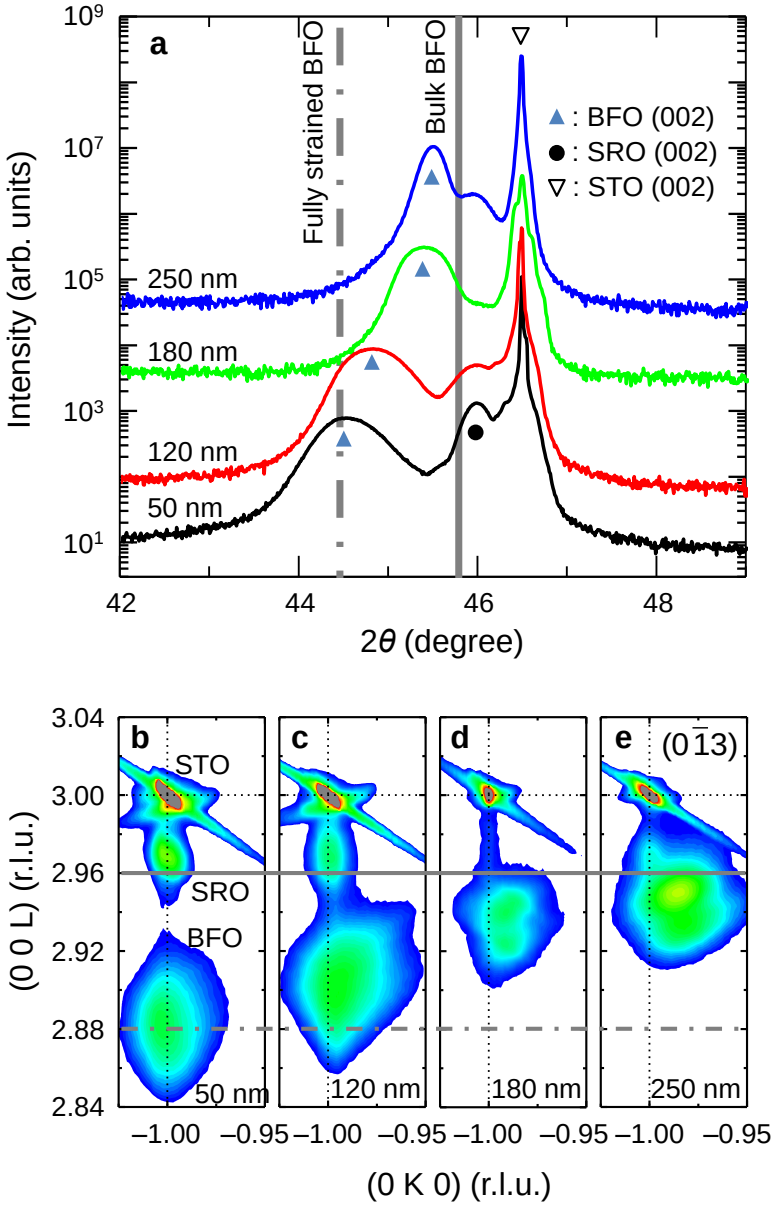

Figure 4.6 (a) XRD θ–2θ scans of BFO films grown at 550°C between 50 and 250 nm thick. The closed blue triangles, black circles, and open-inverted triangles indicate the (002) peaks of BFO, SRO, and STO, respectively. The gray dash-dotted and solid lines indicate the (002) diffraction peak positions of the fully strained and relaxed

BFO films on STO substrates, respectively. The θ–2θ scans show that the 50-nm-thick film is fully strained. However, above a critical thickness, the strain should start to relax. As the film thickness increased, the 2θ peak position moved to larger angles, indicating that the average *c*-axis lattice constant became smaller. (b)–(e) RSM images around the $(0\bar{1}3)$ STO Bragg peaks of BFO films grown at 550°C between 50 and 250 nm-thick. As displayed in the RSM data, the 50-nm-thick BFO film is fully strained. Above the critical thickness, the films were relaxed; i.e., they should be R-BFO films.

To obtain information on the strain evolution of R-BFO films, we also deposited four BFO films at 550 ℃ with thicknesses of 50, 120, 180, and 250 nm. Their XRD θ–2θ and RMS data are shown in Figure 4.6. Similar to the US-BFO case, this 50-nm-thick film was fully strained in the *ab*-plane. However, above a critical thickness, all of the thicker films became relaxed along the *b*-axis as well as along the *a*-axis, contrary to the US-BFO films. Figure 4.4(b) shows the average values of their lattice constants, evaluated from XRD data. These data showed that the strain relaxation occurred progressively in all directions. Although T_D was lower by only 20 ℃, compared with that of the US-BFO films, the step edges of the STO substrate could not clamp the BFO layer effectively in the R-BFO films.

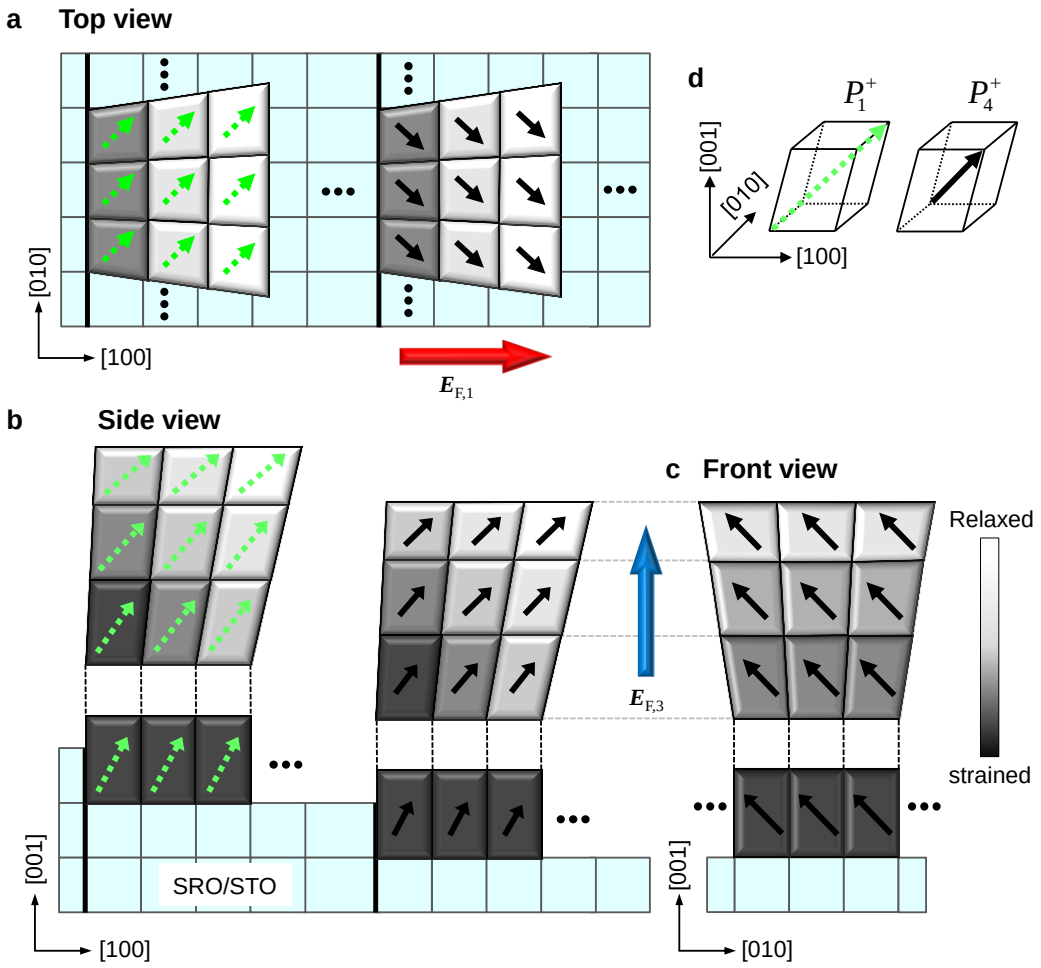

Figure 4.7 Schematic diagram of the direction of the strain relaxation for R-BFO films. The dark and pale gray areas represent strongly strained and relaxed regions, respectively. (a), (b), and (c) Schematic diagram top, side, and front views, respectively. The large red and blue arrows indicate the direction of the horizontal ($E_{F,1}$) and vertical ($E_{F,3}$) flexoelectric fields, respectively. (d) Possible polarization orientation for R-BFO films. The green-dotted and black solid-line arrows indicate

the direction of ferroelectric polarization, P_1^+ and P_4^+, respectively. The step-bunching process and lattice dislocations (higher-order terms) are neglected in this representation [38].

Figure 4.7 shows our proposed schematic diagram of the strain states of R-BFO films. Near the substrate, the BFO layers were fully strained. However, above the critical thickness, strain relaxation should occur in all directions. It should be noted that the *b*-axis lattice near the step edge could be somewhat more strained than those far from the step edge due to the clamping effect, as shown in Figure 4.7a. As a result, there should be an expansion of the *b*-axis lattice constant along the [100] direction. This strain gradient, $\partial u_{22}/\partial x_1$, will generate a horizontal electric field by flexoelectricity (large red arrow in Figure 4.7a). Note that u_{jk} and x_i are the strain and spatial coordinates of the film (*i*, *j*, and *k* = 1, 2, and 3) [4,7]. Additionally, there should be vertical electric fields due to $\partial u_{11}/\partial x_3$, $\partial u_{22}/\partial x_3$, and $\partial u_{33}/\partial x_3$ (large blue arrow in Figure 4.7c), which come from the relaxation of the *a*-, *b*-, and *c*-axis lattice constants along the [001] direction. Note that the $\partial u_{22}/\partial x_1$ and $\partial u_{22}/\partial x_3$ terms can appear only for the R-BFO films. We argue that these new strain gradient terms could reverse the downward self-polarization direction of R-BFO films to an upward self-polarization.

4.4 Mechanism of self-polarization

4.4.1 As-grown domain state in $BiFeO_3$ thin films

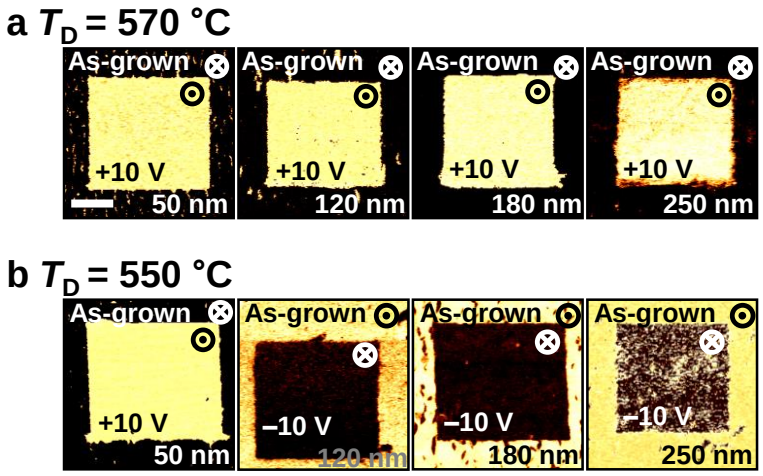

Figure 4.8 (a) and (b) Out-of-plane PFM images with 50-, 120-, 180-, and 250-nm-thick BFO films. The bright yellow and dark regions indicate the up- and down-polarization states, respectively.

To measure the self-polarization direction, we performed piezoresponse force microscopy (PFM) experiments. The as-grown BFO films deposited at 570 ℃ always had downward self-polarization, irrespective of whether they were fully or uniaxially strained (Figure 4.8a). In contrast, the film deposited at 550 ℃ with a thickness of 50 nm, was fully strained and had downward self-polarization (the first picture of Figure 4.8b). However, as the film thickness increased, the self-polarization direction changed from down to up (Figure 4.8b). These results indicate that the polarization direction of the as-grown films is not determined by particular defects, but depends on the film thickness and strain relaxation. Note that the structural change from fully strained to the relaxed state also occurred for thicknesses in the range of 50 to 120 nm, as shown in Figures 4.4a and

4.4b. Namely, the change in the self-polarization direction seems to be closely related to change of the strain state for R-BFO films. Moreover, we measured polarization–voltage (*P*–*V*) hysteresis loops and found that the imprints of the R-BFO films with thickness larger than 100 nm were opposite to those of the US-BFO films, as shown in Figure 4.9, in consistent with changes in the self-polarization direction.

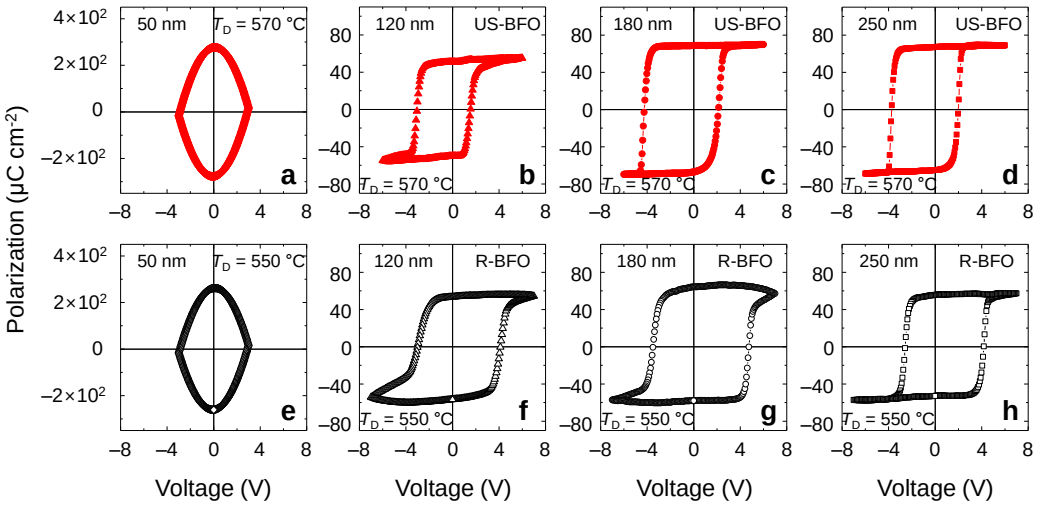

Figures 4.9 *P*–*V* loops for (a) 50-, (b) 120-, (c) 180-, and (d) 250-nm-thick BFO films grown at 570 °C; (e) 50-, (f) 120-, (g) 180-, and (h) 250-nm-thick BFO films grown at 550 °C. The 50-nm-thick BFO films exhibited a leaky behavior. The 120-, 180-, and 250-nm-thick US-BFO (R-BFO) films showed negative (positive) imprint characteristics. These imprint behaviors were nearly consistent with thickness dependence of self-polarization direction, as shown in the PFM images of Figures 4.8a and 4.8b.

4.4.2 Reversal of self-polarization in $BiFeO_3$ thin films

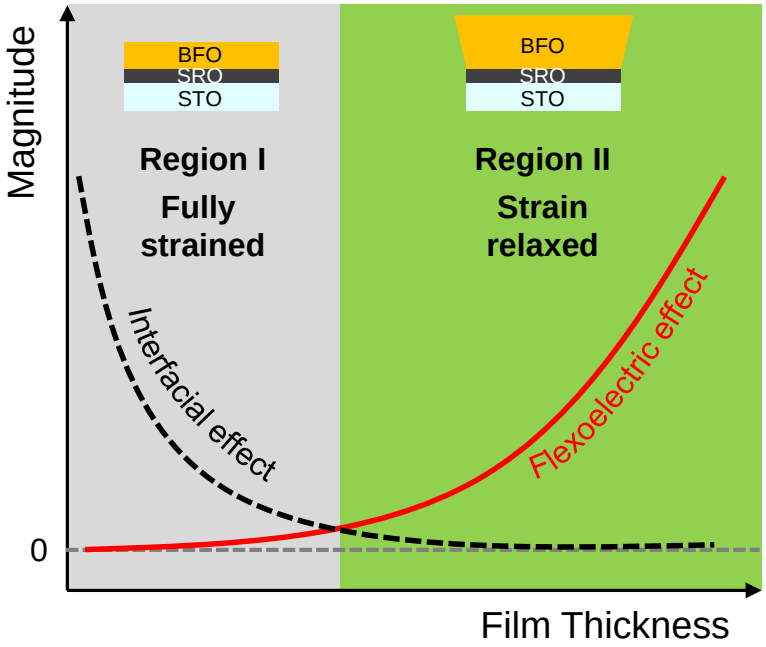

Figure 4.10 Magnitude of the flexoelectric and interfacial effects as a function of film thickness. The red and black-dashed curves indicate the flexoelectric and interfacial effects, respectively. The right and left insets indicate the fully strained and relaxed BFO films, respectively.

To explain the reversal of the self-polarization mechanism, we suggested a schematic diagram, as shown in Figure 4.10. Recently, Yu *et al*. demonstrated that the self-polarization direction could be engineered by varying the termination layer of the bottom electrode [33]. Balke *et al*. reported that the self-polarization direction is determined by the internal field produced by the different interface charges [37]. Note that both the fully strained and US-BFO films always had downward self-polarization because of the dominant interfacial electrode effect, in agreement with earlier reports [22,23,33].

However, for our R-BFO films, we propose that the above-mentioned additional strain gradient terms, i.e., $\partial u_{22}/\partial x_1$ and $\partial u_{22}/\partial x_3$, can generate the electric fields by flexoelectricity. With an increase in the film thickness, this flexoelectric effect should compete with the interfacial effects.

4.5 Estimation of flexoelectric field

4.5.1 Williamson-Hall plot

To obtain more quantitative information, we estimated the values of the out-of-plane and in-plane strain gradients using Williamson-Hall (W-H) plot [17,39]. The W-H plots of BFO films were obtained from the XRD θ–2θ and RSM peak widths [39], as shown in Figure 4.11. To obtain the out-of-plane gradual change of strain, four peaks–(001), (002), (003), and (004)–were selected from the XRD θ–2θ data. The numerical values of ε_{I} were determined from the slope of the fit equation [17,39,40].

$$\beta \cos\theta = \frac{K\lambda_w}{D} + 4\varepsilon_{\mathrm{I}} \sin\theta$$

where $\beta = \beta_{\mathrm{measured}} - \beta_{\mathrm{instrument}}$, and $\beta_{\mathrm{measured}}$ is the measured line width of the diffraction peaks of the samples, $\beta_{\mathrm{instrument}}$ is estimated from the peak width $\beta_{\mathrm{substrate}}$ of a nearby substrate peak,[S4] λ_w = 1.5406 Å is the x-ray wavelength, D is the coherence length along the scattering vector, K is a geometrical constant which was taken as 1. Figure 4.11 shows the plots of $4\sin\theta$ vs $\beta\cos\theta$. Out-of-plane ε_{I} for the US- and R-BFO films are 0.37 % and 0.46 %, respectively. From the out-of-plane ε_{I} values, we estimated the out-

of-plane strain gradients as -0.5×10^5 m^{-1} and -0.7×10^5 m^{-1} for the US- and R-BFO films, respectively.

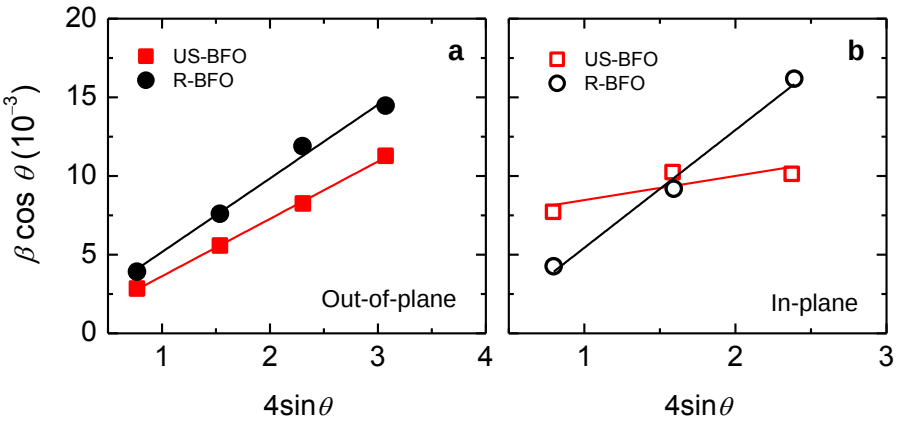

Figure 4.11 (a) Out-of-plane and (b) in-plane W-H plots for the inhomogeneous strain of the BFO films.

Similarly, we estimated the in-plane ε_I of the BFO films (Figure. 4.11b). To obtain the in-plane ε_I, we used the line width in the *k*-direction of the RSM peaks–(013), (023), and (033)–of BFO and STO for US- and R-BFO films. From the W-H plots for the width of those peaks, the in-plane ε_I was estimated to be 0.15 % and 0.74 % for the US- and R-BFO films, respectively. From these in-plane ε_I values, we determined the in-plane strain gradients as 0.2×10^5 m^{-1} and 1.9×10^5 m^{-1} for the US- and R-BFO films, respectively.

4.5.2 Estimation of strain gradient and flexoelectric field

We estimated the out-of-plane strain gradient along [001], which correspond to $\partial u_{33}/\partial x_3$, as -0.5×10^5 m^{-1} and -0.7×10^5 m^{-1} for the US- and R-BFO films, respectively.

We also estimated the in-plane strain gradients to be 0.2×10^5 m^{-1} and 1.9×10^5 m^{-1} for the US- and R-BFO films, respectively. With the experimentally obtained values of strain gradient, we could estimate the flexoelectric fields, $E_{F,i}$ (i = 1, 2, and 3), using[15,19,20]

$$E_{F,i} \approx \lambda \frac{e}{\varepsilon_0 a_j} \frac{\partial u_{jk}}{\partial x_i} \quad \text{(a)}$$

where λ is a scaling factor, e is the electronic charge, a_j is the lattice constant, and ε_0 is the permittivity of free space. Usually, in perovskite oxide systems, λ is known to have a value on the order of 10^0 or 10^1 (e.g., λ = 0.725 and 14.5 for $PbMg_{1/3}Nb_{2/3}O_3$ and $Ba_{0.67}Sr_{0.33}TiO_3$, respectively) [41]. To the best of our knowledge, the precise value of λ is not known yet for BFO. By assuming λ = 1, we estimated $E_{F,1}$ for R-BFO to be ~ 8.7 MV m^{-1}, while $E_{F,1}$ for US-BFO was estimated to be one order of magnitude weaker than that of the R-BFO. Similarly, we could estimate the vertical magnitude of the flexoelectric field, $E_{F,3}$ to be 2.3 MV m^{-1} and 3.2 MV m^{-1} for US-BFO and R-BFO, respectively. The ferroelectric polarization in BFO is [111]-oriented; thus, the effect of both the vertical and horizontal components of the flexoelectric field should be considered with regard to polarization reversal. As a result, the flexoelectric field in R-BFO is much higher, compared with that of the US-BFO film. Additionally, the estimated magnitude of the flexoelectric field in R-BFO gradually became comparable to that of the coercive field for BFO at high temperatures, during the growth [41]. Therefore, the flexoelectric effect should play an important role in reversing the self-polarization direction in R-BFO films.

4.6 Control of electronic functional properties

4.6.1 Configuration of defects

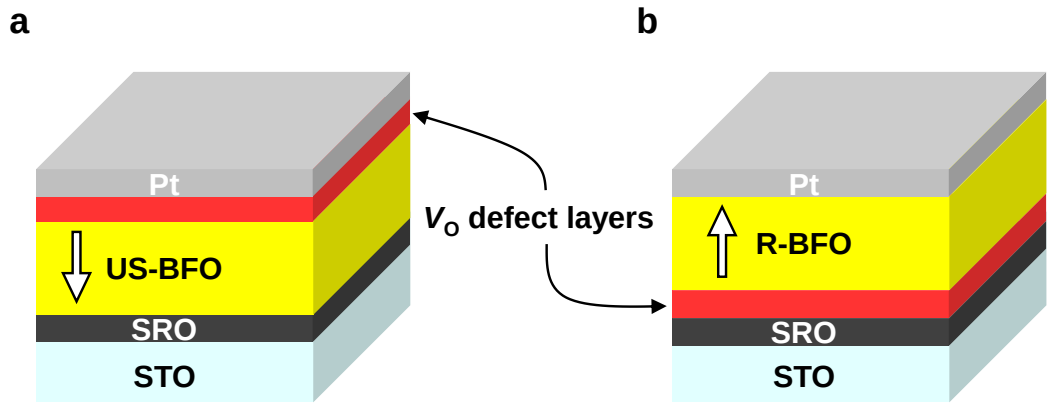

Figure 4.12 (a) and (b) Schematic diagram of the location of the V_O-rich defect layer in US- and R-BFO films, respectively. The large white arrows represent the as-grown polarization direction.

It is well known that the configuration of defects, such as oxygen vacancies, V_O, in ferroelectric films can be determined by the polarization state, especially at high growth temperatures [29,42,43]. Because BFO has a very high Curie temperature of 830 ℃, our BFO films should be in a ferroelectric state during the growth process. Thus, the generated self-polarization will drive V_O to one of the interfacial regions to compensate for the negative polarization charge during the growth [42]. For US- and R-BFO films, an interfacial V_O-rich defect layer formed at the top and bottom interfaces, respectively, as shown in Figure 4.12a and 4.12b. Additionally, to satisfy the lowest energy configuration

in the ferroelectric material, the defect dipoles (D_{defect}) should be aligned along the spontaneous polarization direction during the growth, resulting in imprint [29,43]. The different location of the V_O-rich defect layer and alignment of D_{defect} can result in changes of diode characteristics and ferroelectric hysteresis, respectively.

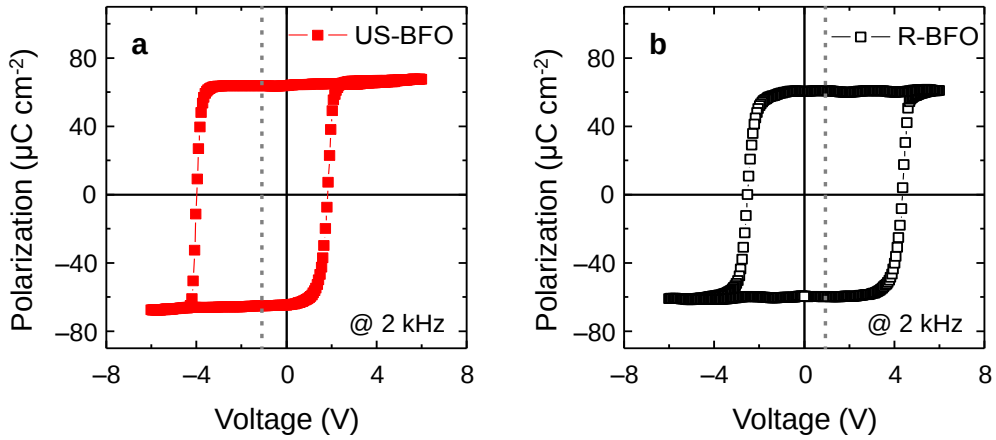

Figure 4.13 (a) and (b) *P–V* hysteresis loops of the US-and R-BFO films, respectively. Vertical gray-dashed lines indicate the voltage center of hysteresis loops.

4.6.2 *P–V* hysteresis loops

To confirm the configuration of the D_{defect} alignment to the imprint, we measured the *P–V* hysteresis loops for 250-nm-thick US- and R-BFO films, as shown in Figure 4.13a and 4.13b. The remnant polarization values along the [001] pseudocubic direction were nearly the same, i.e., approximately 65 and 60 μC cm−2, respectively [21,32]. Figure 4.13a shows a US-BFO film with a negative imprint; namely, its coercive voltages are +1.9 V for a positive bias and −4.0 V for a negative bias. In contrast, the R-BFO film

shows a positive imprint; namely, its coercive voltages are +4.4 V for a positive bias and −2.5 V for a negative bias, as-shown in Figure 4.13b. The two BFO films exhibited different imprint characteristics, as expected.

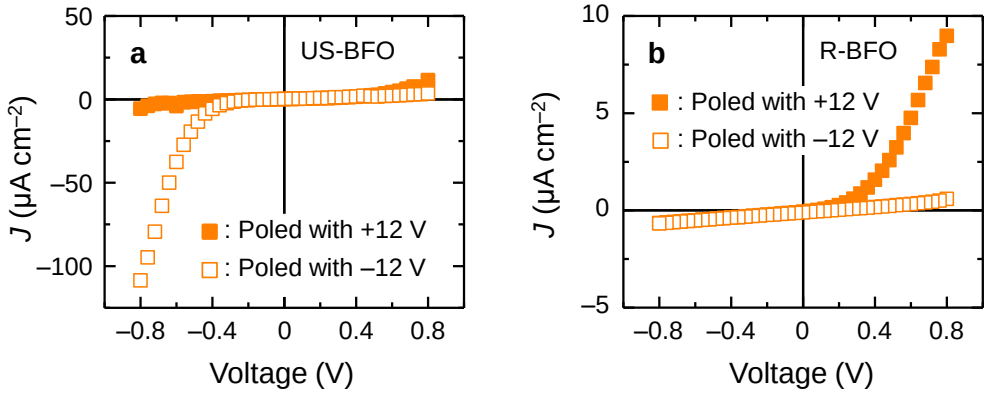

Figure 4.14 (a) and (b) *J–V* curves of US- and R-BFO films, respectively.

4.6.3 Electronic transport characteristics

Additionally, it is already known that the defect layers at the interface can affect the transport properties such as diode behavior [42]. We measured the current density–voltage (*J–V*) curves for 250-nm-thick US- and R-BFO films. Figure 4.14a shows that the *J–V* curves for the US-BFO film measured between −0.8 and +0.8 V, which were much smaller than the coercive voltages [42]. The small sweep voltage range ensured that no polarization switching occurred during the measurements. In the case of an ideal BFO capacitor, the hole carriers can be injected from the electrodes when a positive bias is applied. However, if the defective layer is located at the interface, it could disturb the carrier injection process. With a negative poling (i.e., a single domain of upward

polarization), the *J–V* curve exhibited reverse diode behavior. Conversely, with positive poling (i.e., a single domain of downward polarization), the *J–V* curve did not show any diode behavior for the US-BFO film. On the other hand, for the R-BFO film, the *J–V* curve should exhibit forward diode behavior with a positive poling. Conversely, with negative poling, the *J–V* curve did not show any diode behavior. Such *J–V* curves were actually observed, as shown in Figure 4.14b.

4.7 Conclusion

In summary, we found that the flexoelectric effects can play an important role in determining the self-polarization direction in the BFO thin films. We could successfully control the strain evolution of the films by varying the deposition temperature and the film thickness. Then, due to flexoelectric effects, the different strain gradient states inside the BFO films could create different built-in electric fields, which resulted in changes in the self-polarization direction. In addition, the self-polarization field could also produce large variations in the imprint and diode characteristics of the as-grown BFO films by generating a defect layer and aligning the defect dipoles during the film deposition process. Thus, strain gradient engineering at the nanoscale can potentially provide exciting new opportunities to realize flexoelectricity-based devices.

References

[1] S. M. Kogan, *Sov. Phys. Solid State* **1964**, *5*, 2069.

[2] E. V. Bursian, O. I. Zaikovskii, *Sov. Phys. Solid State* **1968**, *10*, 1121.

[3] V. L. Indenbom, E. B. Loginov, M. A. Osipov, *Kristallografiya* **1981**, *26***,** 1157.

[4] A. K. Tagantsev, *Phys. Rev. B* **1986**, *34*, 5883.

[5] W. Ma, L. E. Cross, *Appl. Phys Lett.* **2001**, *78*, 2920.

[6] R. Resta, *Phys. Rev. Lett.* **2010**, *105*, 127601.

[7] R. Maranganti, and P. Sharma, *Phys. Rev. B* **2009**, *80*, 054109.

[8] A. K. Tagantsev, V. Meunier, P. Sharma, *MRS Bulletin* **2009**, *34*, 643.

[9] A. Gruverman, B. J. Rodriguez, A. I. Kingon, R. J. Nemanich, A. K. Tagantsev, J. S. Cross, and M. Tsukada, *Appl. Phys. Lett.* **2003**, *8*3, 728.

[10] W. Ma, L. E. Cross, *Appl. Phys. Lett.* **2005**, *86*, 072905.

[11] W. Ma , L. E. Cross , *Appl. Phys. Lett.* **2006**, *88*, 232902.

[12] L. E. Cross, *J. Mater. Sci.* **2006**, *41*, 53.

[13] P. Zubko, G. Catalan, A. Buckley, P. R. L. Welche, J. F. Scott, *Phys. Rev. Lett.* **2007**, *99*, 167601 .

[14] D. Lee, T. W. Noh, *Philos. Transact. A. Math. Phys. Eng. Sci.* **2012**, *370*, 4944.

[15] D. Lee, A. Yoon, S. Y. Jang, J.-G. Yoon, J.-S. Chung, M. Kim, J. F. Scott, and T. W. Noh, *Phys. Rev. Lett.* **2011**, *107*, 057602.

[16] G. Catalan, L. J. Sinnamon, J. M. Gregg, *J. Phys.: Condens. Matter* **2004**, *16*, 2253.

[17] G. Catalan, B. Noheda, J. McAneney, L. J. Sinnamon, J. M. Gregg, *Phys. Rev. B* **2005**, *72*, 020102(R).

[18] G. Catalan, A. Lubk, A. H. G. Vlooswijk, E. Snoeck, C. Magen, A. Janssens, G. Rispens, G. Rijnders, D. H. A. Blank, and B. Noheda, *Nature Mater.* **2011**, *16*, 963.

[19] H. Lu, C.-W. Bark, D. Esque de los Ojos, J. Alcala, C. B. Eom, G. Catalan, A. Gruverman, *Science* **2012**, *336*, 59.

[20] D. Lee, S. M. Yang, J.-G. Yoon , and T. W. Noh, *Nano Lett*. **2012** *12*, 6436.

[21] Y. H. Chu, Q. Zhan, L. W. Martin, M. P. Cruz, P. L. Yang, G. W. Pabst, F. Zavaliche, S. Y. Yang, J. X. Zhang, L. Q. Chen, D. G. Schlom, I. N. Lin, T. B. Wu, and R. Ramesh, *Adv. Mater*. **2006**, *18*, 2307.

[22] S. H. Baek, H.W. Jang, C. M. Folkman, Y. L. Li, B.Winchester, J. X. Zhang, Q. He, Y. H. Chu, C. T. Nelson, M. S. Rzchowski, X. Q. Pan, R. Ramesh, L. Q. Chen, and C. B. Eom, *Nature Mater*. **2010**, *9*, 309.

[23] Y. H. Chu, M. P. Cruz, C. H. Yang, L. W. Martin, P. L. Yang, J. X. Zhang, K. Lee, L. Q. Chen, and R. Ramesh, *Adv. Mater*. **2007**, *19*, 2662.

[24] S. Y. Yang, J. Seidel, S. J. Byrnes, P. Shafer, C.-H. Yang, M. D. Rossell, P. Yu, Y.-H. Chu, J. F. Scott, J. W. Ager, III, L. W. Martin, and R. Ramesh, *Nature Nanotech*. **2010**, *5*, 143.

[25] S. M.Wu, Shane A. Cybart, P. Yu, M. D. Rossell, J. X. Zhang, R. Ramesh, and R. C. Dynes, *Nature Mater*. **2010**, *9*, 756.

[26] J. Seidel, L.W. Martin, Q. He, Q. Zhan, Y.-H. Chu, A. Rother, M. E. Hawkridge, P. Maksymovych, P. Yu, M. Gajek, N. Balke, S. V. Kalinin, S. Gemming, F.Wang, G. Catalan, J. F. Scott, N. A. Spaldin, J. Orenstein, and R. Ramesh, *Nature Mater*. **2009**, *8*, 229.

[27] S. Y. Yang, L. W. Martin, S. J. Byrnes, T. E. Conry, S. R. Basu, D. Paran, L. Reichertz, J. Ihlefeld, C. Adamo, A. Melville, Y.-H. Chu, C.-H. Yang, J. L. Musfeldt, D. G. Schlom, J. W. Ager, and R. Ramesh, *Appl. Phys. Lett.* **2009**, *95*, 062909.

[28] D. Lee, S. M. Yang, T. H. Kim, B. C. Jeon, Y. S. Kim, J.-G. Yoon, H. N. Lee, S. H. Baek, C. B. Eom, and T. W. Noh, *Adv. Mater.* **2012**, *24*, 402.

[29] D. Lee, B. C. Jeon, S. H. Baek, S. M. Yang, Y. J. Shin, T. H. Kim, Y. S. Kim, J.-G. Yoon , C. B. Eom, and T. W. Noh, *Adv. Mater.* **2012,** *24*, 6490.

[30] J. Wang, J. B. Neaton, H. Zheng, V. Nagarajan, S. B. Ogale, B. Liu, D. Viehland, V. Vaithyanathan, D. G. Schlom, U. V. Waghmare, N. A. Spaldin, K. M. Rabe, M. Wuttig, and R. Ramesh, *Science*, **2003**, *299*, 1719.

[31] F. Zavaliche,a P. Shafer, and R. Ramesh M. P. Cruz R. R. Das, D. M. Kim, and C. B. Eom, *Appl. Phys. Lett.* **2005**, *87*, 252902.

[32] H. W. Jang, D. Ortiz, S. H. Baek, C. M. Folkman, R. R. Das, P. Shafer, Y. Chen, C. T. Nelson, X. Pan, R. Ramesh, and C. B. Eom, *Adv. Mater.* **2009**, *21*, 817.

[33] P. Yu, W. Luo, D. Yi, J. X. Zhang, M. D. Rossell, C.-H. Yang, L. You, G. Singh-Bhalla, S. Y. Yang, Q. He, Q. M. Ramasse, R. Erni, L. W. Martin, Y. H. Chu, S. T. Pantelides, S. J. Pennycook, and R. Ramesh, Proc. Natl. Acad. Sci. USA **2012**, 109, 9710.

[34] V. P. Afanasjev, A. A. Petrov, I. P. Pronin, E. A. Tarakanov, E. J. Kaptelov, and J. Graul, *J. Phys.: Condens. Matter* **2001**, *13*, 8755.

[35] A. L. Kholkin, K. G. Brooks, D. V. Taylor, S. Hiboux, N. Setter, *Integrated Ferroelectrics* **1998**, *22*, 525.

[36] M. D. Glinchuk, and A. N. Morozovska, *Ferroelectrics* **2005**, *317*, 125

[37] N. Balke, I. Bdikin, S. V. Kalinin, and A. L. Kholkin, *J. Am. Ceram. Soc.* **2009**, *92*, 1629.

[38] T. H. Kim, S. H. Baek, S. Y. Jang, S. M. Yang, S. H. Chang, T. K. Song, J.-G. Yoon, C. B. Eom, J.-S. Chung, and T. W. Noh, *Appl. Phys. Lett.* **2011**, *98*, 022904.

[39] G. K. Williamson, and W. H. Hall, *Acta Metall*. **1953**, *1*, 22.

[40] J. I. Langford, D Louër, *Rep. Prog. Phys.* **1996**, *59*, 131.

[41] Ma, W. *Phys. Status Solidi B* **2008**, *245*, 761.

[42] D. Lee, S. H. Baek, T. H. Kim, J.-G. Yoon, C. M. Folkman, C. B. Eom, and T. W. Noh, *Phys. Rev. B* **2011**, *84*, 125305.

[43] C. M. Folkman, S. H. Baek, C. T. Nelson, H. W. Jang, T. Tybell, X. Q. Pan, C. B. Eom, *Appl. Phys. Lett.* **2010**, *96*, 052903.

Chapter 5
Flexoelectric control of defect formation and electronic functions in ferroelectric thin films

5.1 Introduction

The advancement of materials science relies on our ability to modify and optimize a wide range of functional properties. These properties, including electronic, magnetic and optical properties, strongly depend on the type and concentration of defects, which exist in every material. Particularly in ferroelectrics, defects play an important role in the control and optimization of these materials [1,2]. Typical ferroelectric materials contain a diversity of point defects and extended defects, which sometimes seem unavoidable even in the well-controlled fabrication conditions. These defects are usually detrimental to a functional ferroelectric property [1], but can enable some desirable functions, such as giant electromechanical response [3] and multilevel data storage [4]. This makes it necessary to fully understand the mechanism of defect formation, which can provide a relevant way for tailoring defects and their effect. While our understanding still continues

to evolve, the exact mechanism of defect formation remains unclear, with many important factors unresolved.

The interaction between polarization and charged point defects is one of the well-known mechanisms for determining the type and concentration of defects in ferroelectrics [3–7]. For example, it has been widely accepted that ferroelectric polarization drives charged point defects (e.g., vacancies) to migrate towards the energetically preferred sites, facilitating the formation of some defect compexes during fabrication process. However, it has been overlooked that such polarization-mediated defect formation can be more promoted by other intrinsic polarizations, which have a different origin from the ferroelecctric polarization. Recent studies reported that in epitaxial thin films, a huge internal electric field (E_{int}) can emerge intrinsically by various sources, such as interfacial charge discontinuity [8,9] and strain gradient [10,11], generating a consierable magnitude of polarization. Its magnitude can be around $E_{int} = 10^6$ V m^{-1} on the average and even as large as 10^7–10^8 V m^{-1} locally, which can induce the polarization of 1–10 μC cm^{-2} and seems large enough to affect the defect formation at high temperatures. Therefore, although overlooked so far, it would be critical to explore how such E_{int} and induced polarization influence the defect formation in thin films.

Particularly, flexoelectricity (i.e., generation of E_{int} by strain gradient) has recently gained much attention [10–16]. The strain gradient naturally breaks the inversion symmetry and thus can induce an electric response and intriguing phenomena in all dielectric materials. Especially for epitaxial thin films, in which the lattice mismatch can give rise to very steep elastic strain relaxation, the strain gradient becomes huge and the

associated flexoelectric field can be as large as $\geq 10^7$ V m^{-1}. This flexoelectric field has played an important role in novel electronic functions, such as domain control [10], flexoelectric rotation of polarization [11], mechanical writing of polarization [17] and flexoelectric diode [18]. Despite such universal, strong nature of flexoelectricity, however, its possible inflence on the defect formation during thin-film epitaxy has received little consideration. The exploitation of such an effect would allow the design of defect configuration and associated electronic functions, as well as provide a pathway to unravelling the fundamental physics of defect formation.

Here, we demonstrate the intriguing effect of E_{int} on defect formation in ferroelectric $BiFeO_3$ thin films. We show that flexoelectric effect can systematically control the E_{int} and associated defect formation, emphasizing the key role of flexoelectricity in defect engineering. Finally, the flexoelectric control of defect formation allows a nearly defect-free film with fully functional electronic properties. For our study, we used a high-quality $BiFeO_3$ epitaxial thin film, grown on vicinal $SrTiO_3$ (001) substrate with a conductive $SrRuO_3$ buffer layer. Recent works demonstrated the possibility of a large E_{int} in $BiFeO_3$ films [9,19]. Also, it has been shown that the defect effects in $BiFeO_3$ films can be clearly visualized by measuring their functional properties [4,5]. Therefore, this material system offers a great opportunity to investigate the effect of E_{int} on defect formation.

5.2 Results

5.2.1 Experiments

5.2.1.1 Thin films fabrication

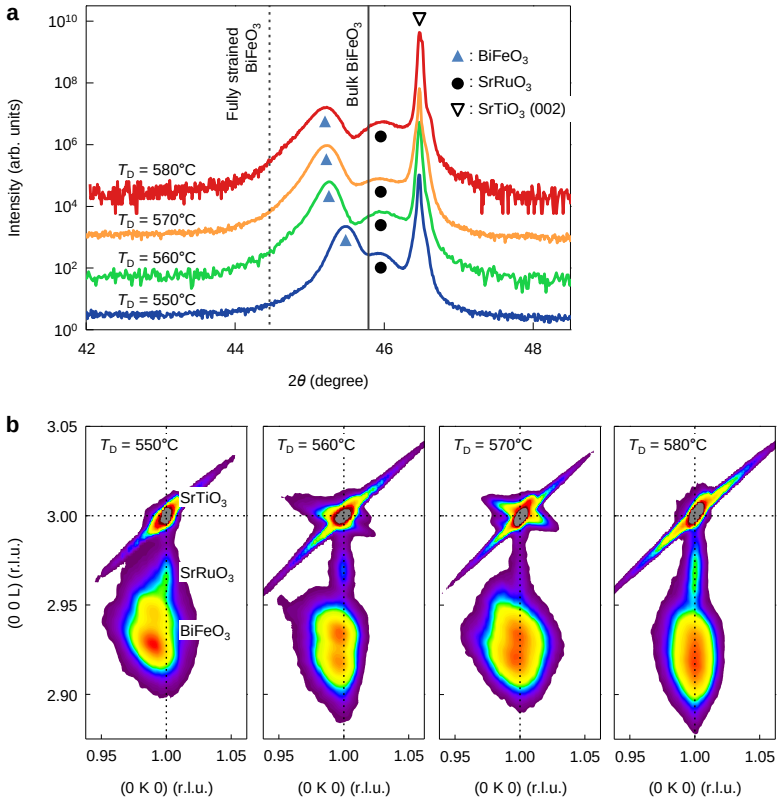

Figure 5.1 Structural analysis. (a) XRD θ–2θ scans of 250-nm-thick $BiFeO_3$ films grown at T_D = 550, 560, 570 and 580°C on vicinal $SrTiO_3$ (001) substrates. The gray short-dashed and solid vertical lines indicate the (002) diffraction peak positions of the fully strained and relaxed $BiFeO_3$ films on $SrTiO_3$ substrates, respectively. (b) RSM images around the (013) $SrTiO_3$ Bragg peaks for 250-nm-thick $BiFeO_3$ films grown at T_D = 550, 560, 570 and 580°C.

We used high-quality $BiFeO_3$ epitaxial thin films with 250-nm-thickness. The films

were sandwiched between a Pt top electrode and a single crystal $SrRuO_3$ bottom electrode. $BiFeO_3$/ $SrRuO_3$ thin-film layers were fabricated using pulsed laser deposition (PLD) onto $SrTiO_3$ (001) single-crystal substrates, with a 4° miscut toward the [100] direction. To form the bottom electrode, an $SrRuO_3$ layer (20-nm-thick) was deposited onto an $SrTiO_3$ substrate by PLD at 650℃. An oxygen pressure of 100 mTorr was maintained. The laser fluence and repetition rate were 2 J cm^{-2} and 2 Hz, respectively. The $BiFeO_3$ thin film was grown on top of the $SrRuO_3$ bottom electrode by PLD over a temperature range of 550 to 570℃. A stoichiometric $BiFeO_3$ ceramic target was used. The deposited $BiFeO_3$ film was postannealed in situ inside the PLD chamber at the deposition temperature for 1 hour under an oxygen atmosphere of 760 Torr. For the top electrode, a Pt layer (40-nm-thick) was deposited at room temperature by sputter deposition. After the deposition, the Pt layer was photolithographically patterned to form the $BiFeO_3$ capacitors. Pt top electrodes consisted of 10 to 200-μm square patterns.

5.2.1.2 Structural analysis

In order to check the crystallography and estimate the strain and its relaxation of $BiFeO_3$ epitaxial thin films, we used a high-resolution X-ray diffraction (XRD). Figure 5.1a shows XRD θ–2θ scans for 250-nm-thick $BiFeO_3$ films grown at four different deposition temperatures, i.e., T_D = 550, 560, 570 and 580℃. For these films, only the (00*l*) pseudocubic reflections could be seen along with the substrate peaks, indicating the formation of a single-crystalline $BiFeO_3$ phase with the well-oriented crystalline axes. If a $BiFeO_3$ film is fully strained under compression by a $SrTiO_3$ substrate, the in-plane lattice

constant of the film should be the same as that of $SrTiO_3$ and the *c*-axis lattice should be elongated, due to the Poisson relation where the total volume is conserved. Using this relationship, we estimated that the (002) peak for the fully strained $BiFeO_3$ should be located at $2\theta = 44.45°$, marked by the black-dashed vertical line. On the other hand, if the film becomes fully relaxed, then the (002) peak should be located at the 2θ position of bulk $BiFeO_3$, i.e., $2\theta = 45.79°$, marked by the black-solid vertical line. Figure 5.1a shows that the out-of-plane strain (along the [001] direction) became more relaxed with the T_D lowered.

To obtain information about the in-plane strain state, we used a reciprocal space mapping (RSM) analysis for 250-nm-thick $BiFeO_3$ films. Figure 5.1b shows the RSM results around the (013) $SrTiO_3$ Bragg peak for several different T_D. The (013) $BiFeO_3$ Bragg peak for $T_D = 580℃$ is located on the vertically dotted line, indicating that the film is fully strained along the [010] direction. On the other hand, the (013) $BiFeO_3$ peak for $T_D = 550℃$ is located on the left side of the vertical dotted line, indicating that the film is relaxed along the [010] direction. These RSM data show that the in-plane strain (along the [010] direction) became more relaxed with the T_D lowered, similarly as the out-of-plane strain. Thus, our XRD θ–2θ and RSM data implies that even the small variation of T_D can systematically modify the strain gradient in the films.

5.2.1.3 Electrical measurements

We investigated the ferroelectric properties of $BiFeO_3$ films using a T-F analyzer 2000 (AixACCT) at room temperature. We measured polarization–electric field (*P*–*E*)

hysteresis loops at 2 kHz. We measured current density–electric field (*J*–*E*) curves at room temperature in the dark, using a low-noise probe station and a picoampere meter (Keithley 236). Before the *J*–*E* curve measurements, a +12 V (−12 V) external-poling voltage was applied to $BiFeO_3$ capacitors to obtain the downward (upward) polarization state.

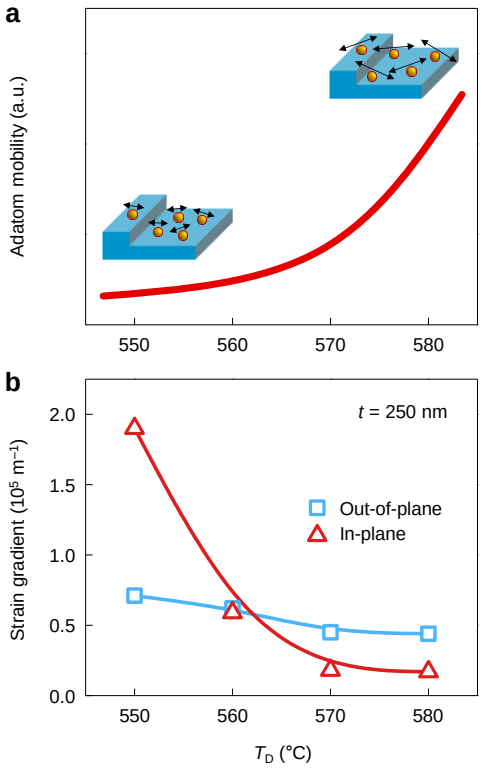

Figure 5.2 Large, systematic variation of strain gradient, according to T_D. (a) Expected surface mobility of adatoms at the T_D range of 550 to 580°C. The inset schematically depicts the mobility of adatoms at each T_D. (b) The measured strain gradients in 250-nm-thick $BiFeO_3$ films for different T_D. These values, estimated at

room temperature, are believed to remain almost unchanged at high temperatures (during film-growth process), due to similar thermal lattice expansion of perovskite materials. Solid lines are the guide to eyes.

5.2.2 Large dependence of strain gradient on T_D

To explain how the strain and its relaxation in $BiFeO_3$ films depend on the T_D variation, we consider the surface mobility of adatoms during film growth. It is natural that the surface mobility of adatoms can be enhanced with the T_D increased (Fig. 2a), which is schematically depicted in the inset. Generally, the coherent thin-film growth depends on the mobility of adatoms [20]: a higher mobility of adatoms can lead to better coherent growth and more strained state. Specifically, we found that the lateral-growth behaviour of $BiFeO_3$, related to the adatom mobility, was changed according to T_D (Fig. 5.3), which can influence the strain profile in the films. Thus, we expect that despite the slight T_D variation (i.e., from 550 to 580℃), there can be a considerable change in a strain gradient, as well as an average strain of the films.

In order to confirm this expectation, we estimated the strain gradient of 250-nm-thick $BiFeO_3$ films, using Williamson-Hall (W-H) plot [13,21,22]. First, to obtain the out-of-plane inhomogeneous strain (ε_I), four Bragg peaks–(001), (002), (003) and (004)–were selected from the XRD θ–2θ data. Then, ε_I was extracted from the following fit equation:

$$\beta \cos \theta = \frac{K\lambda_w}{D} + 4\varepsilon_I \sin \theta \quad (1)$$

where $\beta = \beta_{\text{measured}} - \beta_{\text{instrument}}$, β_{measured} is the measured line width of the diffraction peaks of the samples, $\beta_{\text{instrument}}$ is estimated from the peak width $\beta_{\text{substrate}}$ of a nearby substrate peak, λ_w = 1.5406 Å is the X-ray wavelength, D is the coherence length along the scattering vector, and K is a geometrical constant that was taken as 1. From the extracted out-of-plane ε_I values, we estimated the out-of-plane strain gradients as 0.71 × 10^5, 0.62 × 10^5, 0.45 × 10^5 and 0.44 × 10^5 m^{-1}, for $BiFeO_3$ films grown at T_D = 550, 560, 570 and 580℃, respectively (Fig. 2b) [19].

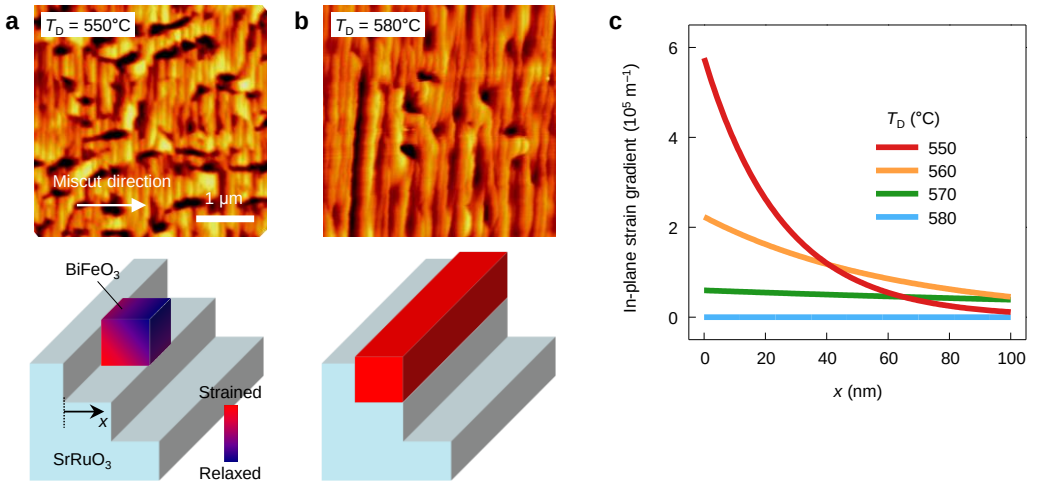

Figure 5.3 Large dependence of strain gradient on T_D. (a,b) Upper panels show atomic force microscopy images of 250-nm-thick $BiFeO_3$ films for (a) T_D = 550°C and (b) 580°C. The film surface for T_D = 580°C has a typical morphology of the step-flow growth mode. On the other hand, for T_D = 550°C, the lateral length of $BiFeO_3$ grains became much shorter, possibly due to the limited mobility of adatoms at lower T_D. Lower panels schematically describe the expected strain profile for (a) T_D

= 550°C and (b) 580°C. Considering the relationship bewteen the grain shape (e.g., aspect ratio) and strain relaxation, we can expect a larger strain gradient for lower T_D. (c) Rough estimation of in-plane strain gradient. According to a general model for the strain profile [23,24], independent of the actual relaxation mechanism, the in-plane strain ε can be expressed as follows:

$$\varepsilon(x) = \varepsilon_0 \cdot e^{-x/\delta} \quad (2)$$

where ε_0 and δ are constants, and x is the distance from the step edge. Typically, a film can be fully strained near the step edge (i.e., x = 0), due to a strong clamping effect. Also, we know the average in-plane strain values from the RSM results. Thus, using these information and Eq. (2), we can roughly estimate the profile of in-plane strain gradient. We here assumed the width of step terraces as 100 nm. The estimated values were found to be quite comparable with those obtained by W-H plots (Fig. 2b).

Similarly, to obtain the in-plane ε_I, we used the line width in the *k*-direction of the RSM peaks–(013), (023) and (033)–of $BiFeO_3$ and $SrTiO_3$ for $BiFeO_3$ films [19]. From the W-H plots for the width of those peaks, the in-plane ε_I was calculated. Using these in-plane ε_I values, we determined the in-plane strain gradients as 1.90×10^5, 0.59×10^5 m^{-1}, 0.18×10^5 and 0.17×10^5 m^{-1}, for $BiFeO_3$ films grown at T_D = 550, 560, 570 and 580℃, respectively (Fig. 5.2b). These values are quite comparable with those obtained by following a general model for the strain relaxation (Fig. 5.3). Thus, our results evidently confirm the feasibility of a systematic, large variation of strain gradient, by the precise

control of T_D.

5.2.3 Functional properties of $BiFeO_3$ films according to T_D

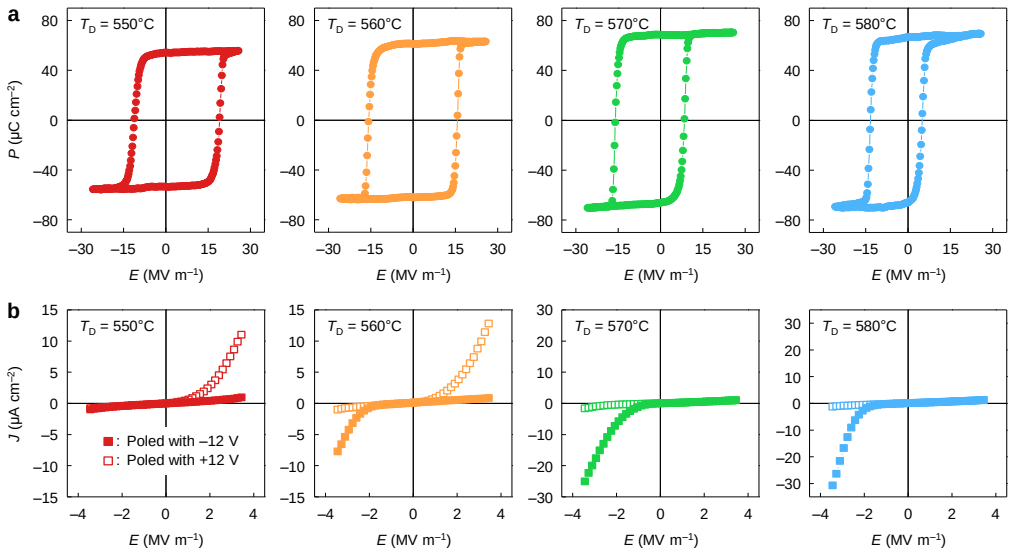

Figure 5.4 Electronic functions of $BiFeO_3$ films, according to T_D. (a) *P–E* hysteresis loops for 250-nm-thick $BiFeO_3$ films deposited at four different T_D of 550, 560, 570 and 580°C. (b) *J–E* curves measured for 250-nm-thick $BiFeO_3$ films deposited at four different T_D.

Such tunability of strain gradient may lead to drastic change in defect configurations and functional properties of the films. We explored this possibility by measuring polarization–electric field (*P–E*) loops of $BiFeO_3$ films deposited at different T_D (Fig. 5.4a). As demonstrated in our previous work (ref. 4; Fig. 5.5), defect dipoles (D_{defect}) can mainly cause the shift of *P–E* loops, called the imprint, in $BiFeO_3$ and other ferroelectric

films [4,25,26], whose amount depends on the D_{defect} concentration. Figure 5.4a shows that every film exhibits a good *P*–*E* hysteresis loop with a nearly rectangular shape, indicating no polarization relaxation. On the other hand, the shift of *P*–*E* loop exhibits a strong dependence on T_D: the film deposited at T_D = 560℃ shows almost no shift in *P*–*E* loops, while those deposited at T_D = 550, 570 and 580℃ show an apparent shift. Thus, we can expect that the relatively large amount of D_{defect} is accompanied with $BiFeO_3$ films for T_D = 550, 570 and 580℃, while the nearly D_{defect}-free film is achievable for T_D = 560℃.

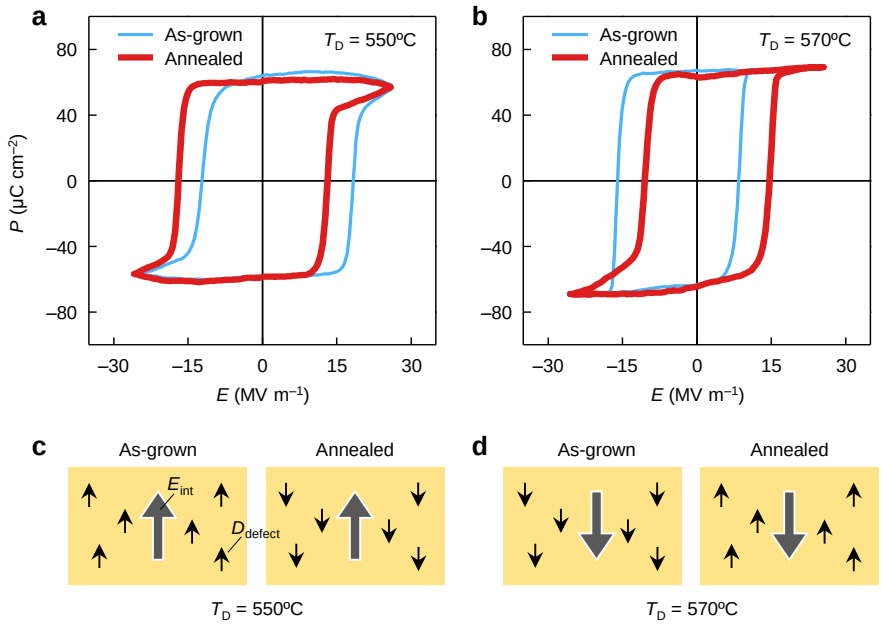

e

T_D (ºC)	E_{dd} (MV m^{-1})	E_{int} (MV m^{-1})	E_{if} (MV m^{-1})	E_{flexo} (MV m^{-1})
550	+2.6	+0.64	–3.2	+3.8
570	–3.0	–0.75	–3.2	+2.4

Figure 5.5 The shift of *P–E* loops. (a,b) *P–E* hysteresis loops of 250-nm-thick $BiFeO_3$ films for (a) T_D = 550°C and (b) 570°C. We recently demonstrated that the shift of *P–E* loops is mainly due to the pinning field (E_{dd}) by defect dipoles (D_{defect}) [27]. We also found that the D_{defect} alignmnent (and associated E_{dd} direction) can be reversed by the polarization switching and subsequent annealing, which modifies the *P–E* hysteresis loops (i.e., the direction of shift). (Details of the annealing procedure are explained in ref. 27.) (c,d) Schematic illustrations describing the D_{defect} and E_{int} (= E_{if} + E_{flexo}) direction of the as-grown (left) and annealed state (right), for (c) T_D = 550°C and (d) 570°C. (e) The direction of E_{dd} (by D_{defect}) can be reversed after the annealing precedure, whereas the E_{int} direction should be nearly unchanged. This means that the shifted value (E_{shift}) of *P–E* loops can be expressed as

$$E_{shift} = \pm E_{dd} + E_{int} \text{ (+: for as-grown state, –: for annealed state)} \quad (3).$$

Thus, using the E_{shift} values (obtained from *P–E* loops), we can estimate the values of E_{dd} and E_{int}, as shown in (e). The estimated values indicate that the shift of *P–E* loops is mainly due to E_{dd} (by D_{defect}), with small contribution from E_{int}. Referring to the strain-gradient values (Fig. 5.2) for T_D = 550°C and 570°C, we also determined the values of E_{if} and E_{flexo}, which are comparable with the calculated E_{if} (ref. 28) and estimated E_{flexo} values (Fig. 5.8).

Additionally, we explored current *J–E* curves for each polarization state of $BiFeO_3$ films (Fig. 5.4b). The small values of applied *E* ensures that little polarization switching occurs during the *J–E* measurements. $BiFeO_3$ has shown rectifying diode and

photovoltaic effects, whose polarity can be switched by the polarization reversal [29]. We recently found that in $BiFeO_3$ thin films, the diode effect was governed by interfacial carrier injection, and the switching of diode polarity could be inhibited by an interfacial defective layer (presumably, oxygen vancancy (V_O)-rich layer) [5]. Similarly as in previous studies, the polarity of diode effect could not be switched in our $BiFeO_3$ films for T_D = 550, 570 and 580℃ (Fig. 5.4b), indicating the presence of V_O-rich layer at the interface. Interestingly, however, the $BiFeO_3$ film for T_D = 560℃ clearly showed the polarity-switchable diode effect, implying a relatively perfect, much less defective interface of the film.

5.2.4 Defect configurations in $BiFeO_3$ films according to T_D

Figure 5.6a summarizes the defect configurations, determined from the measurements of *P–E* loops and *J–E* curves, in $BiFeO_3$ films according to T_D. We also plot the shifted values of *P–E* loops as a function of T_D, as shown in Fig. 5.6b. Further information on the defect concentration can be obtained more easily by measuring the unit-cell volume of $BiFeO_3$ films. Since the formation of point defects usually results in the increase of unit-cell volume [30], the measurement of unit-cell volume provides a simple, but effective, way for a relative comparison of the point-defect concentrations. Figure 5.6c shows the unit-cell volume of $BiFeO_3$ films as a function of T_D, measured from a high-resolution XRD. The film for T_D = 560℃ shows the smallest unit-cell volume, which implies a fewer amount of defects, compared to those for T_D = 550, 570 and 580℃, consistenly with our expectation from *P–E* loops and *J–E* curves.

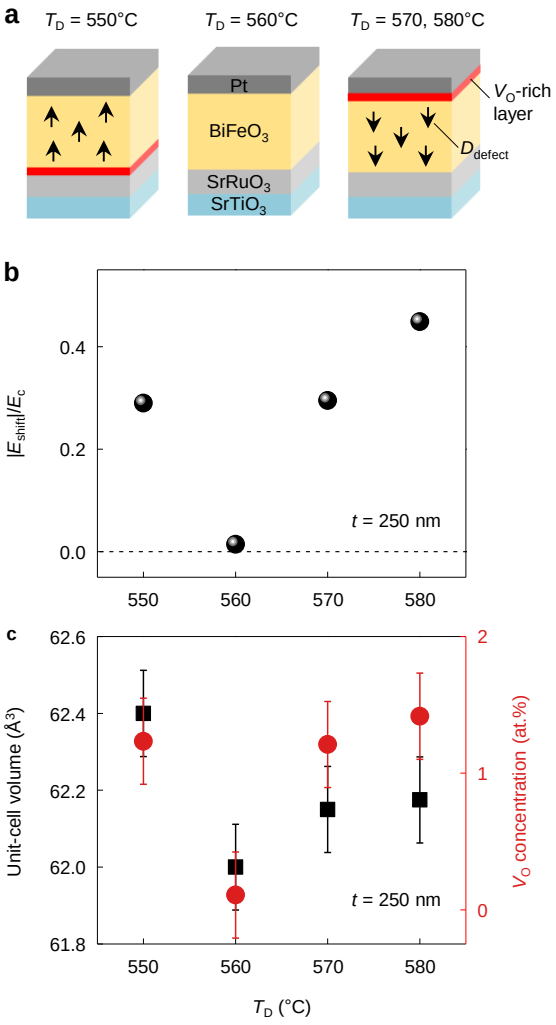

Figure 5.6 Defect configurations in $BiFeO_3$ films, according to T_D. (a) The schematic configurations of D_{defect} and V_O-rich layer in $BiFeO_3$ films according to T_D, determined from the measurements of *P*–*E* loops and *J*–*E* curves. (b) The shift in *P*–*E* loops of 250-nm-thick $BiFeO_3$ films, as a function of T_D. We normalized the shifted

values (E_{shift}) of *P*–*E* loops by the coercive field (i.e., $E_c = (E_{c,+} - E_{c,-})/2$). (c) Unit-cell volume (black closed squares) and estimated V_O concentration (red closed circles) of 250-nm-thick $BiFeO_3$ films, as a function of T_D.

Furthermore, we tried to roughly estimate the V_O concentration in the films from the measured unit-cell volume. According to the empirical model, the unit-cell volume V of perovskites can be expressed as below [31]

$$V = A^3 \cdot (r_B + r_{anion})^3 \quad (4)$$

where r_B and r_{anion} are ionic radii of B-site cation and anion, respectively, and A is a constant close to 2. By assuming oxygen-deficient $BiFeO_{3-\delta}$ for the simplicity, we can define the effective cation and anion radii as [32]

$$r_B = (1-2\delta) \cdot r_{Fe^{3+}} + (2\delta) \cdot r_{Fe^{2+}} \quad (5)$$

$$r_{anion} = (\frac{3-\delta}{3}) \cdot r_O + (\frac{\delta}{3}) \cdot r_v \quad (6)$$

where $r_{Fe^{3+}}$, $r_{Fe^{2+}}$, r_O and r_v are the ionic radii of Fe^{3+}, Fe^{2+}, oxygen and V_O, respectively. The values for these radii are all available, with the exception of those for V_O, from the work of Shannon [33]. For our study, we chose the value of r_v as 1.0 Å (ref. 32). Then, we determined the δ values (i.e., the concentration of V_O) from the measured unit-cell volume. Figure 5.6c shows that while the $BiFeO_3$ film for T_D = 560℃ is free of excessive V_O, other films for different T_D include a noticeable amount of V_O. Thus, it seems clear that the defect formation is sensitive to T_D, and even a very small deviation of T_D (from 560℃) promotes the defect formation in our $BiFeO_3$ films.

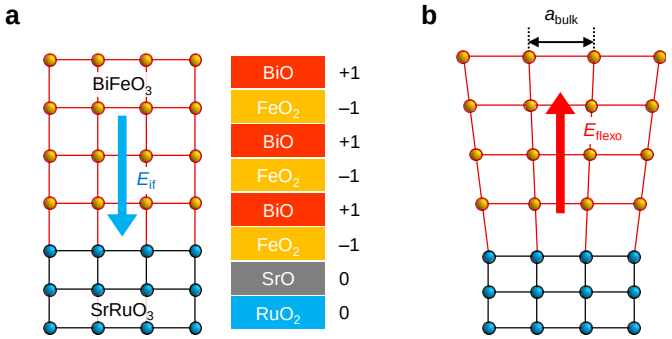

Figure 5.7 Two competing, intrinsic sources of E_{int} in $BiFeO_3$ films on $SrRuO_3/SrTiO_3$. (a) Interfacial charge discontinuity can generate the downward internal electric field (E_{if}) in $BiFeO_3$ films on $SrRuO_3/SrTiO_3$ substrate [28]. Note that $SrRuO_3$ is self-terminated with SrO surface, since the RuO_2-layer is highly volatile. (b) Relaxation of compressive misfit strain can generate the upward internal electric field (E_{flexo}) via flexoelectricity in $BiFeO_3$ films on $SrRuO_3/SrTiO_3$ substrate.

5.2.5 Large, systematic control of E_{int} via flexoelectricity.

Our results in Fig. 5.4 and 5.6 revealed a couple of interesting features on the defect formation in $BiFeO_3$ films. First, the small T_D variation (i.e., ±10℃) made a surprisingly large difference in defect concentration, and then significantly modified functional properties of $BiFeO_3$ films. Secondly, we found that only the film deposited at the intermediate T_D (= 560℃) was free of excessive defects, although it is more natural that the defect concentration is monotonically varied according to the increased (or decreased)

T_D. These results highlight that there exists an unconventional mechanism of defect formation in our $BiFeO_3$ films.

We propose that flexoelectricity can play an emerging role in defect formation via tailoring E_{int} in the films. The $BiFeO_3$ film on $SrRuO_3/SrTiO_3$ substrate has mainly two dominant sources for E_{int}: one is flexoelectric effect by strain gradient that can generate upward electric field (E_{flexo}) [19], and another is the interfacial charge discontinuity that can generate downward electric field (E_{if}; Fig. 5.7) [9]. We estimated E_{flexo} from the measured strain gradient, using the following equation [15,16]:

$$E_{flexo} = \lambda \frac{e}{\varepsilon_0 a} \frac{\partial \varepsilon}{\partial x} \quad (5)$$

where e is the electronic charge, ε_0 is the permittivity of free space, a is the lattice constant, $\partial\varepsilon/\partial x$ is the strain gradient, and λ is a flexoelectirc coefficient close to unity. Importantly, we already showed that even a small variation of T_D can greatly modify the strain gradient (Fig. 5.2). Thus, the associated E_{flexo} can vary considerably according to T_D, whereas E_{if} is expected to remain nearly unchanged, which enables a large, systematic control of E_{int} (= E_{flexo} + E_{if}).

Figure 5.8 shows that a subtle competition between E_{flexo} and E_{if} causes a drastic change in E_{int}: even for the small T_D variation from 550 to 580℃, E_{int} can have a wide range of change (from $E_{int} \geq +10^6$ V m^{-1} to $\leq -10^6$ V m^{-1} through $E_{int} \approx 0$), which may also explain our observed drastic change in defect configurations. We should note that the nearly defect-free $BiFeO_3$ film (corresponding to T_D = 560℃) was achievable in the case of a small E_{int} (i.e., $E_{int} \approx 0$), while the relatively large amount of defects in the films

(corresponding to T_D = 550, 570 and 580℃) was accompanied with a large E_{int}. Thus, it seems that a large E_{int} might promote the defect formation in $BiFeO_3$ and, in other words, a small E_{int} is essential for making a defect-free film.

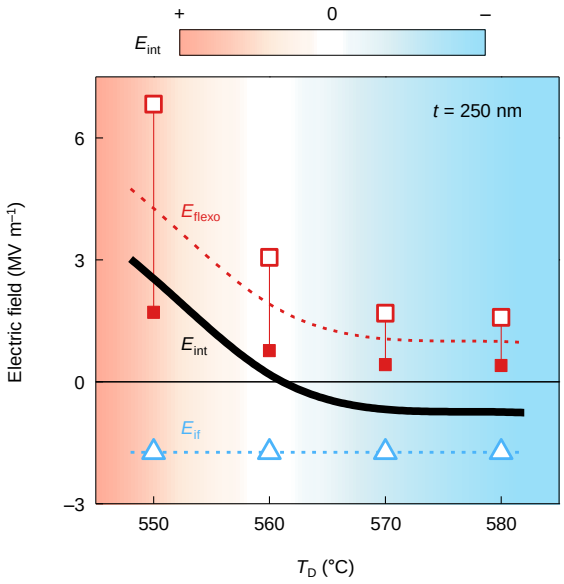

Figure 5.8 Large, systematic control of E_{int} via flexoelectricity. The estimated E_{int} for 250-nm-thick $BiFeO_3$ films, as a function of T_D. Using the measured values of strain gradient, we estimated E_{flexo}, projected onto the ferroelectric polarization direction (i.e., [111] or its equivalent ones). Red open and closed squares correspond to E_{flexo} for the flexoelectric coefficient λ = 1.0 and 0.25, respectively. Red dashed line represents the averaged values of E_{flexo} for λ = 1.0 and 0.25. Blue open triangles represent E_{if}, obtained by referring to the calculated values (ref. 9) and projecting them onto the polarization direction. Black solid line represents E_{int} (= E_{flexo} + E_{if})

according to T_D, obtained by summing E_{flexo} and E_{if}. The positive (or negative) E_{int} indicates the upward (or downward) field direction.

5.2.6 Demonstration of the E_{int} effect on defect formation.

To confirm the effect of E_{int} on defect formation, we controlled the E_{int} by varying only the film thickness, with other growth parameters fixed. We first present the case of T_D = 550℃. The fully strained 50-nm-thick $BiFeO_3$ film without any strain relaxation has no flexoelectric contribution (i.e., E_{flexo} = 0), with the contribution only from E_{if}. This causes the 50-nm-thick $BiFeO_3$ film to have a large downward E_{int}, whereas 250-nm-thick film with a substantial E_{flexo} contribution has a large upward E_{int}, as schematically shown in Fig. 5.9a. This implies that at an intermediate thickness between 50 and 250 nm, E_{flexo} and E_{if} should be balanced with each other, making E_{int} to be reduced. Due to this reduced E_{int}, according to our prediction, the films with intermediate thicknesses should have a fewer amount of defects, compared to the thinnest or thickest films. Indeed, by measuring the unit-cell volume and shift of *P–E* loops, we found that the films with intermediate thicknesses were less defective (Fig. 5.9c).

For T_D = 570℃, differently from the case of T_D = 550℃, the strain gradient cannot be large enough to reverse the E_{int} direction (Fig. 5.9b). Increasing *t* makes E_{int} to vary from a large negative value to a small negative one, just without the directional change. In this case, according to our prediction, the defect concentration in the films would decrease monotonically with the *t* increased, which is verified by measuring the unit-cell volume

and shift of *P*–*E* loops (Fig. 5.9d). Thus, these results unambiguously demonstrate the important role of E_{int} in defect formation.

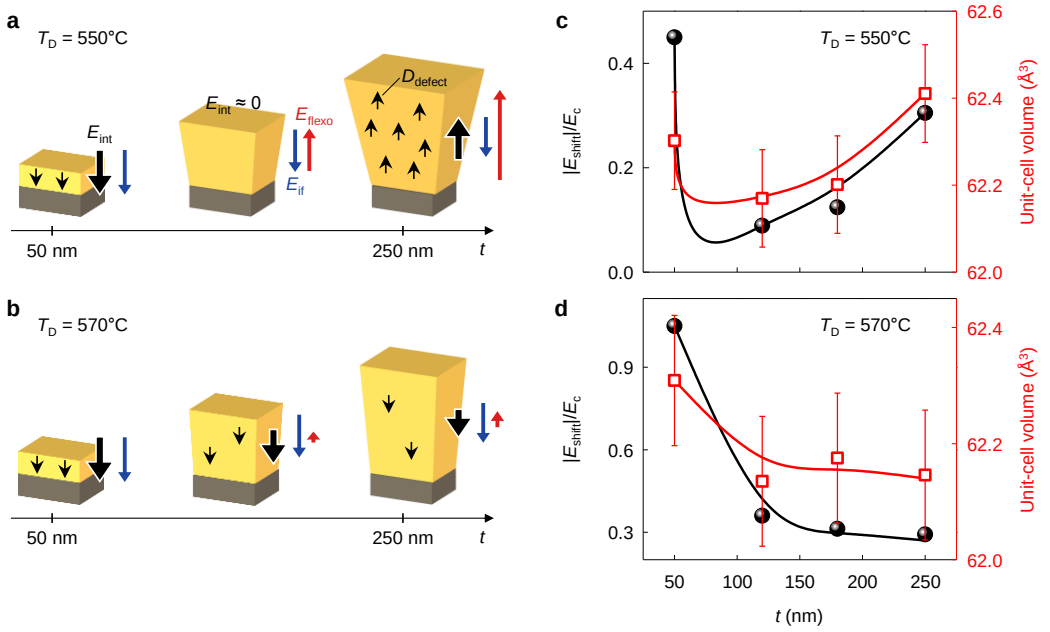

Figure 5.9 Demonstration of the E_{int} effect on defect formation. (a,b) Schematics of the E_{int} variation according to the film thickness *t*, for (a) T_D = 550 and (b) 570°C. Red, blue and black arrows represent E_{flexo}, E_{if} and E_{int}, respectively. The length of arrows indicates the magnitude of the associated electric field. (c,d) The measured shift of *P*–*E* loops (black closed circles) and unit-cell volume (red open squares) as a function of *t*, for (c) T_D = 550 and (d) 570°C. Solid lines are the guide to eyes.

5.3 Discussion

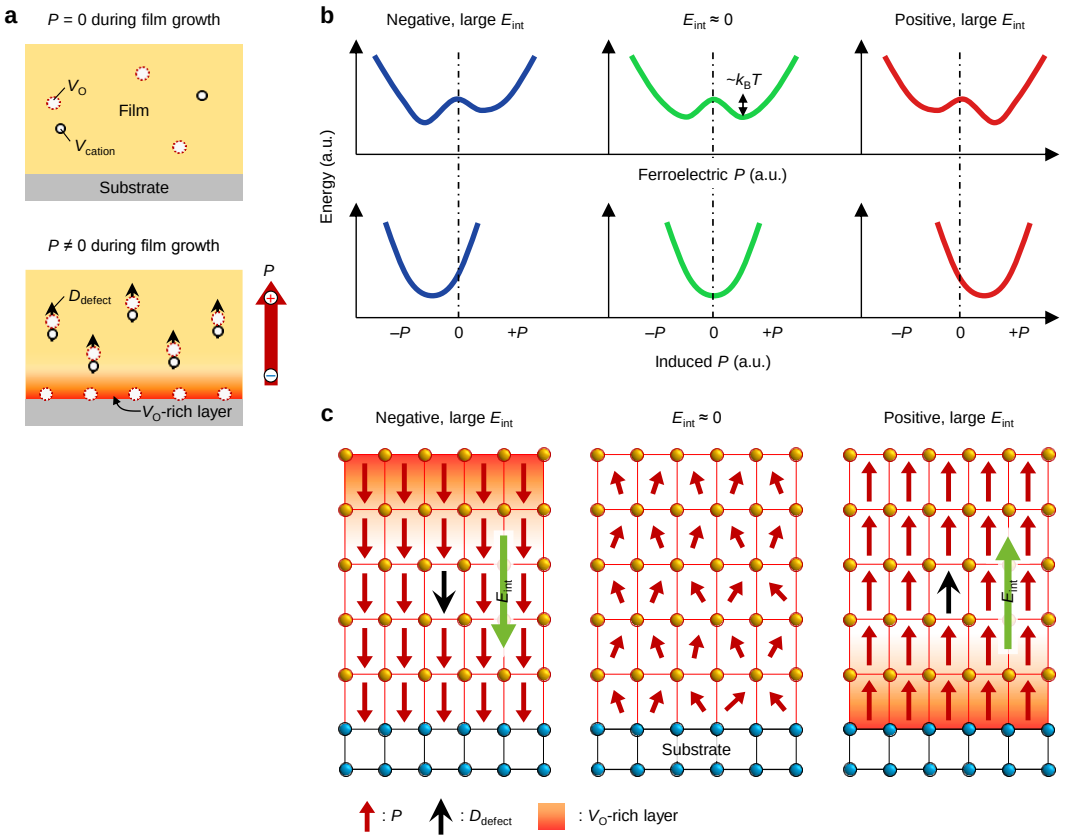

Figure 5.10 Effect of E_{int} on polarization-mediated defect formation. (a) Schematic illustration of the defect formation in ferroelectrics. Defect dipoles (D_{defect}) acquire the energy gain for their formation by the interaction with ferroelectric polarization P (ref. 27,35,36). Usually, cation vacancy (V_{cation}) or impurity forms D_{defect} together with oxygen vacancy (V_O). Also, the interfacial accumulation of positively charged V_O can have the energy gain by compensating the negative polarization charge, resulting in the formation of V_O-rich layer [37,38]. (b) Expectation of polarization profile at high temperatures during film growth, according to E_{int}. For $E_{int} \approx 0$, the interaction between charged point defects and polarization can be weakened due to

thermal fluctuation (~k_BT) of polarization, inhibiting the polarization-mediated defect formation. On the other hand, if a large E_{int} exists, it can induce a noticeable magnitude of polarization, as well as stabillize the ferroelectric polarization against thermal fluctuation. (c) The polarization-mediated defect formation can be promoted under a large E_{int}.

We can now explain how E_{int} contributes to the defect formation in $BiFeO_3$ films. It is well known that the interaction between charged point defects and polarization can give the energy gain for the defect formation [3–7]. Such energy gain drives charged point defects (e.g., vacancies) to migrate towards the energetically preferred sites at high temperatures during film growth (Supplementary Fig. 5.10a), and then facilitates the formation of the associated defects, including D_{defect} (refs. 3,4,7) and V_O-rich interfacial layer [5,6]. This process of polarization-mediated defect formation relies on the strength and stability of polarization at high temperatures during film growth [34]: the equilibrium defect concentration can increase, as the polarization becomes stronger and more stable at high temperatures, due to higher energy gain for the defect formation (in other words, lower formation energy of the defects).

We suggest that a large E_{int} discussed here can allow a stable polarization, promoting the polarization-mediated defect formation. It should be noted that the strain gradient and interfacial charge discontinuity have a robust, intrinsic nature, which cannot be easily altered by external perturbations: the strain gradient in epitaxial thin films is determined by interfacial lattice mismatch and intrinsic elastic strain relaxation, and the interfacial

charge discontinuity is determined by charge state and stacking sequence of atomic layers. As a result, the E_{int}, orginating from these robust origins, can induce a stable polarization (Supplementary Fig. 5.10b,c), differently from ferroelectric polarization that can be weakened by thermal fluctuation at high temperatures. Thus, we believe that E_{int} can promote the polarization-mediated formation of defects, such as D_{defect} and V_O-rich layer, by allowing a stable polarization during film growth.

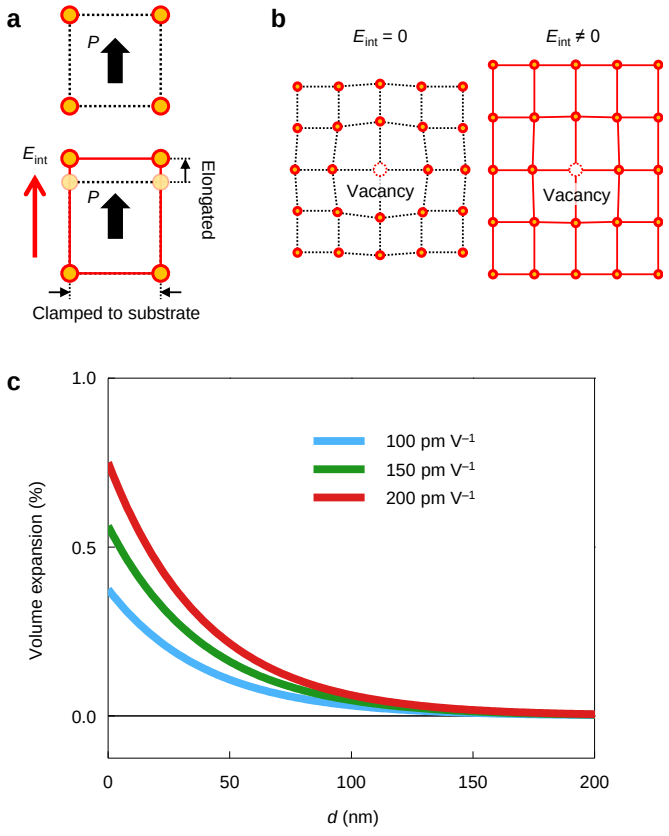

Figure 5.11 Possible effect of E_{int} on the formation of point defects. (a) A large E_{int} can cause the lattice volume expansion by piezoelectric effect in ferroelectrics. [Note

that E_{int} can also cause the crystal volume expansion (as large as ~1.0 % locally) by electrostrictive effect in polar materials, already reported in ref. 39.] (b) The formation of point defects is accompanied with the increase of unit-cell volume, requiring an energy cost (e.g., from elastic energy). If the unit-cell volume is already large, the energy cost for the defect formation can be reduced. Referring to a recent theoretical work [40], we can expect that the formation of point defects can be more promoted for the enlarged unit cell under a large E_{int}, increasing the equilibrium defect concentration in our $BiFeO_3$ films. (c) In order to quantitatively explore a possible crystal volume expansion by E_{int}, we consider the E_{flexo} contribution. The strain relaxation and associated E_{flexo} follow the exponential decay as a function of distance (d) from the bottom interface (i.e., $\propto e^{-d/\delta}$). We assumed the averaged E_{flexo} value of 5×10^6 V m^{-1} and the δ value of 40 nm. We also used three different values (d_{33} = 100, 150, and 200 pm V^{-1}) for converse piezoelectric coefficient. The d_{33} value of $BiFeO_3$ is around 50–100 pm V^{-1} at room temperature. Note that the d_{33} is roughly proportional to the dielectric permittivity and polarization (i.e., $\propto \varepsilon \cdot P$), and thus can show the increasing trend as the temperature increases and approaches to the Curie temperature. In spite of the parameter dependence, our result evidently shows that the E_{int} can lead to a lattice-volume expansion (as large as locally 0.5–1.0 %) at high temperatures during film growth.

Additionally, the E_{int} might also generally contribute to the formation of point defects in polar/ferroelectric materials, not limited to the formation of D_{defect} and V_O-rich layer.

The formation of point defects usually leads to lattice volume expansion [30]. According to a recent theoretical calculation [41], the reverse effect is also true: that is, a larger lattice volume can decrease the formation energy of point defects, thereby promoting the defect formation. We should note that E_{int} can cause the lattice volume expansion by electrostrictive [42] and/or piezoelectric effects in polar/ferroelectric materials (Fig. 5.11), which might be as large as locally ~1.0 % at high temperatures during film growth. Thus, compared to the case of $E_{int} \approx 0$, the formation of point defects might be more facilitated under a large E_{int}, increasing the equilibrium defect concentration in polar/ferroelectric films.

Our study provides novel insight into defect engineering in epitaxial thin films. It is rather surprising that the E_{int} contribution to defect formation has been overlooked, although a huge E_{int} can intrinsically exist in various thin-film systems [8–11,19] and sometimes seems inevitable. Consideration of E_{int} may explain why some thin films include many defects (e.g., vacancies and off-stoichiometry) even with the carefully optimized growth condition [43,44]. Furthermore, we suggest that flexoelectricity enables a general way to control the E_{int} and defect formation in epitaxial thin films. Flexoelectricity (and resulting E_{int}) universally exists in every strain-graded dielectric material [12–16] and has modified diverse functional properties of dielectric/ferroelectric thin films [10,11,17–19]. This universal nature of flexoelectricity makes it more essential to seriously consider a possible effect of E_{int} on the defect formation.

5.4 Conclusion

In summary, we demonstrated that flexoelectricity can emerge as a practical means to control the defect formation in thin films. We showed that the defect formation in $BiFeO_3$ films depended on the internal electric field, whose magnitude could be modified by flexoelectric effect. Finally, we could tailor the associated functional properties of $BiFeO_3$ films, as well as achieve a nearly defect-free $BiFeO_3$ film exhibiting imprint-free polarization hysteresis loop and switchable diode effect. Our findings can be used to optimize physical properties of thin films, as well as realize fully functional films, by controlling the defect formation.

References

1. Lines, M. E. & Glass, A. M. *Principles and Applications of Ferroelectrics and Related Materials* (Clarendon, Oxford, 1977).

2. Dawber, M. *et al*. Physics of thin-film ferroelectric oxides. *Rev. Mod. Phys.* **77**, 1083–1130 (2005).

3. Ren, X. B. *et al*. *Nat. Mater*. **3**, 91–94 (2004).

4. Lee, D. *et al*. *Adv. Mater*. **24**, 6490 (2012).

5. Lee, D. *et al*. *Phys. Rev. B* **84**, 125305 (2011).

6. Chisholm, M. F *et al*. *Phys. Rev. Lett.* **105**, 197602 (2010).

7. Lee, D. *et al*. *Phys. Rev. B* **81**, 012101 (2010).

8. Ohtomo, A. & Hwang, H. Y. *Nature* **427**, 423 (2004).

9. Yu, P. *et al*. *Proc. Natl. Acad. Sci.* **109**, 9710 (2012).

10. Lee, D. *et al*. *Phys. Rev. Lett.* **107**, 057602 (2011).

11. Catalan, G. *et al*. *Nat. Mater*. **10**, 963 (2011).

12. Kogan, S. M. *Sov. Phys. Solid State* **5**, 2069 (1964).

13. Catalan, G *et al*. *Phys. Rev. B* **72**, 020102(R) (2005).

14. Zubko, P. *et al*. *Phys. Rev. Lett.* **99**, 167601 (2007).

15. Zubko, P., Catalan, G. & Tagantsev, A. K. *Annu. Rev. Mater. Res.* **43**, 387 (2013).

16. Yudin, P. V. & Tagantsev, A. K. *Nanotechnology* **24**, 432001 (2013).

17. Lu, H. *et al*. *Science* **336**, 59 (2012).

18. Lee, D. *et al*. *Nano Lett.* **12**, 6436 (2012).

19. Jeon, B. C. *et al*. *Adv. Mater*. **25**, 5643 (2013).

20. Willmann, H. *et al. Thin Solid Films* **517**, 598 (2008).

21. Williamson, G. K. & Hall, W. H. *Acta Metall.* **1**, 22 (1953).

22. Langford, J. I. & Louër, D. *Rep. Prog. Phys.* **59**, 131 (1996).

23. Saito, K. *et al. Polar Oxides: Properties, Characterization, and Imaging*, Edited by Waser, R., Böttger, U. & Tiedke, S. (Wiley-VCH, Weinheim, 2005).

24. Kim, H. J. *et al. Appl. Phys. Lett.* **75**, 3195–3197 (1999).

25. Warren, W. L. *et al. Appl. Phys. Lett.* **67**, 866 (1995).

26. Folkman, C. M. *et al. Appl. Phys. Lett.* **96**, 052903 (2010).

27. Lee, D. *et al. Adv. Mater.* **24**, 6490 (2012).

28. Yu, P. *et al. Proc. Natl. Acad. Sci.* **109**, 9710 (2012).

29. Choi, T. *et al. Science* **324**, 63 (2009).

30. Adler, S. B. *J. Am. Ceram. Soc.* **84**, 2117 (2001).

31. Jiang, L. Q. *et al. J. Phys. Chem. Solids* **67**, 1531 (2006).

32. Marrocchelli, D. *et al. Adv. Funct. Mater.* **22**, 1958 (2012).

33. Shannon, R. D. *Acta Crystallogr., Sect. A* **32**, 751 (1976).

30 34. Lohkämper, R. *et al. J. Appl. Phys.* **68**, 4220 (1990).

35. Ren, X. B. *et al. Nat. Mater.* **3**, 91 (2004).

36. Lee, D. *et al. Phys. Rev. B* **81**, 012101 (2010).

37. Chisholm, M. F. *et al. Phys. Rev. Lett.* **105**, 197602 (2010).

38. Lee, D. *et al. Phys. Rev. B* **84**, 125305 (2011).

39. Cancellieri, C. *et al. Phys. Rev. Lett.* **107**, 056102 (2011).

40. Aschauer, U. *et al. Phys. Rev. B* **88**, 054111 (2013).

41. Aschauer, U. *et al*. *Phys. Rev. B* **88**, 054111 (2013).

42. Cancellieri, C. *et al. Phys. Rev. Lett.* **107**, 056102 (2011).

43. Li, Z. *et al. Adv. Funct. Mater.* **22**, 4312 (2012).

44. Warusawithana, M. P. *et al. Nat. Commun.* **4**, 2351 (2013).

Chapter 6
Conclusion

Over the last several decades, a flurry of studies on the ferroelectric materials has been performed due to the scientific interest in fundamental physics viewpoints as well as potential applications in multifunctional electronic devices. Especially, $BiFeO_3$ (BFO) is the most attractive multiferroic material, since it has at least two kinds of order parameters, ferroelectricity, ferroelasticity, and antiferromagnetism. It has shown rich and intriguing physical phenomena such as domain wall conduction, morphotropic phase boundary, and photovoltaic effect. Despite these extensive studies, I believe that many interesting issues still remain untouched. Growth of the high-quality BFO thin films is prerequisite to studies about untouched issues. In this thesis, I have successfully fabricated high-quality BFO thin film capacitors. Using these samples, I investigated the flexoelectric effect in the reversal of self-polarization and associated changes in the electronic functionalities of BFO thin films.

I controlled the formation of defects in BFO thin films by varying the substrate temperature during epitaxial growth over a narrow range of 570–600℃. We found that the presence of defects significantly affects the optical and ferroelectric properties. The BFO films grown at $T_D \leq 580$℃ had a band gap of 2.5 ± 0.2 eV and showed rectangular

P–E hysteresis loops. Fe_2O_3 impurities appeared in the BFO films grown at $T_D \geq 590$℃, leading to drastic changes in the optical response and leaky *P–E* hysteresis loops. Our work suggests that the defect evolution in BFO films critically depends on the deposition temperature.

We found that the flexoelectric effects can play an important role in determining the self-polarization direction in the BFO thin films. I could successfully control the strain evolution of the films by varying the deposition temperature and the film thickness. Then, due to flexoelectric effects, the different strain gradient states inside the BFO films could create different built-in electric fields, which resulted in changes in the self-polarization direction. In addition, the self-polarization field could also produce large variations in the imprint and diode characteristics of the as-grown BFO films by generating a defect layer and aligning the defect dipoles during the film deposition process. Thus, strain gradient engineering at the nanoscale can potentially provide exciting new opportunities to realize flexoelectricity-based devices.

Our study provides novel insight into defect engineering in epitaxial thin films. It is rather surprising that the internal electric field contribution to the defect formation has been overlooked, although a huge internal electric field can exist in various thin-film systems and sometimes seems inevitable. Consideration of internal electric field may explain why some thin films include many defects (e.g., large off-stoichiometry) even with the carefully optimized growth condition. Furthermore, we suggest that flexoelectric effect enables a general way to control the internal electric field and defect formation in epitaxial thin films. Flexoelectricity (and resulting in internal electric field, i.e., E_{flexo})

universally exists in every strain-graded dielectric material and has been modified diverse functional properties of dielectric/ferroelectric thin films. This universal nature of flexoelectricity makes it more essential to seriously consider a possible effect of internal electric field on the defect formation.

Finally, I demonstrated that flexoelectricity can emerge as a practical means to control the defect formation in thin films. I showed that the defect formation in BFO films depended on the internal electric field, whose magnitude could be modified by flexoelectric effect. I could tailor the associated functional properties of BFO films, as well as achieve a nearly defect-free BFO film exhibiting imprint-free polarization hysteresis loop and switchable diode effect. Our findings can be used to optimize physical properties of thin films, as well as realize fully functional films, by controlling the defect formation.

Appendix
Williamson-Hall plot

이 chapter에서는 XRD θ-2θ와 RSM 데이터를 통해서 박막 내부에 유도 될 수 있는 전기장의 크기를 Williamson-Hall plot (WHP)을 이용해 구하는 방법을 소개하고자 한다. 이 방법은 박막 내에 불균일한 변형(inhomogeneous strain)의 크기를 XRD 데이터를 이용해 구하는 대표적인 방법 중 하나이다.

A.1. Out-of-plane flexoelectric field를 구하는 방법

실제 BFO 박막의 결과를 예를 들어 설명하겠다. XRD 장비를 이용해 박막의 θ-2θ를 (001), (002), (003), 그리고 (004)까지 측정한다. (XRD를 측정할 수 없으면 연구단 서버에 매뉴얼이 있으니 참고하기 바람.) 이 때 (004) peak의 크기가 작으므로 여러 번 더하는 방식으로 측정한다.

그림 A.1a는 BFO 박막의 θ-2θ를 (001), (002), (003), 그리고 (004)까지 측정한 데이터이다. 각각의 BFO peak과 STO peak을 linear scale로 따로 그린다. 그림 A.1b는 BFO 박막의 θ-2θ를 (001), (002), (003), 그리고 (004)를 linear scale로 따로 그린 데이터이다. 오리진 프로그램의 식 Pearson IIV 식을 이용해 fitting을

해서 샘플 peak과 기판 peak의 β값을 구한다. 여기서 β는 full width half maximum (FWHM) 값이다. 최종적인 β값은 식 $\beta = \beta_{\mathrm{BFO}} - \beta_{\mathrm{substrate}}$ 을 이용해 구한다. 여기서 β_{BFO}와 $\beta_{\mathrm{substrate}}$는 각각 BFO 박막과 기판의 FWHM 값이다. W-H 식,

$$\beta\cos\theta = K\frac{\lambda}{D} + 4\varepsilon_{\mathrm{I}}\sin\theta\,, \qquad \text{(Eq. A1)}$$

을 이용해 각각의 peak을 찍고 linear fitting을 통해 기울기를 구한다. 이 때 기울기가 inhomogeneous strain, ε_{I}를 나타낸다. 그림 A.2는 BFO 박막의 out-of-plane WHP를 나타낸다.

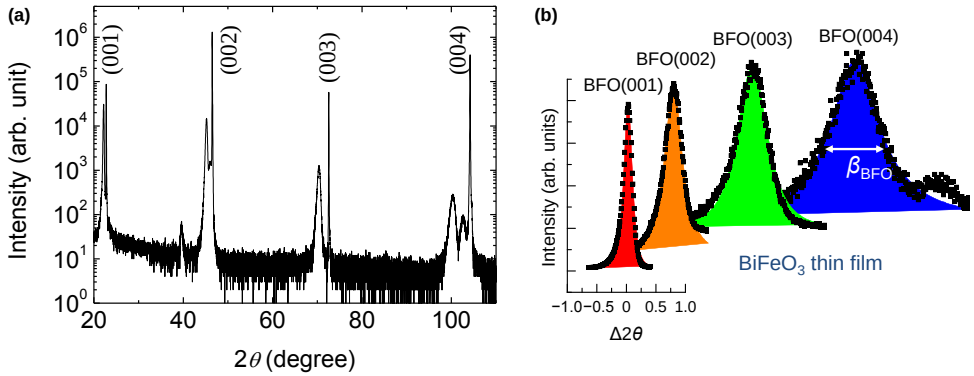

Figure A.1 (a) BFO/SRO/STO 박막의 θ-2θ를 (001), (002), (003), 그리고 (004)까지 측정한 데이터. (b) BFO 박막 peak을 Pearson VII 식을 이용한 fitting. 여기서 β_{BFO}는 BFO 박막의 FWHM 값.

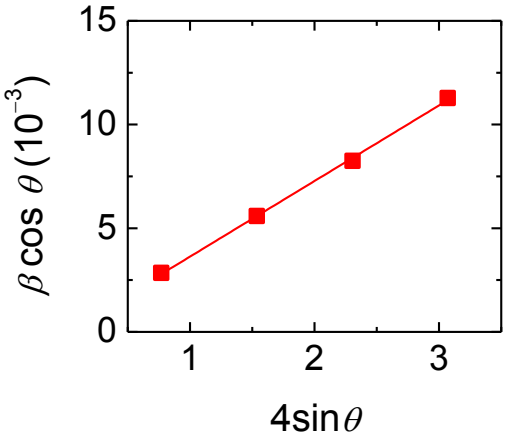

Figure A.2 Out-of-plane WHP. 기울기는 inhomogeneous strain, ε_I를 나타낸다.

그럼 다음 식,

$$\frac{t}{2\delta}\frac{\bar{\varepsilon}^2}{(\varepsilon_I^2+\bar{\varepsilon}^2)}=\tanh\left(\frac{t}{2\delta}\right), \qquad \text{(Eq. A2)}$$

을 이용해 δ를 구한다. $\bar{\varepsilon}$ 는 평균 strain 이고 t는 박막의 두께이다. δ is a measure of the penetration depth of the strain. 평균 strain과 구한 δ 값을 이용해 strain gradient를 구할 수 있다.

$$\left\langle\frac{\partial\varepsilon(z)}{\partial z}\right\rangle_{average}=-\frac{\langle\varepsilon(z)\rangle_{average}}{\delta} \qquad \text{(Eq. A3)}$$

Strain gradient를 구하면 다음 식,

$$E_{F,i}\approx\lambda\frac{e}{\varepsilon_0 a_j}\frac{\partial u_{jk}}{\partial x_i}, \qquad \text{(Eq. A3)}$$

을 이용해 flexoelectric field를 구할 수 있다. 여기서 λ is a scaling factor, e is the electronic charge, a_j is the lattice constant, and ε_0 is the permittivity of free space.

Usually, in perovskite oxide systems, λ is known to have a value on the order of 10^0 or 10^1.

A.2. In-plane flexoelectric field를 구하는 방법

XRD 장비를 이용해 박막의 RSM를 (013), (023), 그리고 (033)까지 측정한다. 그림 A.3은 BFO 박막의 (013), (023), 그리고 (033)까지 측정한 RSM 데이터이다.

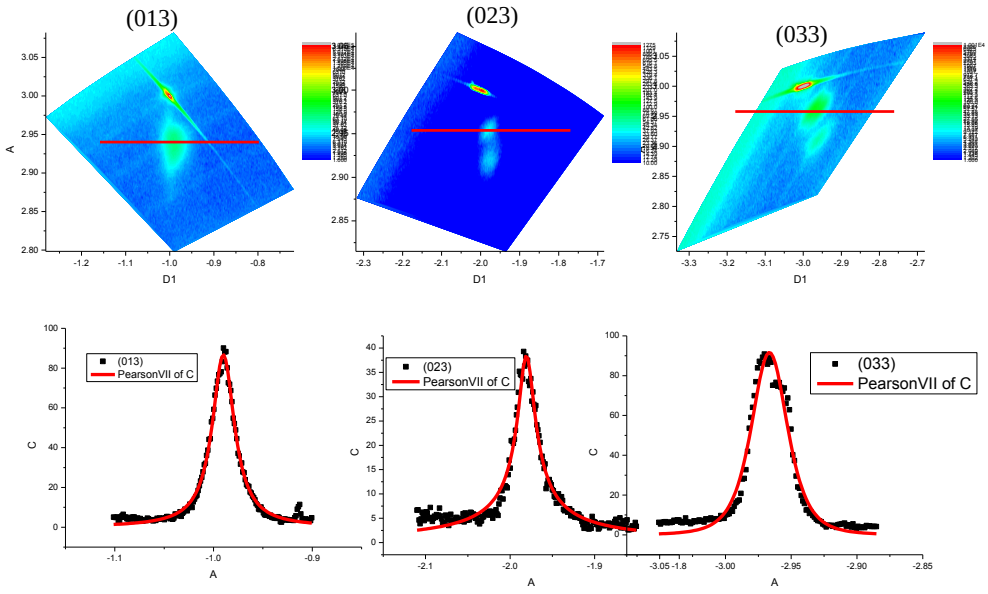

Figure A.3 BFO/SRO/STO 박막의 (013), (023), 그리고 (033)까지 측정한 RSM 데이터. I used the line width in the *k*-direction of the RSM peaks–(013), (023), and (033)–of BFO films.

RSM 데이터의 박막 peak을 k-방향으로 line profile을 딴다. 그럼 그림 A.3의 아래 쪽 데이터를 얻을 수 있다. 그 데이터를 역시 Pearson VII 식을 이용해 fitting을 한 후 위에서 언급한 “A.1. Out-of-plane flexoelectric field를 구하는 방법” 과 동일한 방법으로 in-plane flexoelectric field를 구하면 된다.

Publication List

1. Impact of vacancy clusters on characteristic resistance change of nonstoichiometric strontium titanate nano-film, Yong Su Kim, Jiyeon Kim, Moon Jee Yoon, Chang Hee Sohn, Shin Buhm Lee, Daesu Lee, **Byung Chul Jeon**, Hyang Keun Yoo, Tae Won Noh, Aaron Bostwick, Eli Rotenberg, Jaejun Yu, Sang Don Bu, and Bongjin Simon Mun, Applied Physics Letters **104**, 013501 (2014).
2. Flexoelectric Effect in the Reversal of Self-Polarization and Associated Changes in the Electronic Functional Properties of $BiFeO_3$ Thin Films, **B. C. Jeon**, D. Lee, M. H. Lee, S. M. Yang, S. C. Chae, T. K. Song, S. D. Bu, J.-S. Chung, J.-G. Yoon, and T. W. Noh, Advanced Materials **25**, 5643 (2013).
3. Neutron scattering study of magnetic excitations in a 5*d*-based double-perovskite Ba_2FeReO_6 K. W. Plumb, A. M. Cook, J. P. Clancy, A. I. Kolesnikov, **B. C. Jeon**, T. W. Noh, A. Paramekanti, and Young-June Kim, Physical Review B **87**, 184412 (2013).
4. Continuous Control of Charge Transport in Bi-Deficient $BiFeO_3$ Films Through Local Ferroelectric Switching, T. H. Kim, **B. C. Jeon**, T. Min, S. M. Yang, D. Lee, Y. S. Kim, S.-H. Baek, W. Saenrang, C.-B. Eom, T. K. Song, J.-G. Yoon, and T. W. Noh, Advanced Functional Materials **22**, 4962 (2012).
5. Active Control of Ferroelectric Switching Using Defect-Dipole Engineering D. Lee, **B. C. Jeon**, S.-H. Baek, S. M. Yang, Y. J. Shin, T. H. Kim, Y. S. Kim, J.-G. Yoon, C.-B. Eom, and T. W. Noh, Advanced Materials **24**, 6490 (2012).
6. Multilevel Data Storage Memory Using Deterministic Polarization Control D. Lee, S. M. Yang, T. H. Kim, **B. C. Jeon**, Y. S. Kim, J.-G. Yoon, H. N. Lee, S. H. Baek, C. B. Eom, and T. W. Noh, Advanced Materials **24**, 402 (2012).

7. Spin-orbit coupling in iridium-based 5*d* compounds probed by x-ray absorption spectroscopy, J. P. Clancy, N. Chen, C. Y. Kim, W. F. Chen, K. W. Plumb, **B. C. Jeon**, T. W. Noh, and Y.-J. Kim, Phys. Rev. B **86**, 195131 (2012).
8. Polarity-dependent kinetics of ferroelectric switching in epitaxial $BiFeO_3$(111) capacitors, T. H. Kim, S. H. Baek, S. M. Yang, Y. S. Kim, **B. C. Jeon**, D. Lee, J.-S. Chung, C. B. Eom, J.-G. Yoon, and T. W. Noh, Appl. Phys. Lett. **99**, 012905 (2011).
9. Electronic structure of double perovskite A_2FeReO_6 (A = Ba and Ca): interplay between spin-orbit interaction, electron correlation, and lattice distortion, **B. C. Jeon**, Choong H. Kim, S. J. Moon, W. S. Choi, H. Jeong, Y. S. Lee, J. Yu, C. J. Won, J. H. Jung, N. Hur, and T. W. Noh, Journal of Physics: Condensed Matter **22**, 345602 (2010).
10. PLD Growth of Epitaxially-stabilized 5*d* Perovskite $SrIrO_3$ Thin Films, S. Y. Jang, S. J. Moon, **B. C. Jeon**, and J.-S. Chung, Journal of the Korean Physical Society **56**, 1814 (2010).
11. The electronic structure of epitaxially stabilized 5*d* perovskite $Ca_{1-x}Sr_xIrO_3$ (x = 0, 0.5, and 1) thin films: the role of strong spin-orbit coupling, S. Y. Jang, H. S. Kim, S. J. Moon, W. S. Choi, **B. C. Jeon**, J. Yu, and T. W. Noh, Journal of Physics: Condensed Matter **22**, 485602 (2010).
12. Effects of oxygen-reducing atmosphere annealing on $LaMnO_3$ epitaxial thin films, W. S. Choi, Z. Marton, S. Y. Jang, S. J. Moon, **B. C. Jeon**, J. H. Shin, S. S. A. Seo, T. W. Noh, K Myung-Whun, H. N. Lee, and Y. S. Lee, Journal of Physics D: Applied Physics **42**, 165401 (2009).
13. Influence of the Magnetic Correlation to the Electronic Structure of Hexagonal $TbMnO_3$ Thin Films Investigated by Using Optical Spectroscopy, W. S. Choi, S. J. Moon, **B. C. Jeon**, J. H. Lee, and Y. S. Lee, Journal of the Korean Physical Society **55**, 754 (2009).

국문 초록

물질을 휘었을 때 물질 내부에 불균일한 변형(inhomogeneous strain)이 생기게 되고, 이러한 변형 기울기(strain gradient)에 의해 물질 내에 전기장을 발생시킬 수 있는데, 이러한 현상을 변전효과(flexoelectric effect)라고 한다. 비록 변전효과는 1960년대에 Kogan에의해 처음 제시되었고 오랜 연구 역사를 가지고 있지만 덩치 (bulk) 시료에서는 많은 연구가 되어있지 않다. 왜냐하면 변전효과는 덩치시료에서 매우 작기 때문이다. 실제로 덩치시료를 휘었을 때 생기는 변형 기울기는 1/10 m^{-1} 정도의 값을 갖는다. 최근에, 변전 효과는 특히 박막에서 새롭게 많은 흥미를 끌고 있다. 왜냐하면 켜쌓기(epitaxial) 성장시킨 박막을 이용하면 변전효과가 매우 커질 수 있을 뿐만 아니라 그 크기 또한 제어 할 수 있기 때문이다. 박막이 두꺼워 질수록 기판의 클램핑 효과(clamping effect)가 약해져 변형완화(strain relaxation) 현상이 생긴다. 변형완화가 일어나는 영역은 수십 나노 두께에서 일어나기 때문에 변형완화에 의해 유도되는 변형 기울기 값은 10^5~10^6 m^{-1} 이다. 이 크기는 덩치시료와 비교했을 때 약 100만 혹은 1000만 배 큰 값이다. 본 논문에서는 강유전체(ferroelectrics) 박막에서 변전효과가 물리적으로 어떤 영향을 미치는지에 대해 보여주고자 한다. 즉, 변전효과가 내부적으로 전기장을 만들게 되고, 만들어진 전기장에 의해 강유전체 박막 내에 자발분극(self-polarization)의 방향을 뒤집음으로써 다양한 전기기능적 특성을 제어할 수 있음을 보여주고자 한다.

강유전성, 강탄성(ferroelasticity), 그리고 반강자성(antiferromagnetism)을

동시에 가지고 있는 다강체 (multiferroic) $BiFeO_3$(BFO)는 흥미로운 물리적 성질 때문에 지금까지 많은 관심을 받고 있고 많은 연구가 되고 있다. 하지만 다양하고 많은 연구에도 불구하고 아직도 해결 되지 못한 문제들이 많이 있기 때문에 연구해야 할 부분은 많이 남아있다. 본 논문에서는 증착온도가 BFO 박막에서의 결점 (defect) 형성과 강유전성에 어떻게 영향을 주는지 보여주고자 한다. 증착온도와 박막의 두께에 따라 변형 전개를 성공적으로 제어하였다. 그리고 변전효과가 BFO 박막의 자발분극 방향을 아래 방향에서 위 방향으로 뒤집을 수 있음을 보여주고자 한다. 이러한 자발 분극은 BFO 박막의 전기 기능성 측면에 영향을 줄 수 있음을 보여주고자 한다. 마지막으로, 변전 효과를 통해 내부 전기장을 제어함으로써 결점 형성을 제어하거나 완벽한 기능성을 수행하고 결점이 없는 박막을 제작할 수 있음을 보여주고자 한다.

강유전체 물질은 전기 기능적 특성과 관련된 넓은 영역에서 전도 유망하고, 이들의 특성은 다양한 결점에 영향을 받는다. 강유전체의 실용적 응용측면에서 결점을 제어하고 이해하는 것은 무엇보다 중요하다. BFO 박막의 결점 전개와 변전효과를 연구하기 위해서, BFO 박막을 펄스 레이저 증착법을 이용해 산화물 기판 위에 10도 간격으로 550도에서 600도 까지 성장시켰다. 결점이 590도 이상에서 나타나기 시작하는 것을 발견하였다. 그리고 결점이 형성된 박막은 분광과 엑스레이 회절 실험에서 더욱 뚜렷한 차이를 보인다. 또한 결점은 원자 감응 현미경으로 박막의 표면을 관측했을 때 표면 거침 (roughness)에 갑작스런 영향을 준다. 게다가 결점은 강유전성에 영향을 준다는 것을 관측하였다. 본 논문에서는, 이러한 결과로부터 결점의 전개는

증착온도가 가장 중요한 요인이라는 것을 보여주고자 한다.

강유전체는 증착 과정 중에 계면효과(interface effect), 변전효과, 압전효과(piezoelectricity)에 의해 내부 전기장이 형성될 수 있다. BFO 박막을 $SrRuO_3$ 하부 전극 위에 성장 시켰을 때 계면효과에 의해 아래 방향으로 전기장이 유도 된다. 유도된 전기장과 같은 방향으로 자발분극이 정렬된다. 하지만 변전효과에 의해 내부 전기장을 위쪽 방향으로 유도하게 되면 BFO 박막 내에 자발분극이 위쪽 방향으로 정렬된다. 결점쌍극자(defect dipole)는 자발 분극과 같은 방향으로 형성되는데, 결점쌍극자의 방향에 따라 강유전체 자국(imprint)의 방향이 다르다. 즉, 결점쌍극자가 위 방향으로 정렬하게 되면 분극-전기장 이력곡선이 네가티브 자국이 되고, 결점쌍극자가 아래 방향으로 정렬되면 분극-전기장 이력곡선이 포지티브 자국이 된다. 또한 산소 결핍은 전하보상 때문에 분극의 꼬리 쪽에 모여 산소 결핍층(oxygen vacancy layer)을 형성하게 된다. 산소 결핍층은 전하주입을 방해를 하게 되고 전기적 특성에 영향을 준다. 즉, 산소 결핍층이 Pt/BFO 계면에 있을 때는 분극 방향에 따라 역방향 다이오드 특성을 보이고, 산소 결핍층이 BFO/SRO 계면에 있을 때는 분극 방향에 따라 순방향 다이오드 특성을 보인다. 마지막으로, 변전효과의 크기를 조절해서 계면효과와 거의 같은 크기로 만들면 BFO 박막 내부 전기장을 거의 0으로 만들 수 있다. 이러한 특성을 잘 이용하면 결점이 거의 없는 BFO 박막을 제작할 수 있고, 완벽한 전기 기능성을 보이는 박막을 제작할 수 있다. 즉, 자국이 없고 분극 방향에 따라 양방향 다이오드 특성을 보이는 박막을 구현할 수 있음을 보여주고자 한다.

주요어: $BiFeO_3$, 강유전체, 변형, 변형 기울기, 변전 효과, 껴쌓기 박막, 결점, 자발 분극, 내부 전기장.

학번 2006-22908

감사의 글

어느덧 제가 박사학위를 마치고 마지막 감사의 글을 쓰게 되었습니다. 2008년 2월 처음 실험실 그룹 미팅에서 저의 실험실 생활이 시작 되었습니다. 그 때 모든 분들께서 반갑게 환영을 해주셨던 것이 생각납니다. 실험실에 합류하고 그 때의 고마운 분들께서 계셨기 때문에 제가 무사히 박사학위를 마칠 수 있었습니다. 이제 그 분들과 다른 고마운 분들께 감사의 글을 시작하고자 합니다.

제일 먼저 아내에게 진심 어린 감사의 마음을 전합니다. 박사과정을 시작하는 해에 저와 결혼해 두 아이를 키우고, 제가 연구에만 매진 할 수 있게 묵묵히 도와주었습니다. 당신과 결혼한 것은 제 인생의 최고의 행운이자 선택이었다고 생각합니다. 감사합니다. 그리고, 사랑하는 상훈이와 소율, 아빠의 아들 딸로 태어나주어서 감사합니다. 아침마다 아빠가 출근할 때 잘 하지도 못하는 말로 “다녀오세요” 라고 인사해주고 집에 오면 언제나 반갑게 맞아주어서 아빠의 힘이 되었습니다. 지금처럼 항상 건강하고 씩씩한 아들 딸이 되어주길 바랍니다.

어머님, 이예숙 여사님께 감사의 마음을 전합니다. 부족한 아들이 무사히 학위를 마칠 수 있었던 것은 어머님의 도움이 가장 컸습니다. 아들이 연구에만 매진 할 수 있도록 아버님 병간호를 해주셨고, 아들의 행복한 가정을 꾸려주셔서 제가 이만큼 성장 할 수 있었습니다. 앞으로 당신의 아들이 성공하고 건승하는 모습을 보여드리고, 항상 감사하는 마음으로 어머님께 보답하겠습니다. 다시 한번 머리 숙여 진심으로 감사 드립니다.

언제나 걱정 많이 해주시고 잘되길 기원해주신 장인어르신과 장모님께 감사의 마음 전합니다. 앞으로 즐겁고 건강한 가정이 되도록 노력하겠습니다. 누나 예라, 예심, 예선에게도 감사합니다. 하나 밖에 없는 매형, 유서방, 그리고 윤서방에게도 감사의 마음을 전합니다. 모두들 행복한 가정을 이루고 예쁘고 멋진 조카들과 즐겁고 건강한 가정이 되길 바랍니다. 조카들 태준, 지민, 하린, 그리고 아직 막둥이 배속에 있는 조카, 모두들 씩씩하고 건강하길 바라겠습니다.

서울대학교에 석사과정으로 1년을 보내고 실험실 선택을 위해 처음 노태원

교수님을 뵙게 되었을 때를 떠올려 봅니다. 돌이켜 보면 그 때 교수님께서 저를 선택해주시고 지도 해주신 점 정말 감사 드립니다. 교수님으로부터 정말 많은 것을 배웠습니다. 좋은 연구자가 되는 방법과 사회지도자들의 마인드와 처세를 제가 직접 옆에서 보고 배운 것은 저에게 가장 큰 행운이자 축복 입니다. 시골에서 자라 이러한 것들을 보고 배울 기회가 없었는데, 교수님께서는 저에게 가르침을 받을 수 있는 기회를 주셨습니다. 제가 사회에 나갔을 때 교수님으로부터 배운 것들이 제 인생에 큰 자산이 되고, 특히 회사에 가서 성공적인 지도자가 될 수 있을 것이라 생각합니다. 진심으로 감사 드립니다.

전북대학교 부상돈 교수님께 진심으로 감사의 말씀을 전합니다. 어떻게 보면 저의 첫 논문을 지도해주시고 많은 조언을 주셨기에 제가 무사히 박사학위를 마칠 수 있었습니다. 항상 좋은 자리로 이끌어 주시려고 많은 조언을 주셨기에 제가 앞으로 더 나은 인생을 설계할 수 있을 것이라 생각합니다. 앞으로 하시는 일 모두 잘 되시고 댁내 평안하시길 기원합니다.

수원대 윤종걸 교수님께도 진심으로 감사의 말씀 전합니다. 바쁘신 와중에도 매주 저희 미팅에 참석하셔서, 항상 제 연구 결과에 진심 이린 충고와 조언을 해주셨습니다. 또한 제가 미쳐 생각하지 못한 부분을 집어주시고, 올바른 연구 방향으로 갈 수 있게 이끌어 주셨습니다. 윤종걸 교수님의 도움이 없었다면 제가 무사히 학위를 받지 못했을 것입니다. 다시 한번 진심으로 감사 드립니다.

또한 숭실대 정진석 교수님, 이윤상 교수님께 감사의 말씀을 전합니다. 정진석 교수님께서 제 박막의 구조분석에 정말 많은 도움을 주셨습니다. 심지어 포항에까지 직접 오셔서 실험을 도와주신 점은 정말 감사 드립니다. 이윤상 교수님께서는 저의 첫 논문에 정말 많은 도움을 주셔서 대단히 감사 드립니다. 창원대 송태권 교수님께도 감사의 말씀을 전합니다. 제가 $BiFeO_3$ 박막을 성공적으로 만들 수 있었던 것은 송태권 교수님께서 고품질의 target을 제공해주셨기 때문에 가능했습니다.

제 박사학위 심사위원이신 유재준 교수님, 박제근 교수님, 그리고 채석봉 교수님께 감사의 말씀을 전합니다. 마지막 defense가 끝나고 유재준 교수님께서 “박사를 받고 나가면 이제부터는 야생이니 열심히 하길 바란다.” 라고 해주신 말씀 명심하겠습니다. 그리고 진심 어린 조언 감사 드립니다. 교수님들의 가르침 잊지 않고 늘 명심하겠습니다.

학위를 받는 동안 제 연구에 많은 도움을 주신 분들께 감사의 말씀은 전합니다. 창원대 이명환, 자네의 고품질 $BiFeO_3$ target이 없었다면 제가 좋은 연구를 할 수

없었을 것입니다. 남은 학위 잘 마무리하고 좋은 일 많이 하길 기원하겠습니다. 김충현 박사님의 이론계산은 제 연구에 많은 도움이 되었습니다. 현재 Wisconsin에 계신 이대수 박사님께 정말 감사 드립니다. 저에게 좋은 아이디어를 주셔서 제가 정말 훌륭한 논문을 쓸 수 있었습니다. 성공적인 포닥 생활이 되시고 형수님과 도헌이 모두 건강하길 기원합니다. 제 첫 사수 한양대 문순재 교수님께 감사 드립니다. 실험실에 처음 들어와 큰 실수를 했는데도 잘 다독여 주시고 끝까지 그 일을 마무리 할 수 있게 도와 주셨습니다. 사모님과 잘 생긴 아들 모두 건강하길 기원합니다. 서울 시립대 장영준 교수님, 광주과학 기술원 조지영 교수님께 감사의 말씀을 전합니다. 성균관대 최우석 교수님께도 감사의 말씀을 전합니다. 박사 후 연구원 생활을 성공적으로 마치고 한국에 돌아 오신지 얼마 되지 않으셨지만 연구를 잘 하시니 앞으로 훌륭한 학자가 되실 것이라 생각합니다. 권지환 박사님께도 감사의 마음을 전합니다. 저희 실험실에서 얼마 계시지 않았지만 제 연구에 많은 도움을 주셨습니다. 저희 연구단 팀 리더로 오신 김형도 박사님, 조덕용 박사님, 이승란 박사님, 그리고 김민우 박사님께도 감사의 마음을 전합니다. 앞으로 각 팀의 리더로써 팀을 잘 이끌어서 좋은 연구 많이 하시길 기원합니다.

연구단에 합류하여 같이 지냈던 선후배님들에게도 감사의 마음을 전합니다. 그 당시 정말 스마트한 선배들과 같이 일을 할 수 있었던 것은 제인 인생의 최고의 행운입니다. 처음 “ReCOE” 연구실에 합류해 IR 팀에서 같이 보낸 종훈이 아람이에게도 감사 드립니다. 현재 Wisconsin에서 박사 후 연구원을 하고 계신 김태헌 박사님, 삼성 종합기술원에 계신 김용수 박사님, 엘지전자에 계신 장승엽 박사님, Argonne National Lab.에 계신 장서형 박사님께 감사의 말씀을 전합니다. SK 하이닉스에 있는 문지에게도 감사의 마음을 전합니다. 녹두에 살 때 같이 술도 많이 마시고, 늦게까지 실험실에서 연구하던 이신범 박사님, 양상모 박사님께 감사의 말씀을 전합니다. 이신범 박사님의 우직하고 끝까지 해내는 모습은 제가 꼭 본받고 싶은 부분입니다. 나이도 저와 같은 스마트 양상모 박사님, 친구지만 연구하는데 있어서는 제가 배워야 할 부분이 많았습니다. 두분 다 Oak Ridge에 좋은 연구 많이 하시고, 행복한 가정 이루시길 바랍니다. 이번에 같이 학위를 받는 스마트 정다운 박사, 회사에 가서도 성공적인 구성원이 되길 기원 합니다. 아직 한 학기 남은 향근이도 남은 박사학위 기간 동안 잘 마무리하고 원하는 곳에 가서 성공적인 박사 후 연구원 생활이 되길 기원 하겠습니다. 우리 실험실 분위기 메이커인 창희, 우직하게 연구를 하는 영재, 수빈이, 현주에게 감사의 마음을 전합니다. 이제 박사학위 시작하는 지섭에게도 감사의 마음을 전합니다. 제 처음이자 마지막 부사수 성민에게도 감사의 마음을 전합니다. 이제 박사학위를 시작하지만 앞으로 잘 해나가리라 생각합니다. 실험실에 학부 인턴으로 온 재현, 태영, 훈호, 이곤, 태윤에게도 감사의 마음을 전합니다. XRD operator 금채씨에게도 감사의 마음을

전합니다. 지금은 실험실에 안 계시지만 월미씨에게도 감사의 마음을 전합니다.

마지막으로, 제가 가장 존경하는 아버님(田羅秀)께 박사학위 영광을 돌립니다. 지금은 세상에 안 계시지만 아버님은 제게 어려서부터 인생의 선배로써 많은 조언을 주셨습니다. 명절 마다 같이 성묘가면서 해주신 말씀들이 생각납니다. 당신은 제 기억 속에 언제나 최고의 남자였고 아버지 입니다. 그래서 제가 가장 존경하는 사람 입니다. 아버지만큼 멋진 아들이 되도록 최선을 다하겠습니다. 아버지 사랑합니다. 그리고 제 온 진심을 담아 감사 드립니다.

2014년 1월 관악에서
전병철 드림